Investigations of Thermoelectric Properties of 2D-Layered Tin Selenide

A thesis submitted in Partial Fulfillment of the Degree of

MASTER OF SCIENCE

as a part of

Integrated Ph.D. Programme (Chemical Science)

By

Sushmita Chandra

New Chemistry Unit

Jawaharlal Nehru Centre for Advanced Scientific Research

(*A deemed University*)

Bangalore, India

(March 2019)

Dedicated to my beloved family
and Prof. Biswas's group

Declaration

I hereby declare that this thesis entitled **"*Investigations of Thermoelectric Properties of 2D-Layered Tin Selenide*"** is an authentic record of research work that has been carried out by me at Solid State Chemistry Laboratory, New Chemistry Unit, Jawaharlal Nehru Centre for Advanced Scientific Research, Bangalore, India under supervision of Prof. Kanishka Biswas. This work has not been submitted elsewhere for the award of any degree or diploma. Whenever contributions of others are required, every effort is made to indicate it clearly, with due reference to the literature, and acknowledgement of collaborative research and discussions.

Date:
Bangalore, India   Sushmita Chandra

Prof. Kanishka Biswas
Associate Professor
New Chemistry Unit
Jawaharlal Nehru Centre for
Advanced Scientific Research
Bangalore, India -560064

Email: kanishka@jncasr.ac.in
Phone: +91-80-22082678 (office)
+91-9902063469 (mobile)
FAX : +91-80-2208-2627
Web: http://www.jncasr.ac.in/kanishka/

Certificate

Certified that the work described in this thesis titled **"*Investigations of Thermoelectric Properties of 2D-Layered Tin Selenide*"** has been carried out by Ms. Sushmita Chandra at Solid State Chemistry Laboratory, New Chemistry Unit, Jawaharlal Nehru Centre for Advanced Scientific Research, Bangalore, India under my supervision and that it has not been submitted elsewhere for the award of any degree or diploma.

Date:
Bangalore, India

Prof. Kanishka Biswas
(Research Supervisor)

Acknowledgements

Completion of my M.S. thesis necessitated a lot of guidance and support from many people. I take this opportunity to mention a few of them. However, my sincere thanks extend to everyone who has played a role in making this dream a reality.

Firstly, I would like to thank my research supervisor, Prof. Kanishka Biswas for suggesting me a research problem and guiding me throughout. He has been a constant source of inspiration for me to build up new ideas and carry out experiments. I greatly admire his enthusiasm towards science. His enthusiasm makes a mark upon the young heart, urging them to perform as best as one could. I express my hearty gratitude to him for giving me an opportunity to work under his guidance. I also wish to thank him for correcting me with patience and for forgiving my flaws.

I would like to thank Prof. C. N. R. Rao, FRS, the chairman of New Chemistry Unit (NCU) for his generous support and encouragement throughout my stay in JNCASR. The zeal with which he practices science and his way of looking into a problem with a scientific eye has been a source of inspiration for me. His presence has given me immense inspiration to indulge in active research. I also thank him for providing the infrastructure and facilities to carry out my research work.

I would like to thank our collaborator, Prof. U. Waghmare and his student Ms. Raagya Arora. I have learnt a lot whenever I had meeting with them or discussion with them. I am grateful to Dr. Mrinmoy De and his student Subrata for helping me in AFM measurements.

I thank my past and present lab mates Dr. Provas, Dr. Satya Narayan, Dr. Manoj, Dr. Suresh, Dr. Tanmoy, Dr. Shidaling, Arka, Ananya, Subhajit Roychowdhury, Manisha, Ekashmi, Moinak, Paribesh, Debottam, Krishnendu, Riddhimoy and Subhajit for their cheerful company and help in various occasions. I got the opportunity to learn a lot about research and many instruments from them. Their discussion on past experience, valuable inputs about research life and experiments helped me immensely.

I would like to thank JNCASR for providing me all the facilities.

Preface

Thermoelectric effect enables direct conversion of thermal to electrical energy and provides an alternative route for power generation applications. Although PbTe and Bi_2Te_3 are the most efficient materials for thermoelectrics, environmental concern about lead (Pb) and tellurium (Te) prevents its use for large scale applications. Hence, the goal of thermoelectric community is to design Pb and Te free thermoelectric materials with high efficiency. The thesis entitled "*Investigations of Thermoelectric Properties of 2D-Layered Tin Selenide*" demonstrates the synthesis, structure and optimization of thermoelectric properties of environment friendly SnSe. The thesis has been divided into four chapters.

Chapter 1 of the thesis begins with a brief introduction of the two dimensional layered metal chalcogenides for thermoelectrics and the useful approaches to enhance the thermoelectric figure of merit (zT). Herein, I have discussed about various state-of-the-art 2D layered metal chalcogenides and their thermoelectric properties along with the present understandings and latest developments. Finally, I have discussed about the motivation of the thesis.

Chapter 2 discusses the high thermoelectric figure of merit, zT of 2.1 in two dimensional (2D) nanoplates of Ge doped SnSe synthesized by a simple hydrothermal route followed by spark plasma sintering (SPS). Ge-doping in SnSe nanoplates significantly enhances the p-type carrier concentration which results in high electrical conductivity and power factor of ~5.10 $\mu W/cmK^2$ at 873 K. In addition to nanoscale grain boundary and high lattice anharmonicity in SnSe nanoplates, phonon scattering due to Ge precipitates in the SnSe matrix gives rise to the ultralow lattice thermal conductivity of ~0.18 W/mK at 873 K.

Chapter 3 deals with the solution phase synthesis and thermoelectric transport properties of ultrathin (1.2-3 nm thick) few layered n-type Bi doped SnSe nanosheets. Bi-doping enhances the carrier concentration of n-type SnSe significantly from 3.08×10^{17} cm^{-3} to 1.97×10^{18} cm^{-3} which results in the increment of electrical conductivity and power factor. Furthermore, Bi-doped nanosheets exhibit ultralow lattice thermal conductivity (~ 0.3 W/mK) throughout the temperature range of 300-720 K which can be ascribed to the

effective phonon scattering by interface of SnSe layers, nanoscale grain boundaries and point defects.

Chapter 4 discusses about the experimental stabilization of high-pressure cubic phase of SnSe at ambient conditions with 30 mol% AgBiSe$_2$ alloying. This can be attributed to the interplay of chemical pressure and the introduction of high entropy with the alloying of AgBiSe$_2$ Interestingly, the band-gap of orthorhombic SnSe decreases with AgBiSe$_2$ substitution and for cubic SnSe band gap approaches nearly to 0 eV.

Contents

Chapter 1

2D-Layered Chalcogenides for Thermoelectric Energy Conversion

<div align="right">

Chapter 1

</div>

2D-Layered Chalcogenides for Thermoelectric Energy Conversion

1.1 Introduction

In this era of 21st century, energy crisis and consequent enormous demand of conventional energy sources compel the incorporation of renewable energy sources to combat the energy issues worldwide. Considering the overall global energy consumption, almost two-third of energy is lost as waste heat (Figure 1.1).[1, 2] One of the promising solution to utilize this waste heat as electrical energy is Thermoelectrics. Thermoelectric (TE) materials, using the principle of Seebeck Effect, play a pivotal role in the direct and reversible conversion of heat into electricity (Figure 1.1).[2, 3] Among all the TE materials ever discovered till now, 2D-layered metal chalcogenides have shown considerable impact due to their intrinsically low thermal conductivity and high Seebeck coefficient arising from their strong anisotropic nature. Several notable materials like Bi_2Te_3, Bi_2Se_3, BiSe, SnSe, BiCuSeO and GeSe based systems are hitherto explored, among which SnSe has drawn particular attention due to their ultralow thermal conductivity and remarkably high zT value. In this chapter, I have discussed about the synthesis, structure and thermoelectric properties of a few important layered chalcogenides.
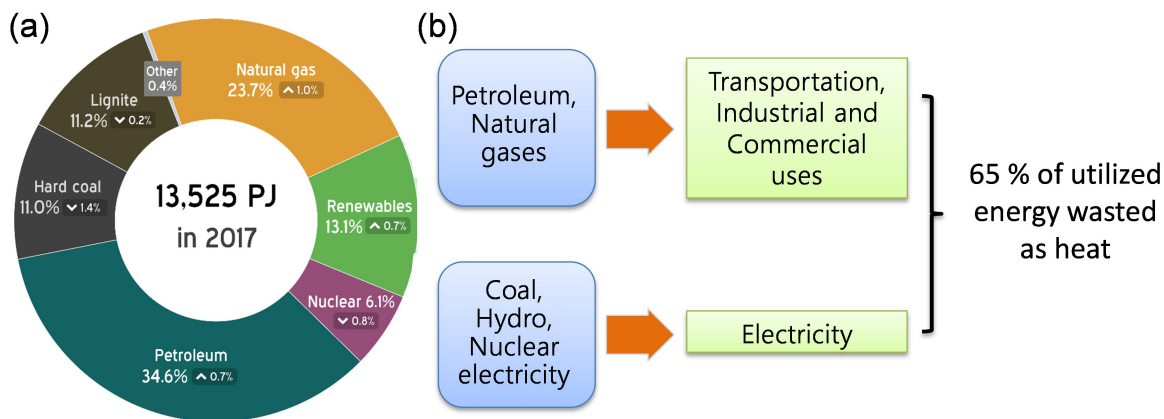
Figure 1.1 (a) Total energy consumption by type for India in year 2017 in petajoules and percents (Source-Ref 1). (b) Schematic demonstrates how ~65 % of the utilized energy being lost as waste heat.

1.2 Origin of Thermoelectric Effect

Thermoelectric effect is the direct and reversible conversion of waste-heat to electricity and vice versa.[4] It is based on two important transport effects: Seebeck effect and Peltier effect.

When a temperature gradient (ΔT) is applied to a thermoelectric (TE) couple consisting of *n*-type and *p*-type elements, the mobile charge carriers (electrons in *n*-type and holes in *p*-type) at the hot end diffuse to the cold end, producing a potential difference (ΔV). This effect is known as Seebeck effect,[5, 6] where S (equation 1.1) is defined as the Seebeck coefficient, forms the basis of TE power generation (Figure 1.2 (a)).

$$S = \frac{\Delta V}{\Delta T} \qquad (1.1)$$

Conversely, when a potential difference is applied to a TE couple, carriers bring heat from one side to the other so that one side gets cooler while the other gets hotter, an effect known as the Peltier effect (Figure 1.2 (a)) which forms the basis of TE refrigeration.[7]

The thermoelectric conversion efficiency for a material requires both high zT values and a large temperature difference across the thermoelectric materials, as given by the

following relation (equation 1.2):[4]

$$\eta_{TE} = \eta_c \frac{(\sqrt{1+zT}-1)}{\left(\sqrt{1+zT}+\frac{T_C}{T_H}\right)}$$ (1.2)

where η_c, T_H and T_C are Carnot Efficiency, the temperatures of the hot and cold ends and zT, the dimensionless figure of merit is expressed as:

$$zT = \frac{\sigma S^2}{\kappa_{ele}+\kappa_{lat}} T$$ (1.3)

where σ, S, κ_{ele}, κ_{lat} and T are the electrical conductivity, Seebeck coefficient, electrical thermal conductivity, lattice thermal conductivity and absolute temperature, respectively.[8-15]

1.3 Conflicting Thermoelectric Parameters

Fundamental to the field of thermoelectric materials is the need to optimize a variety of conflicting properties. An ideal thermoelectric material should have high electrical conductivity similar to metals, large Seebeck coefficient as in semiconductors and ultra-low thermal conductivity like glasses.

1.3.1 Seebeck Coefficient and Electrical Conductivity

For large Seebeck coefficient, there should be only single type of carrier.[3] Mixed *n*-type and *p*-type conduction will lead to both charge carriers moving to the cold end, cancelling out the induced Seebeck voltages. Insulators and semiconductors (in both cases carrier concentration is low) have very high Seebeck coefficients (equation 1.4), but very low electrical conductivity (equation 1.5). The interrelationship between carrier concentration and Seebeck coefficient can be seen from the models of electron transport. For metals or degenerate semiconductors (single parabolic band and energy-independent scattering approximation)[3] the Seebeck coefficient is given by:

$$S = \frac{8\pi^2 k_B^2}{3eh^2} m^* T \left(\frac{\pi}{3n}\right)^{2/3} \tag{1.4}$$

where n is carrier concentration and m^* is effective mass.

Electrical conductivity (σ) is related to n through the following expression:

$$\sigma = ne\mu \tag{1.5}$$

where μ is carrier mobility.
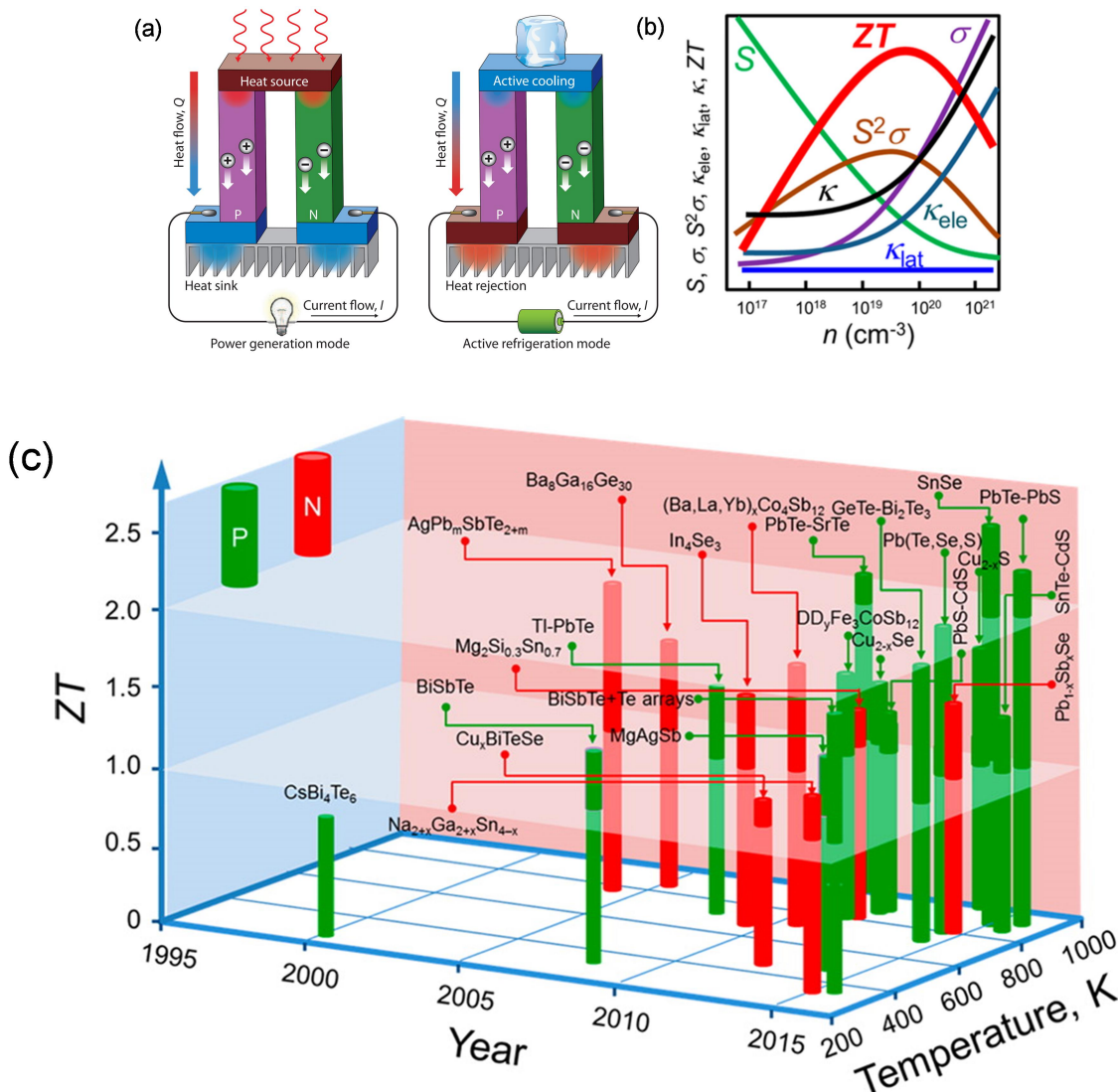
Figure 1.2 (a) Schematic illustrations of a thermoelectric (TE) module for active refrigeration-Peltier effect (left) and power generation-Seebeck effect (right). (b) Schematic diagram showing the variation of zT and related TE parameters, electrical conductivity (σ), Seebeck coefficient (S), power factor ($S^2\sigma$), electronic thermal conductivity (κ_{ele}), lattice thermal conductivity (κ_{lat}), and total thermal conductivity (κ), as a function of carrier concentration (n). The TE parameters are highly correlated thereby limiting the maximum zT. (c) TE figure of merit (zT) as a function of temperature and year illustrating important milestones. (b) and (c) are reproduced with permission from ref. 16 © 2016 American Chemical Society.

An ideal thermoelectric material should have high electrical conductivity similar to metals, large Seebeck coefficient as in semiconductors and ultra-low thermal conductivity like glasses. It is always challenging for the chemists to design a single TE material that meets all the above criteria; moreover, the high interdependence of all the above properties poses an inherent limit to the maximum zT that can be attained in a given material (Figure 1.2 (b)). Figure 1.2 (c) shows the evolution of zT over the past two decades and it clearly shows that the-state-of-art TE materials are found among heavy metal chalcogenides, especially those based on Bi and Pb such as Bi_2Te_3, PbTe, and PbSe.[16]

Figure 1.2 (b) shows compromise between large thermopower and high electrical conductivity in thermoelectric materials to maximize the figure of merit, zT. The peak value of zT arises in the carrier concentration range of 10^{19}-10^{21} cm^{-3} (Figure 1.2 (b)) which falls in between metals and semiconductors that is concentration found in heavily doped semiconductors (degenerate semiconductor).[3]

1.3.2 Effective Mass

The effective mass of the charge carrier offers another conflict as large effective masses generate high thermopower but low electrical mobility. The m^* in equation 1.4 refers to the density-of-states effective mass, which increases with flat and narrow bands with high density of states at the Fermi surface. However, as the inertial effective mass is also related to m^*, heavy carriers will move with slower velocities, and therefore small mobility, which in turn leads to low electrical conductivity (equation 1.5). The precise relationship between effective mass and mobility is complex, and depends on electronic structure, scattering mechanism and anisotropy. In principle, these effective mass terms can be decoupled in anisotropic crystal structures.[3, 5]

A equilibrium must be found for the effective mass (or bandwidth) for the dominant charge carrier, forming a compromise between high effective mass and high mobility. Optimum effective mass for thermoelectric is not known; good thermoelectric materials can be found within a wide range of effective masses and mobility: from low-mobility, high-effective-mass polaron conductors (oxides,[3] chalcogenides[3]) to high-mobility, low-effective-mass semiconductors (SiGe, GaAs).

1.3.3 Electrical Thermal Conductivity

Additional confliction in material design comes from the necessity for low thermal conductivity.[3] Thermal conductivity in thermoelectrics appears from two sources:

(1) electrons and holes transporting heat (κ_{el}) and,

(2) phonons travelling through the lattice (κ_{lat}).

Here κ_{el} is directly related to the electrical conductivity through the Wiedemann–Franz law:

$$\kappa_{el} = L\sigma T \tag{1.6}$$

where L is the Lorenz factor, $2.4 \times 10^{-8}\,\mathrm{W\Omega K^{-2}}$ for free electrons.

The Lorenz factor can vary with carrier concentration. Accurate evaluation of κ_{el} is important, as κ_{lat} is often computed as the difference between κ_{total} and κ_{el} using the experimental electrical conductivity. Ambiguity in κ_{el} happens due to mixed conduction, which introduces bipolar term into the thermal conductivity. As this term is not considered into the Wiedemann–Franz law, the standard computation of κ_{lat} erroneously takes account of bipolar thermal conduction. This results in a perceived increase in κ_{lat} at high temperatures for low band gap materials like Bi_2Te_3 and $PbTe$.[5]

1.3.4 Lattice Thermal Conductivity

Glasses exhibit very low lattice thermal conductivity. In a glass, thermal conductivity

is considered as a random walk of energy throughout a lattice rather than rapid transport via phonons, and leads to the concept of a minimum thermal conductivity, κ_{min}.[3] Actual glasses, however, make poor thermoelectrics because of the absence of needed 'electron-crystal' properties, required for superior electrical transport property (σ) compared with crystalline semiconductors, they have lower mobility due to increased electron scattering and lower effective masses because of broader bands. Good thermoelectric materials are therefore crystalline materials that manage to scatter phonons without significantly interrupting the electrical conductivity.[3] The heat flow is carried by a spectrum of phonons with widely varying wavelengths and mean free paths (from less than 1 nm to greater than 10 μm), creating a need for phonon scattering agents at a variety of length scales.[3]

1.4 Layered Chalcogenides in High Performance Thermoelectrics

1.4.1 Importance of 2D-Layered Structure

Synthesis of novel solid state inorganic materials with diverse structural and chemical properties, is the pathway to achieve rapid development in material based technologies.[17-23] Application of proper material designing strategies is the key step to play with the intricate properties of a material, where the aspect of dimensionality comes as a significant part. Variation of dimensionality infuses different fascinating characteristics in a material, which reveals invaluable insights regarding the electronic structure and thermal properties. From 0D quantum dots to 3D crystal solids, numerous materials have been investigated, where 2D materials have gained momentous attention due to their layered structure and quantum confinement.[19-23] Such 2D layered materials are mainly stabilized by the in-plane covalent bonding interaction and interlayer van der Waals interaction. 2D materials have prospective

applications in electronics, catalysis, gas separation and sensor applications.[23-25] In the following section, I will provide a brief discussion on the importance and uniqueness of layered material for the thermoelectric energy conversion.

The investigations on the thermoelectric properties of the layered materials have been mainly focused on two different class of solids: (a) bulk layered materials and (b) ultrathin 2D nanostructures. The anisotropic nature of crystal structure and chemical bonding result in significant variation of the thermoelectric properties in different crystallographic directions for layered solids. Synthesis of single/few-layer nanosheets material by exfoliation of layered bulk materials or by bottom up wet chemical method and investigation of their thermoelectric properties is also important for fundamental materials science and technology design.

Primarily, the work of Hicks and Dresselhaus in 1993 inspired the researchers to study the thermoelectric properties in nanomaterials, which shows reduction of dimensionality from 3D to 2D structure (quantum wells) to 1D structure (quantum wires) and finally to 0D structure (quantum dots), can create new opportunities to vary S, σ, and κ quasi-independently. The dimensionality reduction offers the accessibility of new variable of length scale to control the materials properties.[26-30] When size of the material reduced to nano dimension, comparable to the spatial extent of the electronic wave function confining the electrons in one or more dimension, the quantum confinement arises. According to Mott-Jones relation, this can results in increase of the slope of the density of states (DOS) at the Fermi level.[4, 28-30]

$$S = \frac{\pi^2}{3}\frac{k^2 T}{e}\left(\frac{\partial log\sigma(E)}{\partial E}\right)_{E=E_F} \tag{1.7}$$

where, S is seebeck coefficient, $\sigma(E)$ is the electronic conductivity determined as a function of the band filling or Fermi energy E_F, k is Boltzmann constant, e is electronic charge.

Low-dimensional quantum-confined systems generally show sharp and dispersionless bands, hence by tuning the size of solids it is possible to place these states near the Fermi level, which could enable a marked increase in Seebeck coefficient (Figure 1.3).
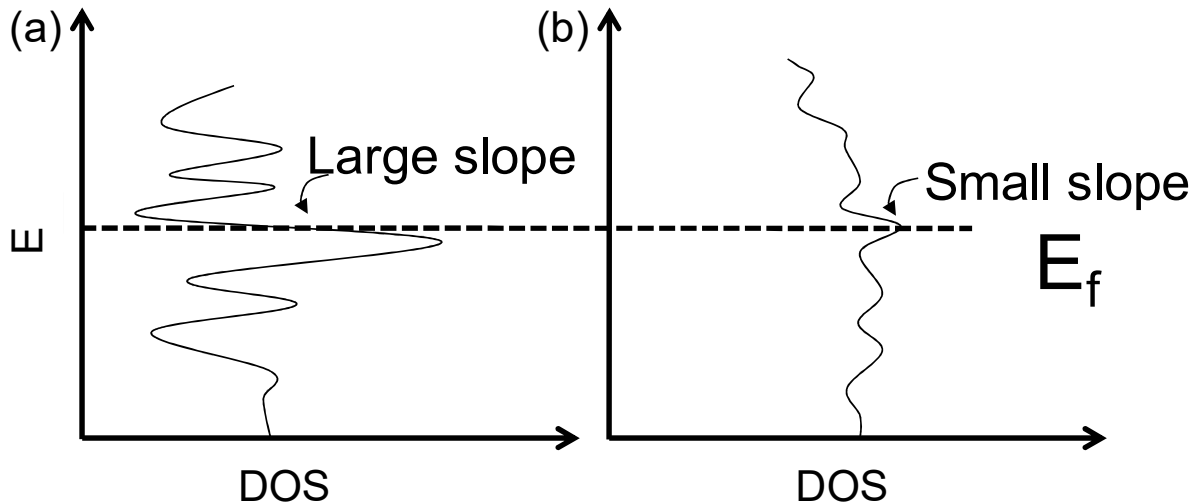
Figure 1.3 Hypothetical density of state (DOS) with (a) a large slope (dlnσ(E)/dE) and (b) a small slope near E_F.

Presence of numerous interfaces and surfaces in nanostructured material should enhance phonon scattering, thereby can reduce thermal conductivity (Figure 1.4). The advantages of using nanostructured materials for thermoelectrics can be summarized in following points:

(a) enhancement in the density of states near E_F, which leads to enhancement of the Seebeck coefficient, (b) benefit of the anisotropic Fermi surfaces in the case of multi-electronic band valley material (c) increase the boundary scattering of phonons at the interfaces, without much carrier scattering at the interface, and (d) increased carrier mobility at a given carrier concentration when quantum confinement conditions are satisfied, so that modulation doping can be utilized.[28-30] In general all these advantages collectively or distinctly favor to optimize the S, σ, and κ independently in a single material in nano dimension.[2, 30-31]
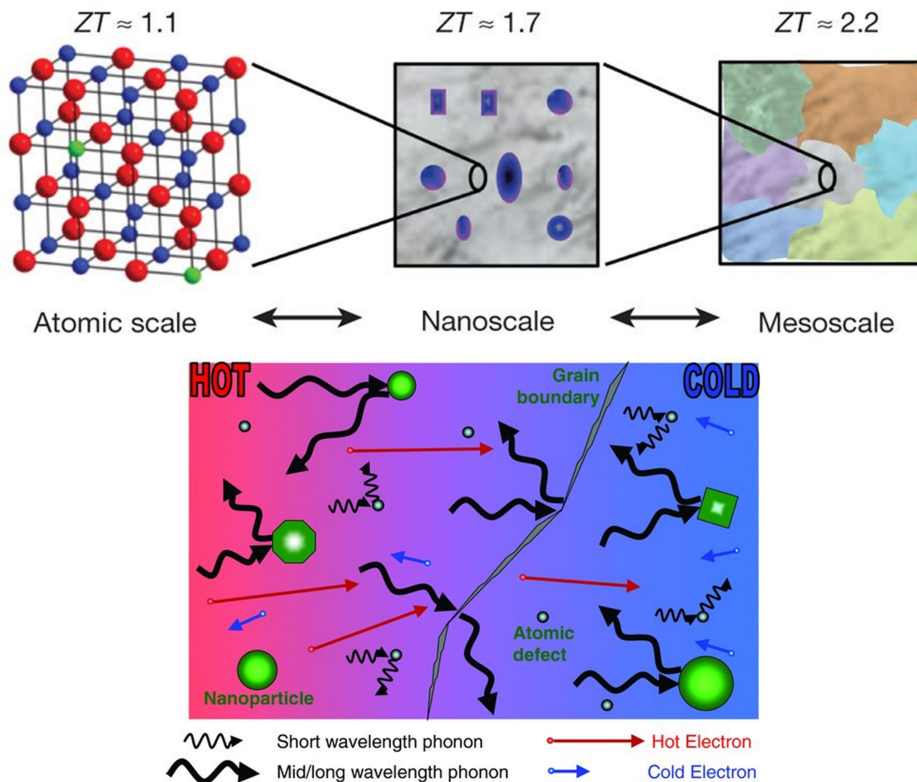
Figure 1.4 Illustration of atomic scale point defects, endotaxial nanostructures and mesoscale grain boundaries in hierarchical architectures based on PbTe that lead to an all-scale phonon scattering (upper panel). Point defects scatter short-wavelength phonons. Nanoparticles are effective at scattering mid-long wavelength phonons while grain boundaries predominantly scatter the long wavelength phonons. Schematic illustration of phonon-scattering by atomic defects, nanoparticles and grain boundaries in a solid (lower panel). The upper panel is adapted from ref. 2 © 2012 Nature publishing group and the lower panel is reproduced with permission from ref. 31 © 2010 Wiley.

1.4.2 Important 2D-Layered Metal Chalcogenides for Thermoelectrics

1.4.2.1 Bismuth Telluride

Bi_2Te_3, a narrow-gap semiconductor with an indirect band gap of ~0.15 eV, is well-known for its distinct layered crystal structure and excellent thermoelectric properties.[26, 31-33] H. Julian Goldsmid in 1954 first inspected Bi_2Te_3 as an effective material for thermoelectric refrigeration.[34] Bi_2Te_3 crystallizes in a rhombohedral layered structure (space group *R-3m*) with five atoms in one unit cell. The lattice parameters of Bi_2Te_3 are a = 0.4384 nm and c = 3.045 nm.[35] The structure is formed by quintuple layers of Te(1)-Bi-Te(2)-Bi-Te(1) stacked by van der Waals interactions along the crystallographic *c*-axis (Figure 1.5).
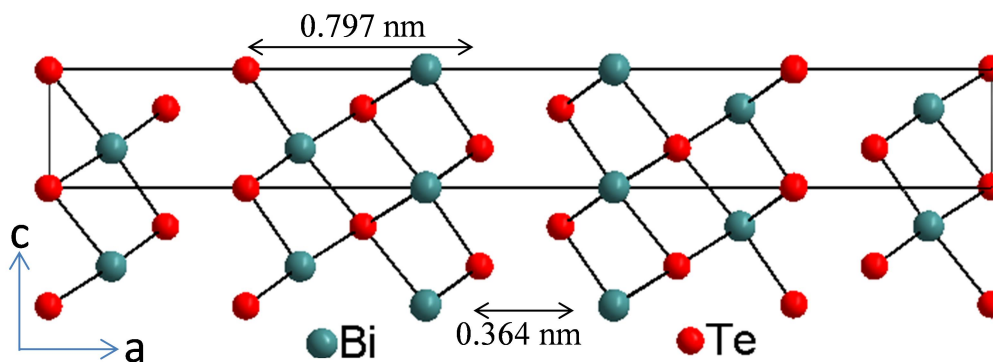
Figure 1.5 Crystal structure of Bi_2Te_3 viewed along the crystallographic b axis.

The superscript (1) and (2) denote two different chemical state of Te. The interaction between adjacent quintuple layers is due to the weak van der Waals forces. Within the quintuple layers the stronger bonds are of the covalent or partially ionic in nature.

Since the discovery of its extraordinary thermoelectric properties, Bi_2Te_3 has become a vital component for thermoelectric industry.[35-37] Bi_2Te_3-based materials are known to have the highest thermoelectric figure of merit, $zT\sim1.14$ at room temperature.[35] It was obvious from the zT expression that a significant improvement in zT can be achieved through simultaneous enhancement of the power factor, $S^2\sigma$ and decrease in the thermal conductivity. Various approaches have been tried to improve the thermoelectric properties of Bi_2Te_3 and its alloys. These approaches comprised the composition change from its stoichiometry, the use of polycrystalline materials with different grain sizes, introduction of structural defects, and incorporation of different dopants, e.g., Sb or Se, into Bi_2Te_3 lattice. Alloying with Sb_2Te_3 and Bi_2Se_3 allowed the fine tuning of the carrier concentration along with a reduction in lattice thermal conductivity of Bi_2Te_3.[3] The most commonly studied p-type composition is near $Bi_{0.5}Sb_{1.5}Te_3$, whereas n-type composition is close to $Bi_2(Te_{0.8}Se_{0.2})_3$.[3] The Bi-Sb atomic disorder in $Bi_{0.5}Sb_{1.5}Te_3$ scatters the heat-carrying phonons, thereby decreasing κ_{lat} leading to high zT values. Bi_2Te_3 nanostructures offer an exceptional model system for study
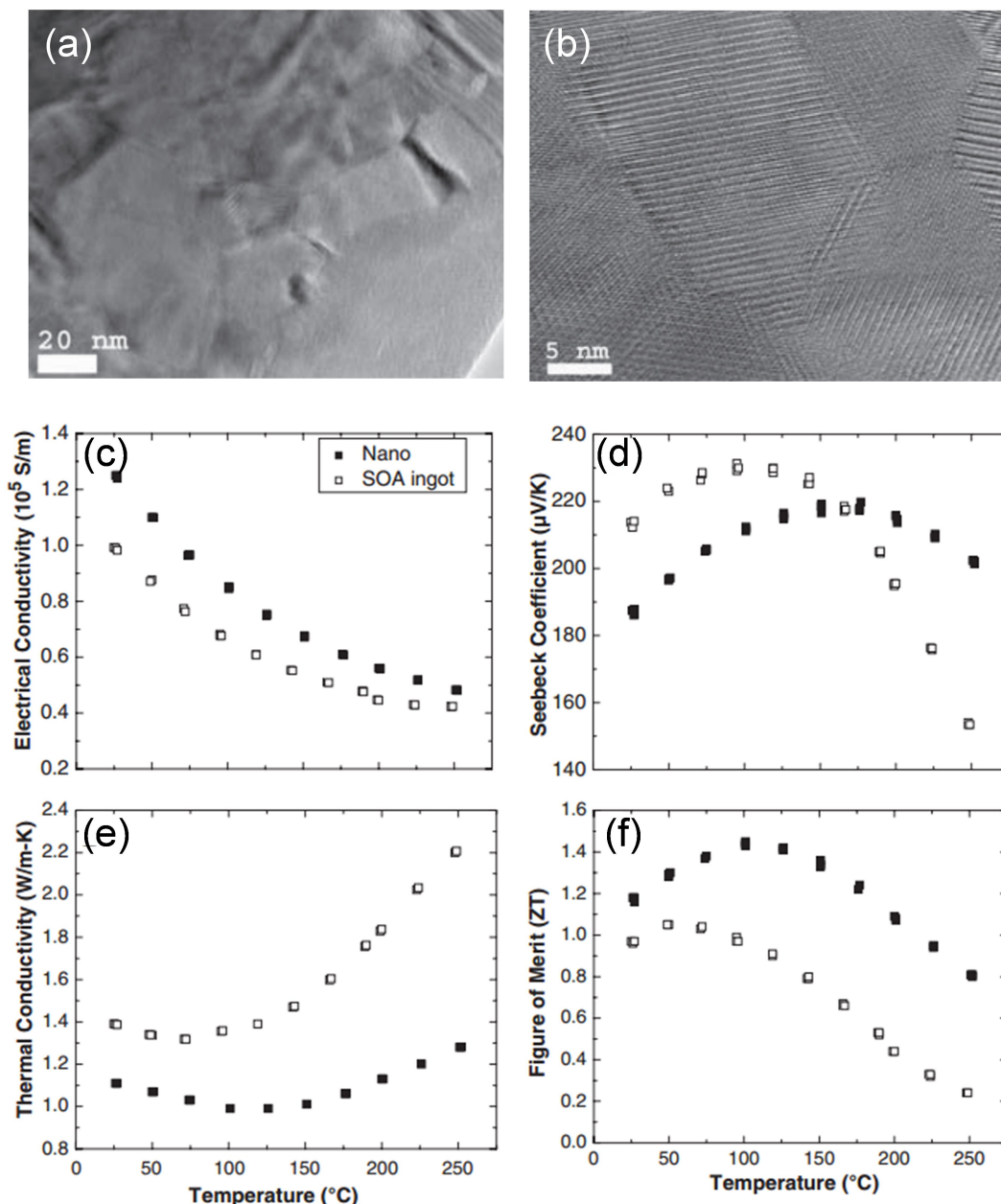
Figure 1.6 Thermoelectric properties of a hot-pressed nanocrystalline (NC) bulk bismuth antimony telluride sample. (a) Low-magnification TEM image showing the nanograins. (b) High magnification TEM image showing the nanosize, high crystallinity, random orientation and clean grain boundaries. Temperature dependence of (c) σ, (d) S, (e) κ, and (f) zT of a hot-pressed NC bulk sample (black squares) as compared with that of an state-of-the-art ingot (white squares). Adapted with permission from ref. 38 © 2012 AAAS.

-ing the preparation of nanostructured thermoelectric materials because bulk Bi_2Te_3- based materials are known to exhibit very high zT values over the temperature range of $200 - 400$ K. A remarkable increase in zT to 1.4 has been accounted in Bi_2Te_3 based nanostructured

bulk materials prepared by the hot-pressing of ball-milled nanoparticles (Figure 1.6 (f)).[38] The zT enhancement for this system occurs from reduced lattice thermal conductivity while maintaining analogous power factor compared to that of the bulk p-type $Bi_{0.5}Sb_{1.5}Te_3$. Formation of dense dislocation arrays at low-energy grain boundaries by liquid-phase compaction in $Bi_{0.5}Sb_{1.5}Te_3$ effectively scatter mid-frequency phonons, resulting in a substantially reduced lattice thermal conductivity (Figure 1.7).[39] Full-spectrum phonon scattering with minimal charge carrier scattering significantly improved the zT to 1.86 at 320 K.[39] Furthermore, a thermoelectric cooler validated the performance with a maximum temperature difference of 81 K, which is much higher than current commercial Peltier cooling devices. Z. F. Ren's group has achieved zT values of 1.04 for n-type $Bi_2Te_{3-y}Se_y$ nanostructured bulk alloy by reorienting the ab planes of the small crystals through repressing the as-pressed sample with composition $Bi_2Te_{2.7}Se_{0.3}$.[40]

The lattice spacing between layers has a direct relation with the atomic bond strength and proposed to achieve a record high zT value as a result of the confinement effects on the electronic density of states. A zT of 2.4 at room temperature has been reported for a p-type Bi_2Te_3/Sb_2Te_3 superlattice grown by chemical-vapor deposition, a value which has surpassed the long-standing $zT = 1$ record for Bi_2Te_3 alloys.[41] Because of the crystal structure, most chemically synthesized Bi_2Te_3 have two dimensional plate like shape.[40] Nanostructured Bi_2Te_3 has been prepared through top-down exfoliation technique. In order to isolate bismuth telluride quintuples and break them into atomic planes, researchers have employed a method similar to the one used for exfoliation of single-layer graphene.[35] Through a mechanical cleavage, researchers have separated nanosheets from crystalline Bi_2Te_3. The process was repeated several times to obtain layers with just a few atomic planes. Owing to the specific
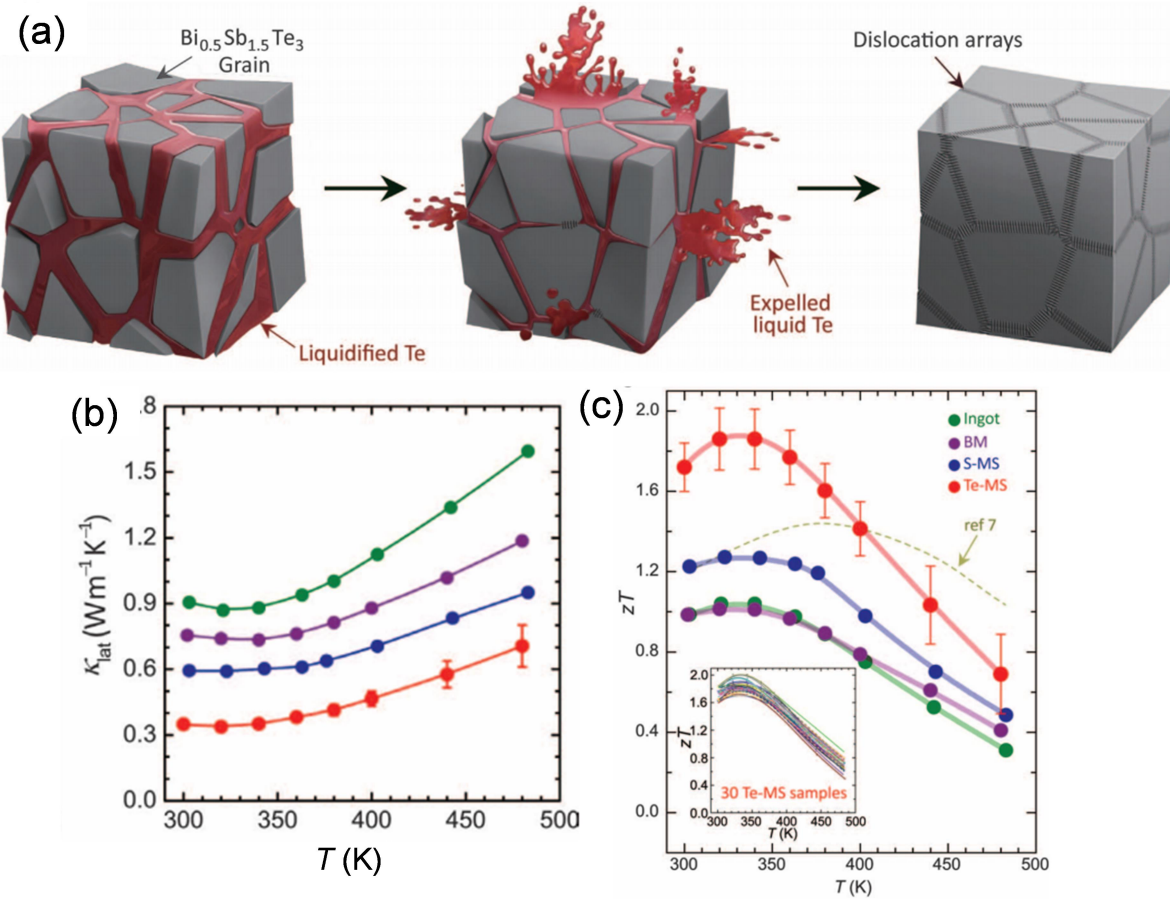
Figure 1.7 Generation of dislocation arrays at grain boundaries in $Bi_{0.5}Sb_{1.5}Te_3$. (a) Schematic illustration showing the generation of dislocation arrays during the liquid-phase compaction process. The Te liquid (red) between the $Bi_{0.5}Sb_{1.5}Te_3$ grains flows out during the compacting process and facilitates the formation of dislocation arrays embedded in low-energy grain boundaries. (b) thermal conductivity (κ_{lat}) for all samples. (c) zT as a function of temperature for $Bi_{0.5}Sb_{1.5}Te_3$ alloys. Adapted with permission from ref. 39 © 2015 AAAS.

structure of Bi_2Te_3 crystal along the c-direction, researchers have successfully verified the number of layers using atomic force microscopy (AFM) and micro-Raman spectroscopy. Top-down approaches for nanostructuring, such as ball-milling[38] and melt-spinning[42] can yield bulk quantities of high zT p-type alloys. These processes are energy consuming, and hence restrict them for production of scalable quantity high zT Bi_2Te_3.

Devising low-energy-intensity scalable methods to obtain high-zT materials of both n and p-type is crucial for fabricating commercially viable thermoelectric devices and modules for transforming the fields of solid-state refrigeration and harvesting electricity from heat.
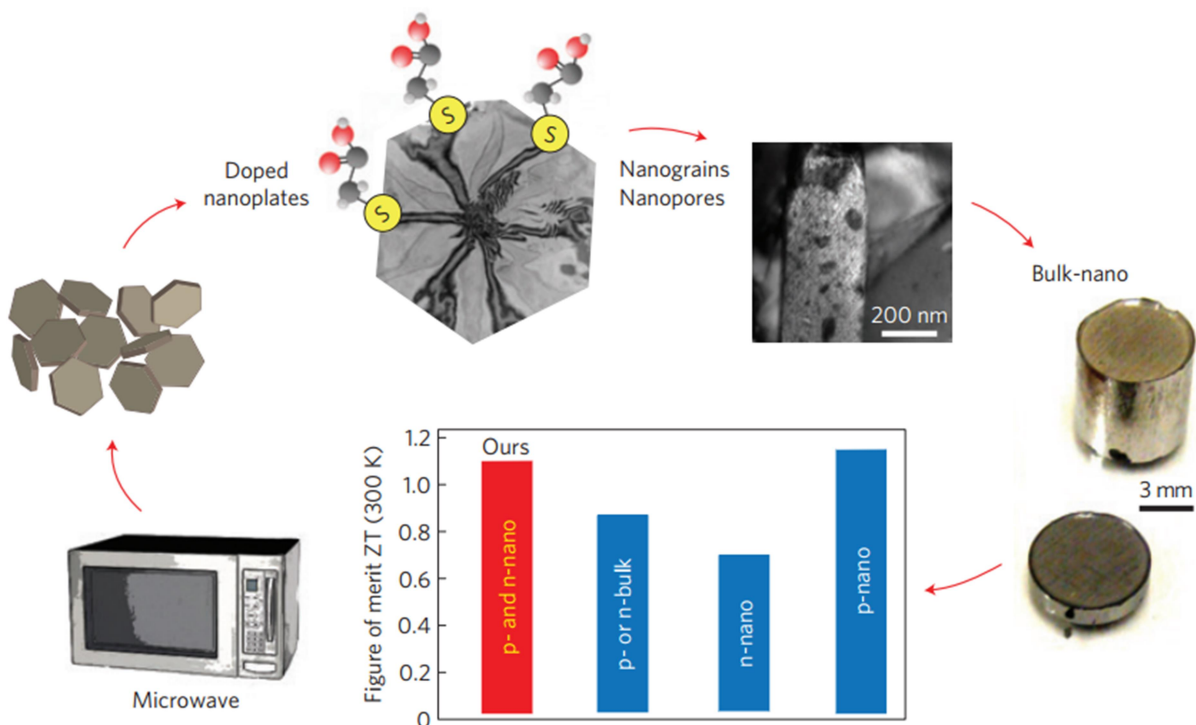
Figure 1.8 Schematic representation of the scalable synthesis used to obtain both *n*- and *p*-type bulk thermoelectric nanomaterials $Bi_2Te_{3-x}S_x$ with high *zT*. Microwave synthesis of sulphur-doped nanoplates followed by cold-compaction and sintering yields up to $92 \pm 3\%$ dense bulk pellets with nanostructured grains. Sulphur doping controls the electrical conductivity, Seebeck coefficient and majority carrier type, while nanostructuring resulted in very low thermal conductivity. The combined effect is applicable to multiple pnictogen chalcogenide systems and their combinations. The graph compares the best *zT* of *p* and *n*-type nanomaterials with those of the best *p* and *n*-bulk materials, denoted as *p* or *n*-bulk nanoparticle-dispersed *n*-bulk, referred to as *n*-nano, and a *p*-type ball-milled alloy, denoted as *p*-nano. Adapted with permission from ref. 43 © 2012 Nature Publishing Group.

Recently, bottom-up colloidal synthetic processes have been used for synthesizing large-quantities of high-quality 2D materials. These chemical methods can produce uniform-sized materials with controlled sizes which provide the possibility of achieving further improvement in thermoelectric efficiency, because in nanostructured materials both thermopower and thermal conductivity are dependent on the size and shape of the nanostructures.[43] Hence, chemically synthesized nanostructured Bi_2Te_3 has been investigated for thermoelectric applications. Ramanath's group has reported the realization of both *p*- and *n*-type nanostructured bulk materials with *zT* as high as 1.1, obtained by bottom-

up assembly of rapidly synthesized single crystal nanoplates of sulphur-doped pnictogen chalcogenides (V_2VI_3).[43] These synthetic strategies have exploited inexpensive organic solvents and metal salts as precursors ($BiCl_3$ and $SbCl_3$) for rapid preparation of large amount sulphur-doped pnictogen chalcogenide (V_2VI_3) nanocrystals to create single- and multicomponent nanostructured bulk thermoelectric materials (Figure 1.8). Microwave stimulation triggers the reaction between molecularly ligated chalcogen and pnictogen complexes with thio-glycolic acid (TGA) in the presence of a high-boiling solvent. Single component pellets prepared from pnictogen chalcogenide nanoplates showed two fold lower lattice thermal conductivity and high power factors, comparable to state of-the-art bulk alloys. This remarkable charge-carrier-crystal and phonon-glass behavior without alloying is made possible by combining nanostructuring and sub-atomic-per-cent sulphur doping. Nanostructured bulk Bi_2Te_3 obtained from single-component assemblies or nanoplate mixtures of different materials exhibit 250 % higher *zT* than their non-nanostructured bulk counterparts and state-of-the-art alloys (Figure 1.8).

In another recent work, a facile solvothermal route was developed to prepare Bi_2Te_3 nanoplates and Bi_2Te_3 nanoflowers via a chemical self-assembly route using these nanoplates as building blocks.[44a] Furthermore, to improve thermoelectric performance, high pressure route was used to sinter powder to form pellet. The resultant product was mostly hexagonal plates with uniform size of 100-200 nm diameter and thickness of ~18 nm. The pellet prepared from flower-like Bi_2Te_3 has larger Seebeck coefficient and simultaneous smaller resistivity as compared to plate-like Bi_2Te_3. The room temperature resistivity of both the samples is almost double of that of *n*-type bulk Bi_2Te_3 (1.4 mΩcm). Indeed such discrepancies in resistivity are often typical of nanocrystalline materials that possess different

degrees of disorder and formation of grain boundary barriers.[44a] The large surface-to-volume ratio of nanograins effects in high trap-state densities at each grain boundary caused by defects and dangling bonds. These trap-states immobilize charge carriers and result in a reduced mobility. Then, the grain boundaries become electrically charged and result in a grain boundary potential barrier to electronic transport. Thus, $d\sigma/dT$ can become positive at certain temperatures for grain boundary potential barriers. This is an important difference from bulk Bi_2Te_3 materials, where the negative $d\sigma/dT$ ratio forces a maximum in zT at 50 ^{o}C, preventing its application at significantly higher temperatures. This behavior of nanostructured materials has been recently predicted by Nolas and co-workers,[44b] where transport properties are dominated by grain boundary potential barrier scattering in combination with phonon scattering. The nanostructured Bi_2Te_3 shows n-type behavior with a maximum S value of ~ -150 μV/K. The observed power factor value of 8.6 $\mu Wcm^{-1}K^{-2}$ is much higher as compared to previously reported values for chemically synthesized Bi_2Te_3 nanoparticles.[44c] The room temperature thermal conductivity is ~ 0.5 $Wm^{-1}K^{-1}$. As a result, a maximum zT of 0.7 has been achieved at temperature of 180 ^{o}C.[44a]

Spark plasma sintering (SPS) is known to be very useful technique for preparing nanostructured bulk materials due to the its rapid heating and cooling rates, which allow fast sintering, preventing unnecessary grain growth arising from a long sintering process at high temperatures. Moreover, the grain growth and densification can be controlled by varying the SPS conditions, allowing the study of the effect of grain size and porosity on the thermoelectric properties of nanostructured bulk materials. Recently Hyeon and co-workers reported a colloidal synthesis of ultrathin Bi_2Te_3 nanoplates with the thickness of 1−3 nm (Figure 1.9) and subsequent SPS processing in order to fabricate n-type nanostructured bulk

thermoelectric materials.[45]

Bi$_2$Te$_3$ nanoplates were synthesized by the reaction between bismuth dodecanethiolate and tri-n-octylphosphine telluride in the presence of oleylamine.[45] It was observed that gain size and density of Bi$_2$Te$_3$ nanostructured bulk materials were strongly dependent on the SPS temperature (Figure 1.9). Accordingly, the thermoelectric properties of Bi$_2$Te$_3$ nanostructured bulk materials sintered at various temperatures were characterized to get the most favorable sintering condition for highly efficient nanostructured thermoelectric materials. The highest *zT* of 0.62 was achieved in sample sintered at 250 °C, which is one of the highest values among those of reported *n*-type nanostructured thermoelectric materials prepared from chemically synthesized nanoparticles (Figure 1.9).[45]
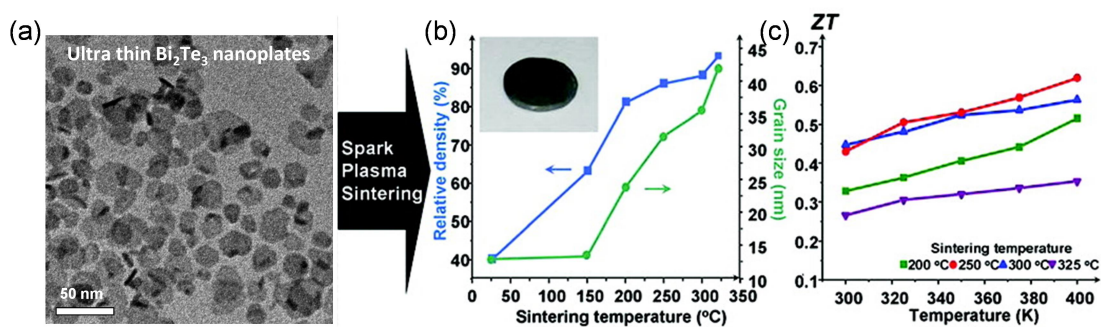
Figure 1.9 (a) TEM image shows ultrathin Bi$_2$Te$_3$ nanoplates. The density of Bi$_2$Te$_3$ nanostructured bulk materials was found to be strongly dependent on the sintering temperature. (b) Graph of relative densities (blue square) and grain sizes (red circle) has been calculated by the XRD patterns using the Scherrer equation versus sintering temperature. (c) Temperature dependence of *zT* of Bi$_2$Te$_3$ nanostructured bulk materials sintered at 200 °C (green square), 250 °C (red circle), 300 °C (blue upward triangle), and 325 °C (purple downward triangle). Adapted with permission from ref. 45 © 2012 American Chemical Society.

1.4.2.2 Bismuth Selenide

Bi$_2$Se$_3$ is a V-VI semiconductor with a narrow band gap of ~0.3 eV, which has potential application in optical recording system, photo-electrochemical devices, and thermoelectrics.[46-50] Like Bi$_2$Te$_3$, it is also a 3D topological insulator with metallic surface states protected by the time reversal symmetry.[48] Bi$_2$Se$_3$ is an anisotropic layered material

(R-3m space group and crystal structure is same as Bi_2Te_3) containing quintuple layers (QL) each of approximately 1 nm thick and composed of five covalently bonded atomic planes [Se2-Bi-Se1-Bi-Se2]. Atomically thin layers of Bi_2Se_3 are important candidate for thermoelectrics. In addition, the attraction of Bi_2Se_3 also comes from its unique 2D electron gas like nature that covers the whole surface, thus contributing to the metallic surface states. This suppresses the electron backscattering, ensuring a high μ of ~6000 $cm^2V^{-1}s^{-1}$ and a Fermi velocity of~$5×10^5$m/s.[48-50] The 2D electron gas and the effective phonon scattering at the grain boundaries and interfaces enable the Bi_2Se_3 single-layer-based composite to achieve improved σ and S as well as reduction in κ, thereby leading to an enhancement of zT as compared to bulk material (Figure 1.10).
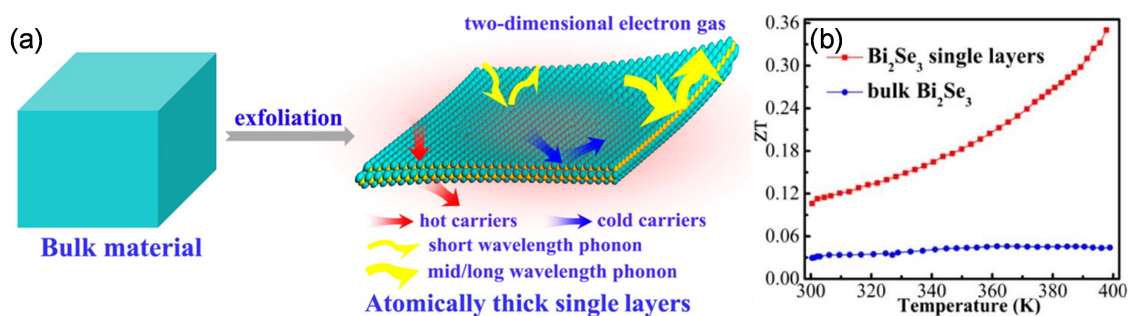
Figure 1.10 (a) Schematic representation of exfoliation technique and representation of transport properties of Bi_2Se_3 single layer. (b) Temperature dependent ZT of bulk and single layered Bi_2Se_3. Adapted with permission from ref. 50 © 2012 American Chemical Society.

Y. Xie and co-workers first reported the synthesis of isolated five-atom-thick Bi_2Se_3 single layers via a scalable intercalation/exfoliation strategy, which takes advantage of an intermediate precursor (Li-intercalated Bi_2Se_3 microplates).[50] The Bi_2Se_3 single-layer-based (SLB) composite exhibited a significant enhancement in electric transport properties and a much lower thermal conductivity than that of the bulk material over the entire temperature range. Hence, the σ/κ ratio for the SLB composite is higher than that for the bulk material over the whole temperature range. |S| for the SLB composite gradually increases from 90

μV/K at 300 K to 121 μV/K at 400 K, which is a factor of 1.2 greater than that of bulk material (98.5 μV/K). The power factor (σS^2) of the SLB composite is greater than that of the bulk material, which could be a benefit of the simultaneously increased σ and S values. Hence, zT for the SLB composite is higher than that for the bulk material over the whole temperature range. In particular, the SLB composite exhibits $zT = 0.35$ at 400 K, which is 8 times larger than zT of the bulk material and higher than the previously reported values for pure Bi_2Se_3 nanostructures, suggesting the superiority of the atomically thick SLB structure (Figure 1.10).

Jana *et al.* has studied the thermoelectric properties of few-layer nanosheets of Bi_2Se_3, synthesized via a green ionothermal method in the water-soluble, room-temperature ionic liquid, 1-ethyl-3-methylimidazolium tetrafluoroborate ([EMIM][BF$_4$]).[51] Ionothermal reaction of bismuth acetate and selenourea in [EMIM][BF$_4$] yields ultrathin (3–5 layer) Bi_2Se_3 nanosheets. The high electrical conductivity is attributed to the presence of surface states that offer high mobility and scattering-resistant carriers. In addition to this surface defects, nanoscale grain boundaries and interfaces effectively scatter the heat carrying phonons, thereby decreasing κ_{total} to as low as 0.4 Wm^{-1}K^{-1} near room temperature. As a result maximum zT of 0.1 has been observed near room temperature.

1.4.2.3 Tin Selenide

SnSe is a layered material, adopt a orthorhombic crystal structure, which can be derived from a three-dimensional distortion of the NaCl structure (Figure 1.11).[27, 52-54] At high temperature the low symmetry *Pnma* phase undergoes a displacive phase transition to a high symmetry *Cmcm* phase.[55-59] The two-atom-thick SnSe slabs are folded up and create a zig zag accordion like projection along the crystallographic *b* axis. In both the structures

these identical layers are weakly bound (weak van der Waals interaction) and resulting in an anisotropic layered structure (Figure 1.11).[58, 59]
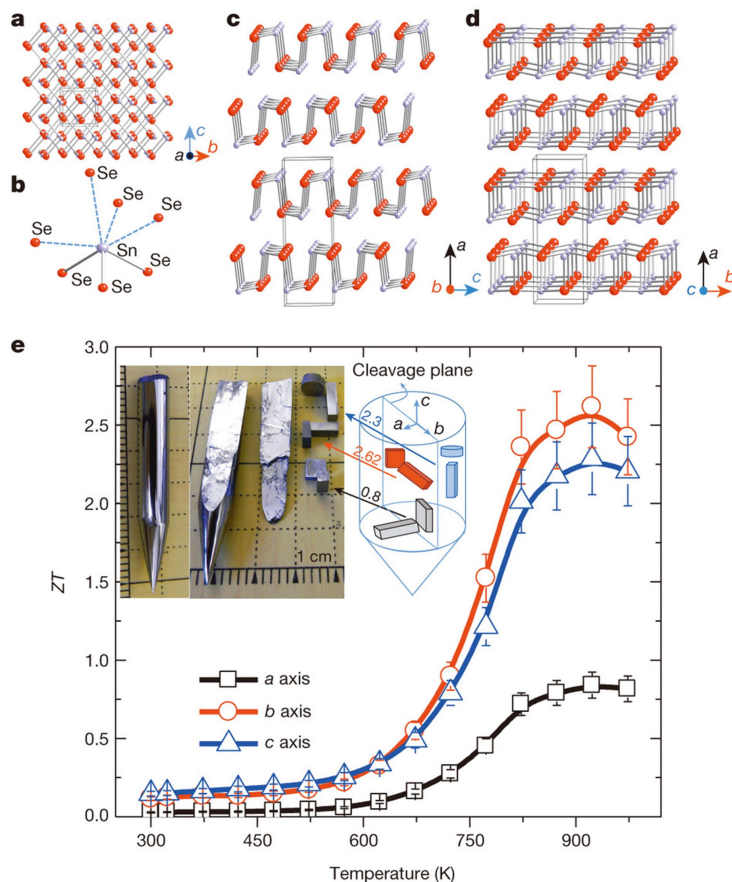
Figure 1.11 (a) Crystal structure of SnSe along the crystallographic *a* axis: grey, Sn atoms; red, Se atoms. (b) Highly distorted SnSe$_7$ coordination polyhedron with three short and four long Sn–Se bonds. (c) Structure along the *b* axis. (d) Structure along the *c* axis. (e) Main panel, *zT* values along different axial directions; the *zT* measurement uncertainty is about 15% (error bars). Inset images: left, a typical crystal; right, a crystal cleaved along the (l00) plane, and specimens cut along the three axes and corresponding measurement directions. Inset diagram, how crystals were cut for directional measurements; *zT* values are shown on the blue, red and grey arrows; colours represent specimens oriented in different directions. Adapted with permission from ref. 27 © 2014 Nature Publishing Group.

Zhao and Kanatzidis have extensively investigated the thermoelectric properties of single crystalline SnSe at different crystallographic direction. They are able to achieve a record high *zT* value up to ~2.6 along in-plane direction in *p*-type SnSe single crystals[27] and *zT* value of ~2.8 at 773K along out-of-plane direction in *n*-type Br-doped SnSe single crystals[54] due to moderate power factor and ultra-low thermal conductivity (Figure 1.11). Thereafter

investigations on the thermoelectric properties of SnSe gain a significant attention.[59] Recently, it has been shown that excellent average zT value can be obtained in Na doped p-type SnSe single crystal due to increase in the σ value.[58] Moreover Bi doped n-type SnSe single crystals also show a high zT of 2.2 at 723K[60] (Figure 1.12).
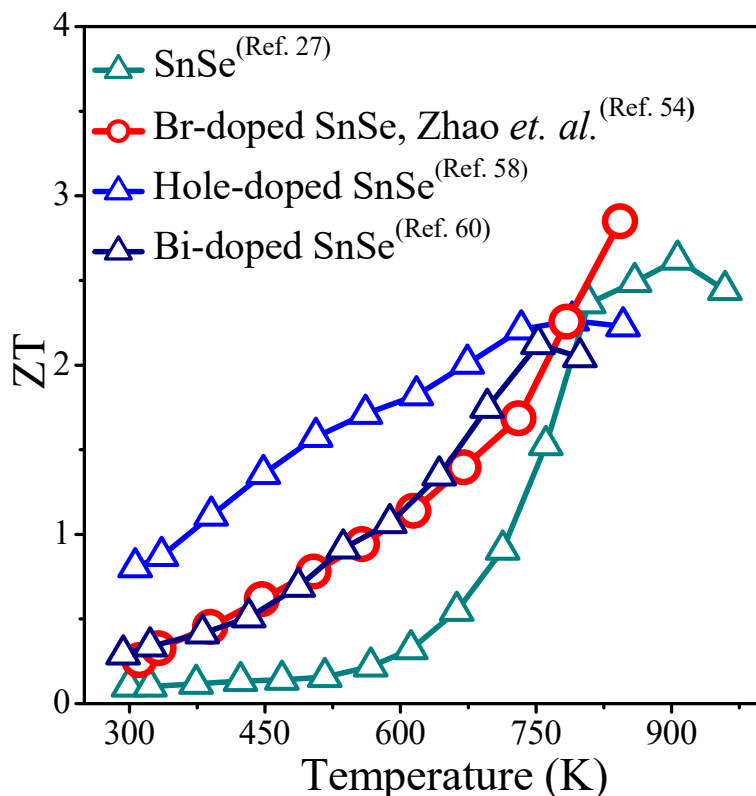
Figure 1.12 Comparative study of thermoelectric figure of merit of various SnSe single crystals.

The single-crystalline nanosheets of SnSe with four-atomic thickness were synthesized for the first time in 2013 by Li et $al.$[61] Recently, a theoretical investigation claims that a zT value as high as 3.3 in single-layered SnSe nanosheet along the armchair and 2.76 along zigzag direction, respectively, with optimal n-type carrier concentration at 700 K.[53] However, detail experimental work is required for practical realization.

1.4.2.4 Germanium Selenide

GeSe crystallizes in three different structures: orthorhombic (*Pnma*), rhombohedral

($R3m$), and cubic phases ($Fm\bar{3}m$; Figure 1.13) depending on the temperature and pressure conditions.[62, 63] At ambient conditions, GeSe has the orthorhombic structure similar to that of SnSe, which shows an unprecedented zT in the single-crystal form owing to ultralow thermal conductivity. Recently, by using first-principles density functional calculations, Hao *et.al.* predicted the high thermoelectric performance in GeSe through carrier engineering.[64] However, the orthorhombic GeSe is experimentally found to be a *p*-type semiconductor with poor thermoelectric performance.[65]
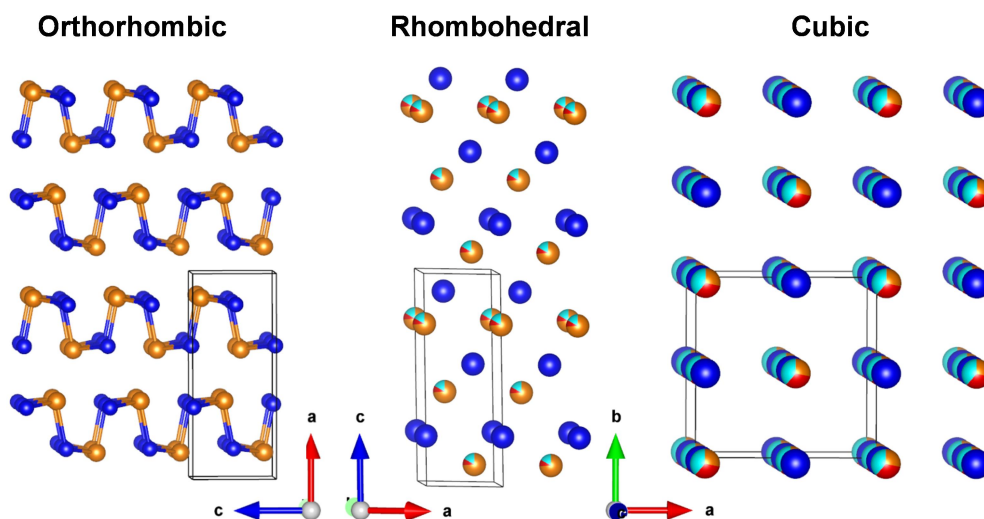
Figure 1.13 Crystal structure of different phases of GeSe: orthorhombic (O), rhombohedral (R), and cubic (C). Ge Yellow, Se Blue; Ag Red, Bi Cyan). Adapted with permission from ref. 67 © 2018 Angewandte Chemie Publishing Group.

Recently, Huang *et. al.*[62] have been able to stabilize the *p*-type rhombohedral GeSe by alloying it with AgSbSe$_2$, which showed a zT of 0.86 at 710K in GeAg$_{0.2}$Sb$_{0.2}$Se$_{1.4}$. They have achieved a low κ_L of 0.9W m^{-1} K^{-1}, which is, however, still higher than the theoretical κ_{min} of GeSe (0.4 W m^{-1} K^{-1}).[65a] The room-temperature orthorhombic GeSe undergoes to a first-order structural transition to a face-centered cubic (FCC) structure (Figure 1.13) at 920K.[66] This cubic phase of GeSe is unstable at ambient conditions because of the presence of several imaginary vibration modes in its phonon dispersion. Theoretical

calculations, however, indicate that the application of external pressure of 7 GPa would lead to the stabilization of the cubic phase.[63] The high-symmetry cubic phases are in general much sought-after for high-performance thermoelectrics as they possess degenerate electronic band valleys.
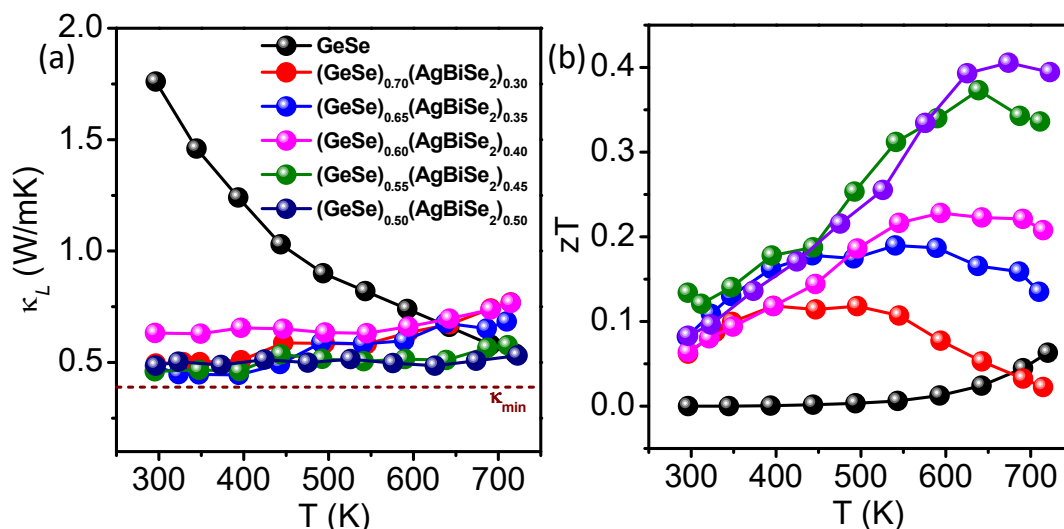
Figure 1.14 Temperature-dependent (a) lattice thermal conductivity (κ_L) and (b) thermoelectric figure of merit (zT) of (GeSe)$_{1-x}$(AgBiSe$_2$)$_x$ (x=0–0.50). Adapted with permission from ref. 67 © 2018 Angewandte Chemie Publishing Group.

Recently, Roychowdhury *et. al.*[67] have shown ultralow lattice thermal conductivity (κ_L) of 0.43 W m^{-1} K^{-1} in GeSe by alloying with AgBiSe$_2$ (Figure 1.14 (a)) and they have obtained a zT of 0.45 at 677 K (Figure 1.14 (b)) in *n*-type (GeSe)$_{0.50}$(AgBiSe$_2$)$_{0.50}$. Ultralow thermal conductivity is attributed to the enhanced point defect phonon scattering owing to entropy-driven extended solid solutions. This report establishes cubic (GeSe)$_{1-x}$(AgBiSe$_2$)$_x$ as a promising *n*-type thermoelectric material and there are further scopes to improve the thermoelectric performance of these GeSe based thermoelectric materials.

1.5 Motivation of the Thesis

In this chapter, I have discussed about the key concepts, latest development and under

-standing of the thermoelectric properties of layered chalcogenides. We have learned that layered Bi_2Te_3 is one of the leading thermoelectric material for near room temperature applications, while layered SnSe demonstrates remarkably high *zT* of ~2.6 at 923 K in the form of single crystals, which is a potential candidate for the high temperature power generation. However, polycrystalline SnSe is a better choice for thermoelectric applications for the ease of its production and machinability. Though, in most of the cases, reported SnSe materials are *p*-type while thermoelectric applications demand for both *p*-type and *n*-type materials. Generally, layered metal chalcogenides show interracially low thermal conductivity due to anisotropic structure and strong lattice anharmonicity. The studies on the thermoelectric properties of layered chalcogenides are progressive and this is an open area of research. Although the thermal conductivity is intrinsically low for layered chalcogenides, attention should be given on improving the Seebeck coefficient by various innovative approaches such as electronic band valley convergence and exploration of resonance level in the electron structure. Many new layered materials with promising thermoelectric properties have been discovered, although a lot of work and progress need to be done for their practical realization in the form of thermoelectric module. In this context, the combine effort of chemist, physics, materials scientists and engineers will be highly worthy.

References

[1]   Source: Indian Energy Consumption Grew in 2017, Energy Transition Statics, Indian Central Electricity Authority.

[2]   Biswas, K.; He, J.; Blum, I. D.; Wu, C.-I.; Hogan, T. P.; Seidman, D. N.; Dravid, V. P.; Kanatzidis, M. G., High-performance bulk thermoelectrics with all-scale hierarchical architectures. *Nature* **2012**, *489*, 414.

[3]   Snyder, G. J.; Toberer, E. S., Complex thermoelectric materials. *Nat. Mater.***2008**, *7*, 105.

[4]   Sootsman, J.; Chung, D. Y.; Kanatzidis, M. G., New and Old Concepts in Thermoelectric Materials. *Angew. Chem. Int. Ed.* **2009**, *48*, 8616.

[5]   Seebeck, A., Thomson's dilemma. *Ann. Chim. Phys.* **1826**, *56*, 133.

[6]   Tritt, T. M.; Subramanian, M. A., Thermoelectric Materials, Phenomena, and Applications: A Bird's Eye View. *Mater. Res. Soc. Bull.* **2006**, *31*, 188.

[7]   Altenkirsch, E. *E.,* The bridge between the materials and devices of thermoelectric power generators. *Phys. Z.* **1909**, *10*, 560.

[8]   Chen, G.; Dresselhaus, M. S.; Dresselhaus, G.; Fleurial, J. P.; Caillat, T., Recent developments in thermoelectric materials. *Int. Mater. Rev.* **2003**, *48*, 45.

[9]   DiSalvo*,* F. J., Thermoelectric cooling and power generation. *Science* **1999***, 285,* 703.

[10]   Biswas, K.; He, J.; Zhang, Q.; Wang, G.; Uher, C.; Dravid, V. P.; Kanatzidis, M. G., Strained endotaxial nanostructures with high thermoelectric figure of merit. *Nat. Chem.* **2011**, *3*, 160.

[11]   Zhao, L. D.; Dravid, V. P.; Kanatzidis, M. G., The panoscopic approach to high performance thermoelectrics. *Energy Environ. Sci.* **2014**, *7*, 251.

[12] Vedernikov, M. V.; Iordanishvili, E. K. *17th Int. Conf. on Thermoelectrics* **1998**, *1*, 37.

[13] Chung, D. Y.; Iordanidis, L.; Choi, K. S.; Kanatzidis, M. G., Complex chalcogenides as thermoelectric materials: a solid state chemistry approach. *Bull. Korean Chem. Soc.* **1998**, *19*, 1283.

[14] Tritt, T. M., Thermoelectric phenomena, materials, and applications. *Ann. Rev. Mater. Res.* **2011**, *41*, 433.

[15] Li, J. -F.; Liu, W. -S.; Zhao, L. -D.; Zhou, M., High-performance nanostructured thermoelectric materials. *NPG Asia Mater.* **2010**, *2*, 152.

[16] Tan, G.; Zhao, L.-D.; Kanatzidis, M. G., Rationally Designing High-Performance Bulk Thermoelectric Materials. *Chem. Rev.* **2016**, *116*, 12123.

[17] Chhowalla, M.; Shin, H. S.; Eda, G.; Li, L.-J.; Loh, K. P.; Zhang, H., The chemistry of two-dimensional layered transition metal dichalcogenide nanosheets. *Nat. Chem.* **2013,** 5, 263.

[18] Kanatzidis, M. G., Structural Evolution and Phase Homologies for "Design" and Prediction of Solid-State Compounds. *Accounts of Chemical Research* **2005,** 38, 359.

[19] Mas-Balles, R.; Gomez-Navarro, C.; Gomez-Herrero, J.; Zamora, F., 2D materials: to graphene and beyond. *Nanoscale* **2011,** *3*, 20.

[20] Rao, C. N. R.; Ramakrishna Matte, H. S. S.; Maitra, U., Graphene analogues of inorganic layered materials. *Angew. Chem. Int . Ed.* **2013,** *52*, 13162.

[21] Gupta, A.; Sakthivel, T.; Seal, S.; Recent development in 2D materials beyond graphene. *Prog. Mater. Sci.* **2015,** *73*, 44.

[22] Sun, Y.; Gao, S.; Xie, Y., Atomically- thick two dimensional crystals: electronic structure regulation and energy device construction. *Chem. Soc. Rev.* **2014,** *43*, 530.

[23] Geim, A. K.; Grigorieva, I. V., Van der Waals heterostructures. *Nature* **2013,** *499*, 419.

[24] Schedin, F.; Geim, A. K.; Morozov, S. V.; Hill, E. W.; Blake, P.; Katsnelson, M. I.; Novoselov, K. S., Detection of individual gas molecules adsorbed on graphene. *Nature Mat.* **2007,** *6*, 652.

[25] Novoselov, K. S.; Jiang, D.; Schedin, F.; Booth, T. J.; Khotkevich, V. V.; Morozov, S. V.; Geim, A. K., Two-dimensional atomic crystals. *Proc. Natl. Acad. Sci. U.S.A.* **2005,** *102*, 10451.

[26] Zebarjadi, M.; Esfarjani, K.; Dresselhaus, M. S.; Ren, Z. F.; Chen, G., Perspectives on thermoelectrics: from fundamentals to device applications. *Energy Environ. Sci.* **2012,** *5*, 5147.

[27] Zhao, L.-D.; Lo, S.-H.; Zhang, Y.; Sun, H.; Tan, G.; Uher, C.; Wolverton, C.; Dravid, V. P.; Kanatzidis, M. G., Ultralow thermal conductivity and high thermoelectric figure of merit in SnSe crystals. *Nature* **2014,** *508*, 373.

[28] Hicks, L. D.; Dresselhaus, M. S., Effect of quantum-well structures on the thermoelectric figure of merit. *Phys. Rev. B* **1993,** *47*, 12727.

[29] Dresselhaus, M. S.; Chen, G.; Tang, M. Y.; Yang, R.; Lee, H.; Wang, D.; Ren, Z.; Fleurial, J. P.; Gogna P., New Directions for Low-Dimensional Thermoelectric Materials. *Adv. Mater.* **2007,** *19*, 1043.

[30] Dresselhaus, M. S.; Dresselhaus, G.; Sun, X.; Zhang, Z.; Cronin, S. B.; Koga, T., Low-dimensional thermoelectric materials. *Phys. Solid State* **1999,** *41*, 1063.

[31] Vineis, C. J.; Shakouri, A.; Majumdar, A.; Kanatzidis, M. G., Nanostructured Thermoelectrics:Big Efficiency Gains from Small Features. *Adv. Mater.* **2010,** *22*, 3970.

[32] Tritt, T. M., Holey and Unholey Semiconductors. *Science* **1999,** *283*, 804.

[33] Nolas, G. S.; Sharp, J.; Goldsmid, H. J., Thermoelectrics Basic Principles and New Materials Development. *Springer: Berlin, Germany*, **2001**.

[34] Goldsmid, H. J.; Douglas, R. W., The use of semiconductors in thermoelectric refrigeration. *J. Appl. Phys.* **1954,** *5*, 386.

[35] Teweldebrhan, D.; Goyal, V.; Balandin, A. A., Exfoliation and Characterization of Bismuth Telluride Atomic Quintuples and Quasi-Two-Dimensional Crystals. *Nano Letters* **2010,** *10*, 1209.

[36] Ioffe, A. F. Semiconductor Thermoelements; Nauka: Moscow, **1956** (in Russian) or Ioffe, A. F. Semiconductor Thermoelectric and Thermoelectric Cooling; *Info search*: London, **1957**.

[37] Wright, D. A., Thermoelectric Properties of Bismuth Telluride and its Alloys. *Nature* **1958,** *181*, 834.

[38] Poudel, B.; Hao, Q.; Ma, Y.; Lan, Y.; Minnich, A.; Yu, B.; Yan, X.; Wang, D.; Muto, A.; Vashaee, D.; Chen, X.; Liu, J.; Dresselhaus, M. S.; Chen, G.; Ren, Z., High-Thermoelectric Performance of Nanostructured Bismuth Antimony Telluride Bulk Alloys. *Science* **2008,** *320*, 634.

[39] Kim, S. I.; Lee, K. H.; Mun, H. A.; Kim, H. S.; Hwang, S. W.; Roh, J. W.; Yang, D. J.; Shin, W. H.; Li, X. S.; Lee, Y. H.; Snyder, G. J.; Kim, S. W., Thermoelectrics. Dense dislocation arrays embedded in grain boundaries for high-performance bulk thermoelectrics. *Science* **2015,** *348*, 109.

[40] Yan, X.; Poudel, B.; Ma, Y.; Liu, W. S.; Joshi, G.; Wang, H.; Lan, Y.; Wang, D.; Chen, G.; Ren, Z. F., Experimental Studies on Anisotropic Thermoelectric Properties and Structures of *n*-Type $Bi_2Te_{2.7}Se_{0.3}$. *Nano Letters* **2010,** *10*, 3373.

[41] Venkatasubramanian, R.; Siivola, E.; Colpitts, T.; O'Quinn, B., Thin-film thermoelectric devices with high room-temperature figures of merit. *Nature* **2001,** *413*, 597.

[42] Wenjie, X.; Xinfeng, T.; Yonggao, Y.; Qingjie, Z.; Terry, M. T., High thermoelectric performance BiSbTe alloy with unique low-dimensional structure. *J. Appl. Phys.* **2009,** *105*, 113713.

[43] Mehta, R. J.; Zhang, Y.; Karthik, C.; Singh, B.; Siegel, R. W.; Borca-Tasciuc, T.; Ramanath, G., A new class of doped nanobulk high-figure-of-merit thermoelectrics by scalable bottom-up assembly. *Nat. Mater.* **2012,** *11*, 233.

[44] (a) Fu, J.; Song, S.; Zhang, X.; Cao, F.; Zhou, L.; Li, X.; Zhang, H., Bi_2Te_3 nanoplates and nanoflowers: Synthesized by hydrothermal process and their enhanced thermoelectric properties. *CrystEngComm* **2012,** *14*, 2159. (b) Martin, J.; Wang, L.; Chen, L.; Nolas, G. S., Enhanced Seebeck coefficient through energy-barrier scattering in PbTe nanocomposites. *Phys. Rev. B* **2009,** *79*, 115311 (c) Wang, R. Y.; Feser, J. P.; Gu, X.; Yu, K. M.; Segalman, R. A.; Majumdar, A.; Milliron, D. J.; Urban, J. J., Universal and Solution-Processable Precursor to Bismuth Chalcogenide Thermoelectrics. *Chem. Mater.* **2010,** *22*, 1943.

[45] Son, J. S.; Choi, M. K.; Han, M.-K.; Park, K.; Kim, J.-Y.; Lim, S. J.; Oh, M.; Kuk, Y.; Park, C.; Kim, S.-J.; Hyeon, T., n-Type Nanostructured Thermoelectric Materials Prepared from Chemically Synthesized Ultrathin Bi_2Te_3 Nanoplates. *Nano Lett.* **2012,** *12*, 640.

[46] Larson, P.; Greanya, V. A.; Tonjes, W. C.; Liu, R.; Mahanti, S. D.; Olson, C. G., Electronic structure of Bi_2X_3 (X = S, Se, Te) compounds: Comparison of theoretical calculations with photoemission studies. *Phys. Rev. B* **2002,** *65*, 085108.

[47] Urazhdin, S.; Bilc, D.; Tessmer, S. H.; Mahanti, S. D.; Kyratsi, T.; Kanatzidis, M. G., Scanning tunneling microscopy of defect states in the semiconductor Bi_2Se_3. *Phys. Rev. B* **2002,** *66*, 161306.

[48] Woollam, J. A.; Beale, H. A.; Spain, I. L., Bi_2Se_3 Hall Effect Magnetometer for Reliable Low Temperature Use. *Rev. Sci. Instrum*. **1973,** *44*, 434.

[49] Du, Y.; Shen, S. Z.; Cai, K. F.; Casey, P. S., Research progress on polymer–inorganic thermoelectric nanocomposite materials. *Prog. Polym. Sci.* **2012,** *37*, 820.

[50] Sun, Y.; Cheng, H.; Gao, S.; Liu, Q.; Sun, Z.; Xiao, C.; Wu, C.; Wei, S.; Xie, Y., Atomically Thick Bismuth Selenide Freestanding Single Layers Achieving Enhanced Thermoelectric Energy Harvesting. *J. Am. Chem. Soc.* **2012**, *134*, 20294.

[51] Jana, M. K.; Biswas, K.; Rao, C. N. R., Ionothermal Synthesis of Few-Layer Nanostructures of Bi_2Se_3 and Related Materials. *Chem. Eur. J.* **2013**, *19*, 9110.

[52] Baumgardner, W. J.; Choi, J. J.; Lim, Y.-F.; Hanrath, T., SnSe Nanocrystals: Synthesis, Structure, Optical Properties, and Surface Chemistry. *J. Am. Chem. Soc.* **2010**, *132*, 9519.

[53] Wang, F. Q.; Zhang, S.; Yu, J.; Wang, Q., Thermoelectric properties of single-layered SnSe sheet. *Nanoscale* **2015,** *7*, 15962.

[54] Chang, C.; Wu, M.; He, D.; Pei, Y.; Wu, C.-F.; Wu, X.; Yu, H.; Zhu, F.; Wang, K.; Chen, Y.; Huang, L.; Li, J.-F.; He, J.; Zhao, L.-D., 3D charge and 2D phonon transports leading to high out-of-plane ZT in n-type SnSe crystals. *Science* **2018**, *360*, 778.

[55] Sassi, S.; Candolfi, C.; Vaney, J. B.; Ohorodniichuk, V.; Masschelein, P.; Dauscher, A.; Lenoir, B., Transport Properties of Polycrystalline *p*-type SnSe. *Mater. Today* **2015**, *2*, 690.

[56] Chen, C.-L.; Wang, H.; Chen, Y.-Y.; Day, T.; Snyder, G. J., Thermoelectric properties of p-type polycrystalline SnSe doped with Ag. *J. Mater. Chem. A* **2014,** *2*, 11171.

[57] Sassi, S.; Candolfi, C.; Vaney, J. B.; Ohorodniichuk, V.; Masschelein, P.; Dauscher, A.; Lenoir, B., Assessment of the thermoelectric performance of polycrystalline *p*-type SnSe. *Appl. Phys. Lett.* **2014,** *104*, 212105.

[58] Zhao, L. D.; Tan, G.; Hao, S.; He, J.; Pei, Y.; Chi, H.; Wang, H.; Gong, S.; Xu, H.; Dravid, V. P.; Uher, C.; Snyder, G. J.; Wolverton, C.; Kanatzidis, M. G., Ultrahigh power factor and thermoelectric performance in hole-doped single-crystal SnSe. *Science* **2016**, *351*, 141.

[59] Peng, K.; Lu, X.; Zhan, H.; Hui, S.; Tang, X.; Wang, G.; Dai, J.; Uher, C.; Wang, G.; Zhou, X., Broad temperature plateau for high ZTs in heavily doped *p*-type SnSe single crystals. *Energy Environ. Sci.* **2015,** *9*, 454.

[60]   Duong, A. T.; Nguyen, V. Q.; Duvjir, G.; Duong, V. T.; Kwon, S.; Song, J. Y.; Lee, J. K.; Lee, J. E.; Park, S.; Min, T.; Lee, J.; Kim, J.; Cho, S., Achieving ZT=2.2 with Bi-doped n-type SnSe single crystals. *Nat. Commun.* **2016**, *7*, 13713.

[61] Li, L.; Chen, Z.; Hu, Y.; Wang, X.; Zhang, T.; Chen, W.; Wang, Q., Single-Layer Single-Crystalline SnSe Nanosheets. *J. Am. Chem. Soc.* **2013,** *135*, 1213.

[62] Huang, Z.; Miller, S. A.; Ge, B.; Yan, M.; Anand, S.; Wu, T.; Nan, P.; Zhu, Y.; Zhuang, W.; Snyder, G. J.; Jiang, P.; Bao, X., High Thermoelectric Performance of New Rhombohedral Phase of GeSe stabilized through Alloying with $AgSbSe_2$. *Angew. Chem. Int. Ed.* **2017,** *56*, 14113.

[63] Deringer, V. L.; Stoffel, R. P.; Dronskowski, R., Vibrational and thermodynamic propert-ies of GeSe in the quasiharmonic approximation. *Phys. Rev. B* **2014,** *89*, 094303.

[64] Hao, S.; Shi, F.; Dravid, V. P.; Kanatzidis, M. G.; Wolverton, C., Computational Prediction of High Thermoelectric Performance in Hole Doped Layered GeSe. *Chem. Mater.* **2016,** *28*, 3218.

[65] (a) Zhang, X.; Shen, J.; Lin, S.; Li, J.; Chen, Z.; Li, W.; Pei, Y., Thermoelectric properties of GeSe. *J. Materiomics* **2016,** *2*, 331; (b) Hughes, M. A.; Fedorenko, Y.; Gholipour, B.; Yao, J.; Lee, T.-H.; Gwilliam, R. M.; Homewood, K. P.; Hinder, S.; Hewak, D. W.; Elliott, S. R.; Curry, R. J., *n*-type chalcogenides by ion implantation. *Nat. Commun.* **2014,** *5*, 5346.

[66] Sist, M.; Gatti, C.; Nørby, P.; Cenedese, S.; Kasai, H.; Kato, K.; Iversen, B. B., High-Temperature Crystal Structure and Chemical Bonding in Thermoelectric Germanium Selenide (GeSe). *Chem. Eur. J.* **2017,** *23*, 6888.

[67] Roychowdhury, S.; Ghosh, T.; Arora, R.; Waghmare, U. V.; Biswas, K., Stabilizing n-Type Cubic GeSe by Entropy-Driven Alloying of AgBiSe$_2$: Ultralow Thermal Conductivity and Promising Thermoelectric Performance. *Angew. Chem. Int. Ed.* **2018**, *130*, 15387.

Chapter 2

Realization of High Thermoelectric Figure of Merit in Solution Synthesized p-type 2D SnSe Nanoplates via Ge Alloying*

---

* Manuscript based on this study is currently under revision.

Realization of High Thermoelectric Figure of Merit in Solution Synthesized *p*-type 2D SnSe Nanoplates via Ge Alloying

Summary: *Recently single crystals of layered SnSe has created a paramount importance in thermoelectrics owing to their ultralow lattice thermal conductivity and high thermoelectric figure of merit (zT). However, nanocrystalline or polycrystalline SnSe offers a wide range of thermoelectric applications for the ease of its synthesis and machinability. Here, we have demonstrated high zT of 2.1 at 873 K in two dimensional (2D) nanoplates of Ge doped SnSe synthesized by a simple hydrothermal route followed by spark plasma sintering (SPS). Anisotropic measurements also show a high zT of ~1.8 at 873 K parallel to the SPS pressing direction. 3 mol% Ge-doping in SnSe nanoplates significantly enhances the p-type carrier concentration which results in high electrical conductivity and power factor of ~5.10 µW/cmK² at 873 K. In addition to nanoscale grain boundary and high lattice anharmonicity in SnSe nanoplates, phonon scattering due to Ge precipitates in the SnSe matrix gives rise to the ultralow lattice thermal conductivity of ~0.18 W/mK at 873 K.*

2.1 Introduction

Thermoelectric materials can convert waste heat to electricity, thus they should possess an important role in future energy management. Performance of a thermoelectric material is generally quantified by dimensionless *zT* defined as, $zT = \sigma S^2 T/\kappa$, where σ, *S*, κ and *T* are the electrical conductivity, Seebeck coefficient, thermal conductivity and temperature, respectively.[1] Two dimensional layered metal chalcogenides have recently gained momentous attention in the field of thermoelectrics owing to their anisotropic crystal structure and low thermal conductivity.[2] Among the 2D layered materials, the IV-VI semiconductors are contemplated as the most promising thermoelectric materials, for instance SnSe, which sparked a huge interest among the scientists due to its fascinating thermoelectric properties arising from its ultralow thermal conductivity, chemical stability, earth-abundance, and low toxicity.[3] At room temperature, SnSe adopts a layered orthorhombic crystal structure (space group *Pnma*) which is a resultant of three-dimensional distortion of the NaCl crystal structure. Sn and Se atoms are bonded covalently within the layer forming a zigzag double layer (2 atoms thick slab) along the *b-c* plane (Figure 2.1) and layers are separated by van der Waals interactions along the crystallographic *a*-direction. The structure contains distorted $SnSe_7$ polyhedra with four long and three short Sn-Se bonds. The $5s^2$ lone pair of Sn^{2+} is sterically accommodated in between the four long bonds thus culminating anisotropy and anharmonicity in the crystal structure. Single crystals of SnSe have lately shown an outstanding *zT* of ~2.6 at 923 K along crytallographic *b*-direction.[3a] Recently, an astonishing *zT* of 2.8 have been achieved in Br-doped *n*-type SnSe single crystals.

However, polycrystalline or nanocrystalline SnSe is a preferred choice for thermoelectric applications due to the ease of its production and processability.[4a] But polycrystalline samples

generally show lower carrier mobility as compared to that of the single crystals, thus effectively reduce the zT values.[4] Important reports are present which corroborate polycrystalline or nanocrystalline SnSe with various doping such alkali metal ions, Pb, Sb, Cu, Cl and I showing reasonably high zT.[5] However, in comparison with single crystals of SnSe, there are still scopes to improve the thermoelectric properties of polycrystalline SnSe by controlling the synthesis process and balancing the nanostructuring to optimize both the electronic and thermal transport properties.
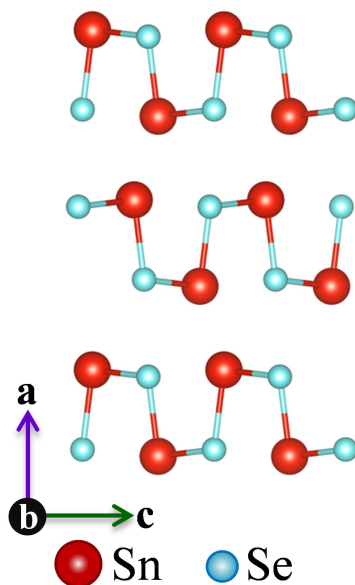
Figure 2.1 Structure of SnSe viewed down the crystallographic *b* direction.

Incidentally, GeSe adopts identical layered orthorhombic crystal structure as SnSe at ambient conditions and showed promises in thermoelectrics.[6] Thus, GeSe may form a solid solution with SnSe and can decrease the thermal conductivity. Moreover, Ge being more electronegative than Sn, can form an impurity dopant level just below the conduction band of Sn, thus can effectively decrease the band gap of SnSe which may also optimize the electronic transport properties. Although, there are few earlier reports on the Ge doping in polycrystalline SnSe synthesized by high temperature solid state melting, but the zT remains very low ~0.7 at

around 850 K.[7] Thus, we thought to explore the effect of Ge doping on the thermoelectric properties of 2D SnSe nanoplates synthesized by low temperature solution route.

In this chapter, I present high thermoelectric figure of merit (zT) of 2.1 at 873 K in Ge doped 2D SnSe nanoplates synthesized by a facile low temperature hydrothermal synthesis followed by spark plasma sintering (SPS). Ge doping increases the carrier concentration of the samples which leads to superior electrical conductivity and power factor in $Sn_{1-x}Ge_xSe$. Upon 3 mol% Ge doping in SnSe, the system deviates from solid solution and Ge starts precipitating in the SnSe matrix. $Sn_{0.97}Ge_{0.03}Se$ sample exhibits ultralow thermal conductivity of ~0.18 W/mK at 873 K due to synergistic phonon scattering by nano precipitates, nanoscale grains and inherent lattice anharmonicity. As SnSe possess an anisotropic structure, we have measured thermoelectric properties in both the parallel and perpendicular directions to the SPS pressing axis, which show a high zT of ~1.8 at 873 K parallel to the SPS pressing direction in $Sn_{0.97}Ge_{0.03}Se$.

2.2 Experimental Section

2.2.1 Reagents. Tin (II) chloride dihydrate ($SnCl_2.2H_2O$, 98%, Sigma Aldrich), selenium powder (Se, 99.99%, Alfa Aesar), germanium (IV) iodide (GeI_4, 99%, Sigma Aldrich) and sodium hydroxide pellets (NaOH, 98% Sigma Aldrich) were used for the synthesis.

2.2.2 Synthesis. $Sn_{1-x}Ge_xSe$ (x = 1-3 mol%) nanoplates were synthesized using simple hydrothermal route. First a mixture of $SnCl_2 \cdot 2H_2O$ (2 mmol) and GeI_4 (x mmol%) were dissolved in deionized water. The solution was then sonicated at room temperature for 10 min, followed by addition of NaOH (30 mmol) and sonication for another 10 min unless a clear solution was obtained. The mixture was then transferred to a Teflon-lined stainless steel

autoclave of 25 ml capacity and Se powder (1 mmol) was added to it that results in a black solution. The autoclaves were then sealed tightly and heated to 130 °C for 36 h. After cooling to room temperature, the black precipitate was collected and thoroughly washed with absolute ethanol and deionized water for several times. Finally the product was vacuum dried at 60 °C for 6 h and collected as powder. During the synthesis, NaOH acts as a solubilizing agent. Excess of Sn^{2+} should always be present in the reaction mixture (molar ratio of Sn^{2+} and Se must be higher than two) as Sn^{2+} itself acts as a reductant and precipitant.[8]

$$Sn^{2+} + Se \rightarrow Sn^{4+} + Se^{2-}$$

$$Sn^{2+} + Se^{2-} \rightarrow SnSe \downarrow$$
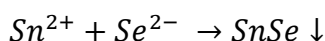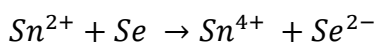
The yield of the reaction was ~ 95% and the product was scaled up to 10 gm for the thermoelectric measurements. The nanoplates were dispersed in ethanol for further characterizations.

2.2.3 Powder X-ray diffraction. Powder X-ray diffraction for all of the samples were recorded using a Cu K_α (λ = 1.5406 Å) radiation on a Bruker D8 Diffractometer.

2.2.4 Band gap measurements. To measure the optical band gap, a Perkin Elmer Lambda 900, UV/Vis/NIR spectrometer was used at the range of 200 nm to 3000 nm. Optical diffuse reflectance was measured for all the samples and using Kubelka-Munk equation, absorption (α/Λ) data were calculated. The above mention equation is as follows: $\alpha/\Lambda = (1 - R)^2/(2R)$, where *R* is the reflectance and α and Λ are the absorption and scattering coefficients, respectively. The energy band gap was derived from the tangent of α/Λ vs. *E* (eV) plot.

2.2.5 Field emission scanning electron microscopy (FESEM). FESEM imaging and EDAX were performed using NOVA NANO SEM 600 (FEI, Germany) operated at 15 KV.

2.2.6 Back-scattered electron microscopy (BSE). BSE imaging was performed during FESEM

using ZEISS Gemini SEM – Field Emission Scanning Electron Microscope operated at 500V.

2.2.7 Transmission electron microscopy (TEM). TEM experiments were performed using JEOL JEM3010 TEM fitted with a Gatan CCD camera operating at 300 KV accelerating voltage. A suspension of the nanosheets was prepared in cyclohexane solution and it was then drop casted in a holey carbon coated Cu grid for TEM imaging.

2.2.8 Scanning transmission electron microscopy (STEM). STEM imaging was carried out using FEITECNAI G^2 20 STWIN TEM operating at 200 KV. The sample preparation was same as that of TEM. EDAX compositional analysis and color mapping were performed during STEM imaging. Background was subtracted (using multi-polynomial model) during the data processing for EDAX color mapping (with 500 eV minimum region of interest width). Errors in the determination in compositions of nanosheets in EDAX measurements is nearly 5%.

2.2.9 Inductively coupled plasma atomic emission spectroscopy (ICP-AES). The exact composition of the as synthesized nanosheets was calculated based on ICP-AES data. ICP-AES measurements were carried out using Perkin-Elmer Optima 7000DV instrument. ICP-AES measurement were carried out by dissolving the powder nanosheets in aquaregia (HNO_3:HCl = 1:3) followed by diluting with millipore water. Sn standard (1000 mg/L, Sigma-Aldrich), Se standard (1000 mg/L, Sigma-Aldrich) and Bi standard (1000 mg/L, Sigma-Aldrich) were used to determine the compositions in ICP. In the present measurement, error bar lies below 1.5 %.

2.2.10 Spark plasma sintering (SPS). SPS was done using a SPS211-LX (Dr. Sinter Lab) instrument. The powdered nanoplates were sintered to prepare a rectangular column (8 mm × 8 mm × 8 mm) and coin (2 mm x 10 mm) using graphite dies at 50 MPa pressure and 450 ^{0}C temperature. From the rectangular column, a rectangular bar (2 mm × 2 mm × 8 mm) was made using a typical cutter-polisher. The density of the SPS processed samples were found to be about

~95 % of theoretical density.

2.2.11 Electrical transport properties. Electrical conductivity (σ) and Seebeck coefficients (S) were measured simultaneously from the rectangular bar under helium atmosphere from room temperature to 873 K using a ULVAC-RIKO ZEM-3 instrument system. σ and S were measured in both the parallel and perpendicular to the pressing directions.

2.2.12 Hall measurement. Room temperature carrier concentrations were determined from Hall coefficient measurements with the equipment developed by Excel Instrument, India. Four-contact Hall-bar geometry was used for the measurement. The applied magnetic field was 0.57 Tesla. Room temperature carrier concentration, *n*, was measured using the formula $n=1/eR_H$, where *e* is the electronic charge, R_H is hall coefficient.
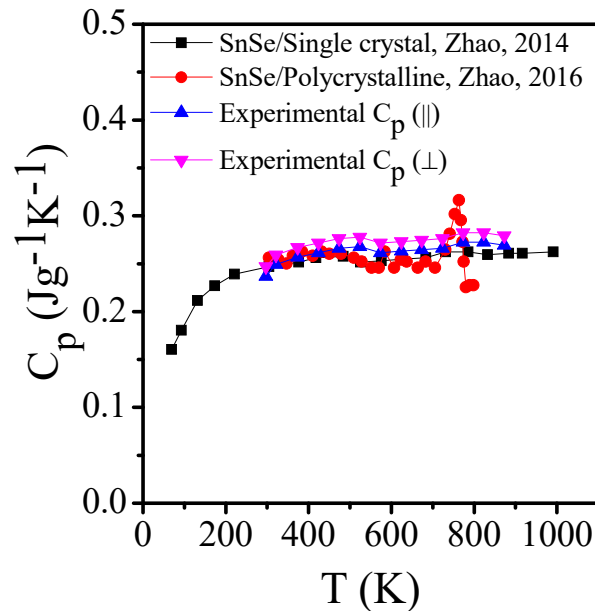

Figure 2.2 Temperature dependence of experimentally observed specific heat of present SnSe samples along the parallel and perpendicular direction of SPS. For comparison, C_p values of previously reported single crystals and polycrystals are given as reference.

2.2.13 Thermal transport. The thermal diffusivity (*D*) of the coin-shaped samples have been measured by laser flash diffusivity technique using NETZSCH LFA 457 instrument in 300−873 K range. Total thermal conductivity (κ) was calculated using the formula $\kappa = DC_p\rho$, where *D* is

the thermal diffusivity, C_p is specific heat, and ρ is density of the sample. Temperature dependent heat capacity, C_p (Figure 2.2) was derived using standard sample (pyroceram). Further, the electronic thermal conductivities, κ_{ele} were estimated using Wiedemann-Franz Law, $\kappa_{ele} = L\sigma T$, where L is the Lorenz number which is estimated by fitting reduced chemical potential derived from temperature-dependent Seebeck coefficient using single parabolic band conduction and dominant acoustic phonon scattering of carriers.

2.3 Results and Discussion

Powder X-ray diffraction (PXRD) was performed to identify the crystal structure of the as-synthesized samples of $Sn_{1-x}Ge_xSe$ (x = 0-3 mol%). The experimental patterns were indexed with the pure orthorhombic SnSe (*Pnma*, Figure 2.3) with lattice parameters of a = 11.50 Å, b = 4.15 Å and c = 4.45 Å.[3a, b]
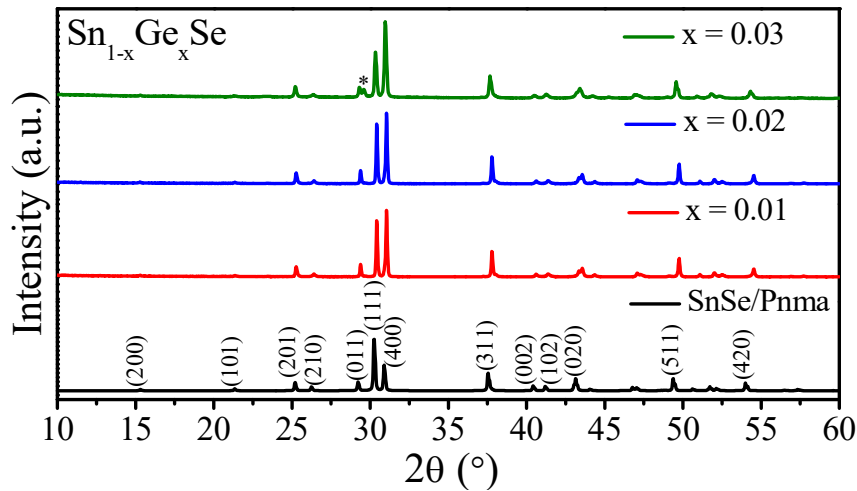
Figure 2.3 PXRD patterns of as-synthesized Ge doped SnSe nanoplates. The additional peak (denoted by *) that appears near the $(011)_{SnSe}$ peak indicates the trace of Ge precipitates in SnSe matrix.

However, an additional low intense peak appears in case of 3 mol% Ge doped SnSe near the $(011)_{SnSe}$ peak which can be attributed as Ge second phase (Figure 2.4). Thus, the solid solu

-tion limit exceeds after 2 mol% Ge doping in SnSe and traces of Ge starts precipitating out into the matrix. Furthermore, the peaks of $Sn_{1-x}Ge_xSe$ are slightly right shifted than that of the pristine sample which is in good agreement with the smaller atomic radius of Ge (211 pm) in comparison to Sn (225 pm). The optical band gap of SnSe (1.01 eV) decreases slightly after Ge incorporation (Figure 2.5). Ge being more electronegative than Sn creates an impurity acceptor level just below the conduction band of Sn, which in turn reduces the band gap of the $Sn_{1-x}Ge_xSe$ nanoplates.
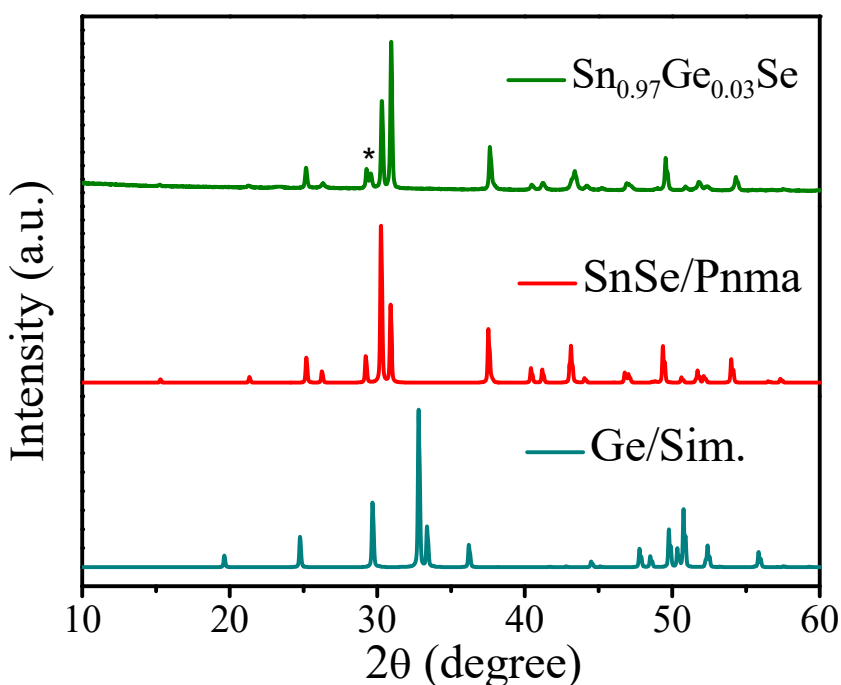
Figure 2.4 PXRD pattern of the as-synthesized $Sn_{0.97}Ge_{0.03}Se$ nanoplates indicating the presence of Ge precipitates in SnSe matrix.

To understand the morphology of the as-synthesized $Sn_{1-x}Ge_xSe$ samples, FESEM and transmission electron microscopy (TEM) were performed for the samples. The morphology of the $Sn_{0.97}Ge_{0.03}Se$ samples resembles to that of the 2D nanoplates which is evident from Figure 2.6 (a) and (c). The lateral dimension of the nanoplates ranges from 0.5 - 1.0 μm. The single crystalline nature of the nanoplate is verified by the HRTEM image (Figure 2.6 (b)). The lattice spacing between two apparent planes was estimated to be 3.07 Å which indicates that the (011)
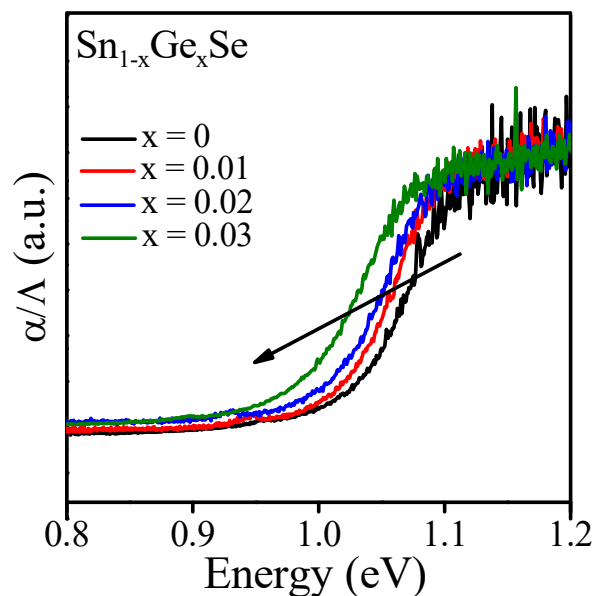
Figure 2.5 Electronic absorption spectra of $Sn_{1-x}Ge_xSe$ nanoplates.

set of planes are exposed in $Sn_{0.97}Ge_{0.03}Se$ nanoplates. In addition, selected area electron diffraction (SAED) of a single $Sn_{0.97}Ge_{0.03}Se$ nanoplate shows a spot pattern for (0kl) set of reflections (see inset of Figure 2.6 (a)) confirming the single crystalline nature.

The actual elemental compositions of $Sn_{1-x}Ge_xSe$ nanoplates were obtained from two independent experiments; inductively coupled plasma atomic emission spectroscopy (ICP-AES) and energy-dispersive analysis of X-rays (EDAX). Compositions determined by these two independent techniques are in good agreement with the nominal compositions (Table 2.1), which confirms successful control over the composition in the present synthetic technique. EDAX elemental colour mapping was performed during scanning transmission electron microscopy (STEM) imaging which shows the presence of Sn, Se and Ge in $Sn_{0.97}Ge_{0.03}Se$ nanoplates (Figure 2.6 (d)).

To understand the microstructure compositions in $Sn_{0.97}Ge_{0.03}Se$ SPS'ed samples, back-scattered electron imaging (BSE) was performed during FESEM (Figure 2.7 (a)), which shows the presence of the dark contrast Ge precipitates of $\sim$ 2–10 μm size embedded in lighter contrast
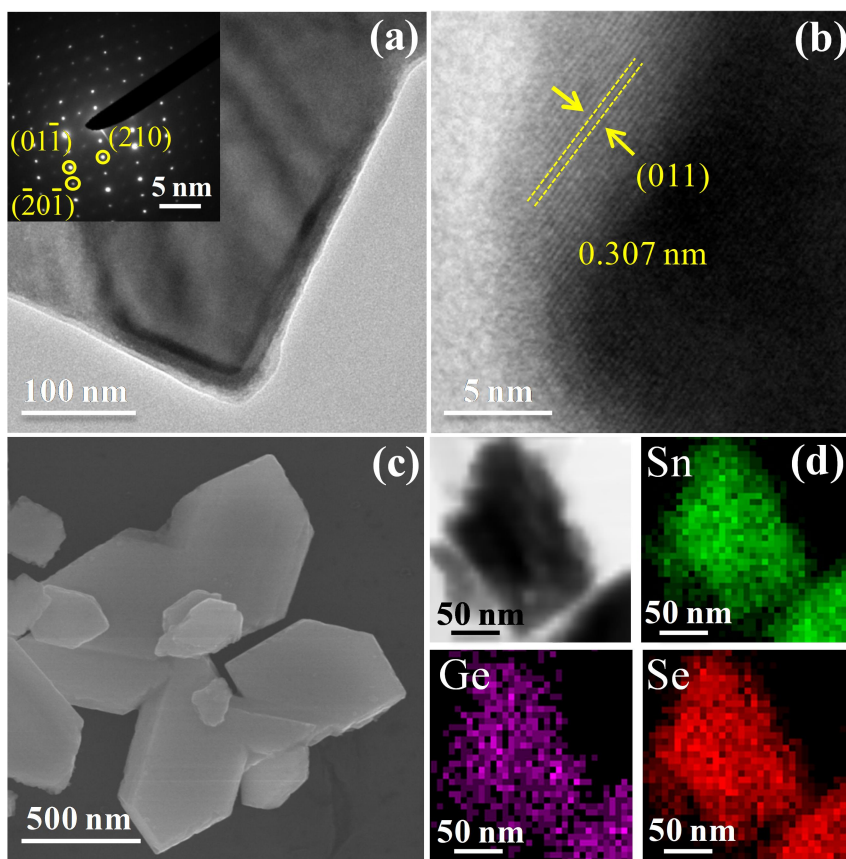
Figure 2.6 (a) TEM image of $Sn_{0.97}Ge_{0.03}Se$ nanoplates. SAED pattern of the same nanoplate is shown in the inset. (b) HRTEM and (c) FESEM image of $Sn_{0.97}Ge_{0.03}Se$ nanoplates. (d) STEM image of $Sn_{0.97}Ge_{0.03}Se$ nanoplates and EDAX color mapping for Sn, Se, and Ge.

SnSe matrix. To further confirm the phase composition, EDAX line scanning on a precipitate along with the matrix (highlighted by a white line in Figure 2.7 (a)) was performed, which clearly shows that the matrix is SnSe rich, whereas the precipitate is Ge rich (Figure 2.7 (b)).

Table 2.1 Analysis of sample compositions from ICP-AES and EDAX.

Nominal Composition	Composition obtained from ICP-AES	Composition obtained from EDAX
SnSe	$SnSe_{1.05}$	$SnSe_{1.1}$
$Sn_{0.99}Ge_{0.01}Se$	$Sn_{0.987}Ge_{0.014}Se_{1.03}$	-
$Sn_{0.98}Ge_{0.02}Se$	$Sn_{0.980}Ge_{0.026}Se$	-
$Sn_{0.97}Ge_{0.03}Se$	$Sn_{0.969}Ge_{0.036}Se_{1.1}$	$Sn_{0.959}Ge_{0.039}Se_{1.4}$
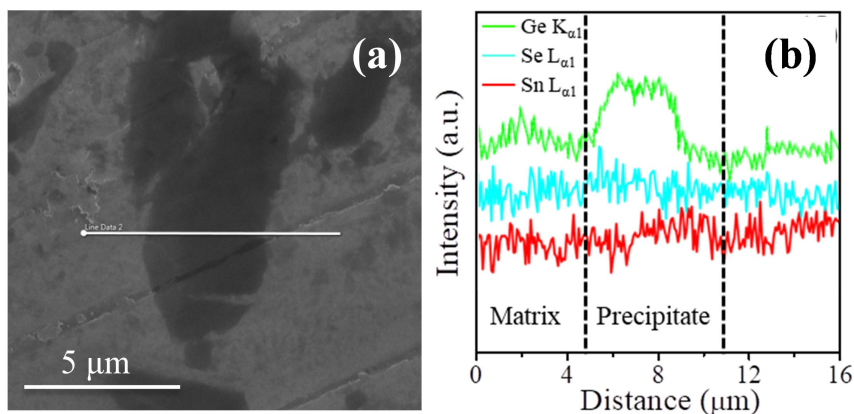
Figure 2.7 (a) Backscattered FESEM image from SPS processed $Sn_{0.97}Ge_{0.03}Se$, which shows the presence of precipitates of relatively dark contrast and large size. (b) EDAX line scan along the precipitate (highlighted in image a).

X-ray photoelectron spectroscopy (XPS) was performed on $Sn_{0.99}Ge_{0.01}Se$ which confirms the presence of Sn, Ge and Se in as-synthesized nanoplates (Figure 2.8). The Sn3d spin-orbit doublet peaks appeared at 489.1 eV and 499.3 eV with splitting of 10.2 eV, which can be assigned to $Sn3d_{5/2}$ and $Sn3d_{3/2}$, respectively. We could able to deconvolute the broad peak of selenium as $Se3d_{5/2}$ and $Se3d_{3/2}$ at 53.3 eV and 55.7 eV respectively. Presence of $Ge3d_{5/2}$ and $Ge2p_{3/2}$ peaks at 32.1 eV and 1219.5 eV can be attributed to Ge (II) states in $Sn_{0.99}Ge_{0.01}Se$.[7]

SnSe exhibits anisotropy in different crystallographic directions, thereby the thermoelectric measurements are done both in II (parallel) & ⊥ (perpendicular) to the pressing direction of SPS. A schematic illustration of the anisotropic measurement is given in Figure 2.9. Figure 2.10 – 2.15 presents the temperature dependent thermoelectric properties (both II & ⊥ direction) of the SPS'ed samples of $Sn_{1-x}Ge_xSe$ (x = 0-3 mol%) in the temperature range of 300 – 873 K. In each case, thermoelectric properties are higher in the perpendicular direction as compared to parallel direction to the SPS which is a typical behavior of SnSe.[4b, 5b] Figure 2.10 (a) and 2.10 (b) represents the variation of σ with temperature along the parallel and perpendicular to the pressing direction respectively. The dependence of electrical conductivity for all the samples
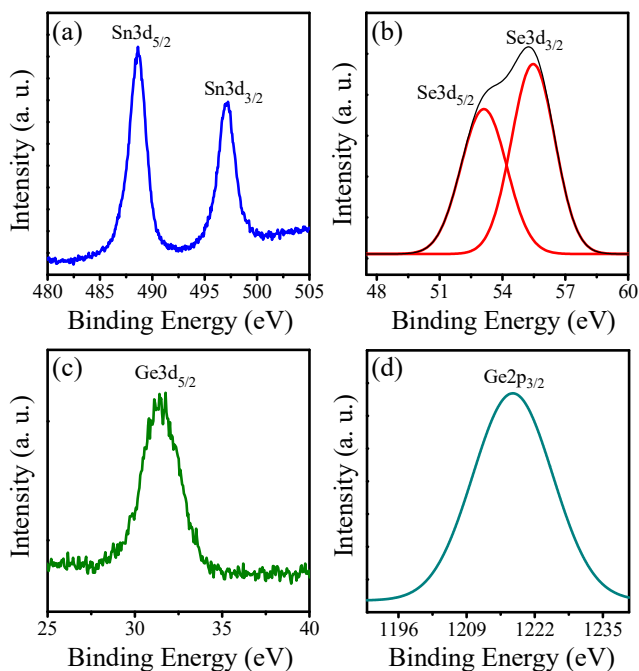
Figure 2.8. High-resolution XPS of (a) Sn 3d, (b) Se 3d, (c) Ge 3d and (d) 2p orbital in $Sn_{0.99}Ge_{0.01}Se$ nanoplates. The binding energy of the elements confirms that Sn, Se and Ge are in +2, -2 and +2 oxidation states respectively.

follows a similar trend which can be described as follows. First, semiconducting transport behavior occurs from 300 to 500 K due to the thermal excitation of minority carriers; then a metallic behavior is noticed up to 675 K; above this temperature σ increases linearly to 873 K which can be attributed to the structural phase transition from P*nma* to C*mcm* at around ~800K which has a similar trend to the previous SnSe samples.[4b, 5e]
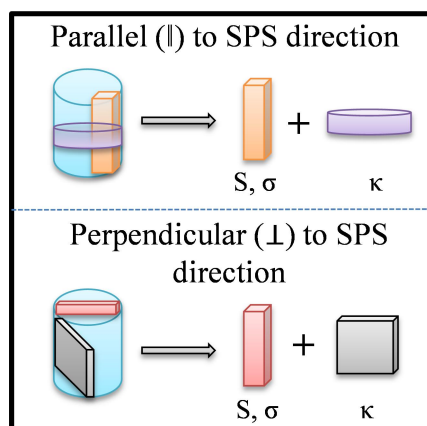
Figure 2.9 A schematic illustration to understand the anisotropic transport properties of SnSe.
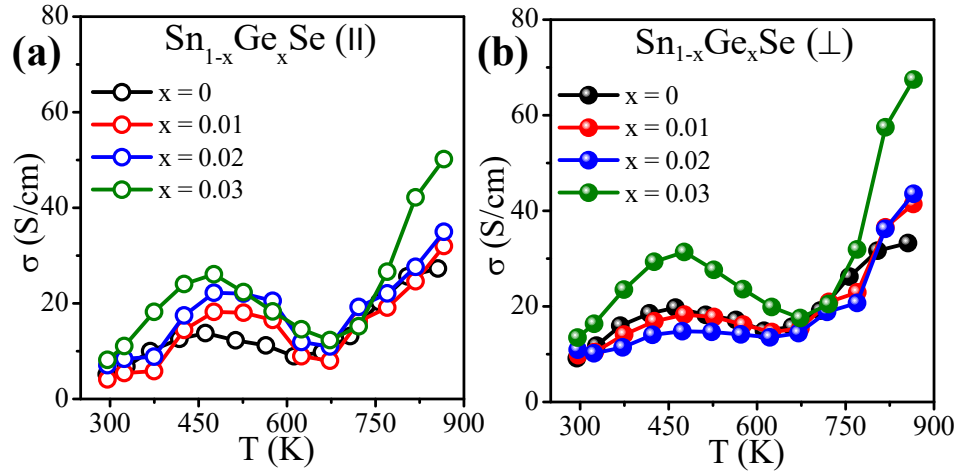
Figure 2.10 Temperature dependent electrical conductivity, σ, of $Sn_{1-x}Ge_xSe$ nanoplates measured (a) parallel (open symbols) and (b) perpendicular (solid symbols) to the SPS pressing direction respectively.

At room temperature, the σ values for the $Sn_{0.97}Ge_{0.03}Se$ (for the $\perp$ direction) was 13.8 Scm^{-1}, which increases to 67.9 Scm^{-1} with increase in temperature. Ge doping in SnSe increases the *p*-type carrier concentration (Table 2.2).

Table 2.2 Room temperature carrier concentrations of $Sn_{1-x}Ge_xSe$ samples.

Composition	Carrier Concentration (n) cm^{-3}
SnSe	3.9×10^{17}
$Sn_{0.99}Ge_{0.01}Se$	6.7×10^{18}
$Sn_{0.98}Ge_{0.02}Se$	9.0×10^{18}
$Sn_{0.97}Ge_{0.03}Se$	4.2×10^{19}

For 3 mol% Ge doped SnSe, carrier concentration (4.2×10^{19} cm^{-3}) is increased by two order of magnitude than the pristine sample ($3.9 \times 10^{17} cm^{-3}$). Thus the improved carrier concentration in $Sn_{0.97}Ge_{0.03}Se$ gives rise to superior electrical conductivity compared to that of pristine SnSe.

Figure 2.11 (a) and (b) shows the temperature dependence of Seebeck coefficient for all the $Sn_{1-x}Ge_xSe$ (x = 0-3 mol%) samples in the parallel and perpendicular directions respectively.
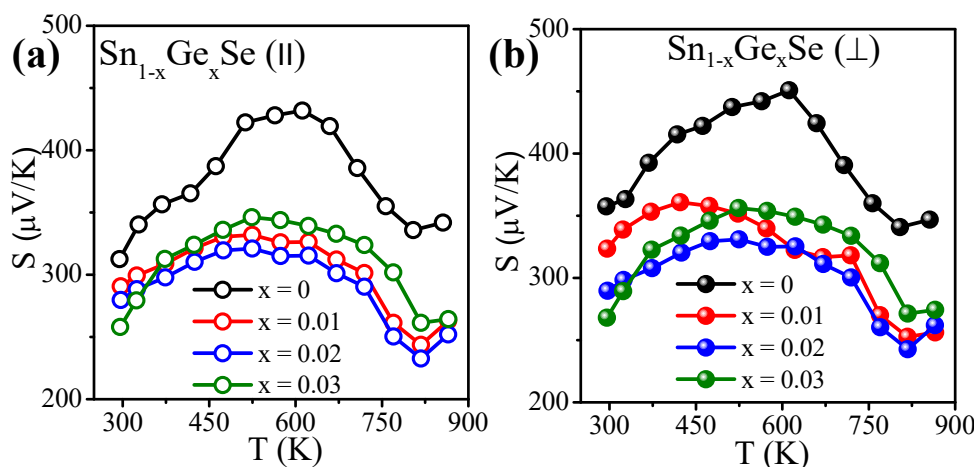
Figure 2.11. Temperature dependent Seebeck coefficient, *S,* of $Sn_{1-x}Ge_xSe$ nanoplates measured (a) parallel and (b) perpendicular to the SPS pressing direction respectively.

The $Sn_{1-x}Ge_xSe$ samples exhibit lower *S* values than the pristine sample. The reduction in *S* is consistent with the enhanced carrier concentrations as confirmed by Hall measurements (Table 2.2). Initially with increase in temperature, Seebeck coefficient increases and reaches to a maximum value in the temperature range of 550-650 K which is typical for solution processed SnSe samples.[4b, 5e] The peak in Seebeck coefficient indicates the bipolar conduction in the samples. [4b, 5e] The increase in Seebeck coefficient after 800 K indicates the structural phase transition. [4b, 5e]
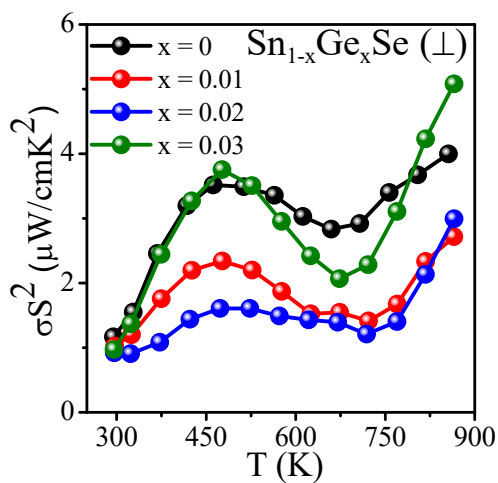
Figure 2.12 Temperature dependent power factor, σS^2 along perpendicular to the SPS direction.

The power factor of the $Sn_{1-x}Ge_xSe$ samples are given in Figure 2.12 (for the perpendicular to pressing direction). Remarkable high value of power factor (~5.10 $\mu W/cmK^2$) is obtained for 3 mol% Ge doped polycrystalline SnSe at 873 K.
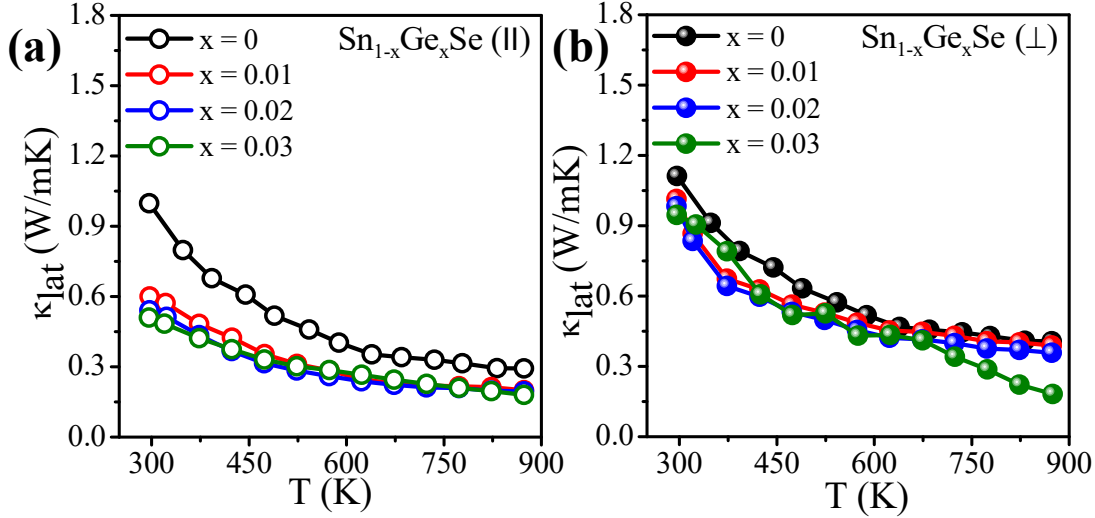
Figure 2.13 Temperature dependent lattice thermal conductivity, κ_{lat} of $Sn_{1-x}Ge_xSe$ nanoplates measured along (a) parallel and (b) perpendicular to the SPS direction respectively.

Figure 2.13 (a) and (b) show the temperature dependent κ_{lat} measured parallel and perpendicular to the SPS directions, respectively. The negligible difference between κ (Figure 2.14) and κ_{lat} clearly indicates that the thermal transport is mainly dominated by phonons.
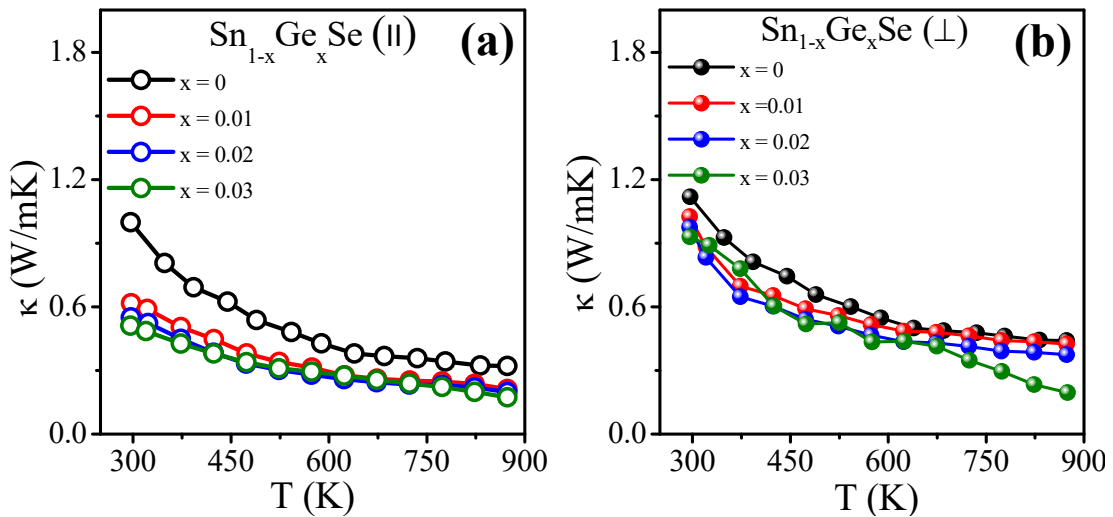
Figure 2.14 Temperature dependent total thermal conductivity, κ of $Sn_{1-x}Ge_xSe$ nanoplates measured along (a) parallel and (b) perpendicular to the SPS direction respectively.
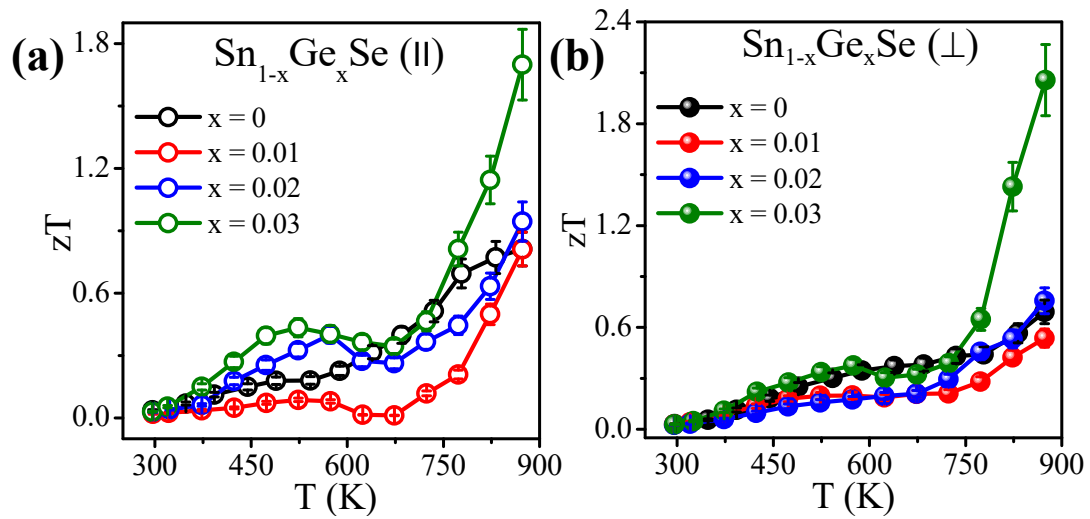
Figure 2.15 Temperature dependent *zT* of Sn$_{1-x}$Ge$_x$Se nanoplates measured along (a) parallel and (b) perpendicular to the SPS direction respectively.

In addition to the significant lattice anharmonicity in SnSe, the presence of solid solution point defects and Ge precipitates scatters the phonons in the Sn$_{0.97}$Ge$_{0.03}$Se samples, thereby effectively reduces the lattice thermal conductivity. For Sn$_{0.97}$Ge$_{0.03}$Se sample, κ_{lat} of ~0.18 W/mK is observed at 873 K for measurement perpendicular to the SPS direction.
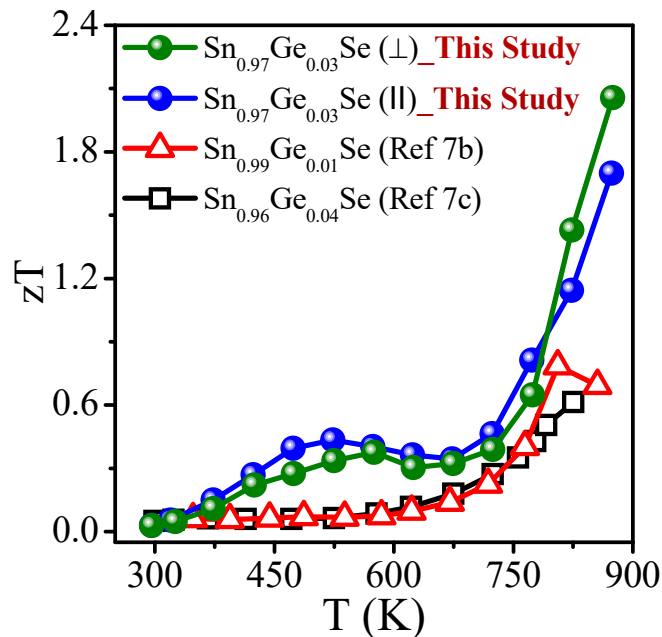
Figure 2.16 Comparison plot for *zT* of nanocrystalline Sn$_{1-x}$Ge$_x$Se with other Ge doped SnSe polycrystalline samples.

Hence, Ge doping in polycrystalline SnSe increases the electrical conductivity via tuning the *p*-type carrier concentration of the system, while the κ_{lat} decreases to a ultralow value due to effective phonon scattering at the point defects, nanoscale grains boundaries and precipitates. Consequently, *zT* increases to a maximum value of ~2.1 at 873 K for *p*-type solution processed nanocrystalline $Sn_{0.97}Ge_{0.03}Se$ ($\perp$ to the pressing direction, Figure 2.15 (b)), which is significantly higher than that of previously reported polycrystalline Ge doped SnSe made by solid state melting (Figure 2.16).[7] We have obtained a maximum *zT* value of ~1.8 at 873 K along the pressing direction in $Sn_{0.97}Ge_{0.03}Se$, Figure 2.15 (a). The obtained high *zT* value in $Sn_{0.97}Ge_{0.03}Se$ is reproducible in several batches of samples synthesized separately (Figure 2.17).
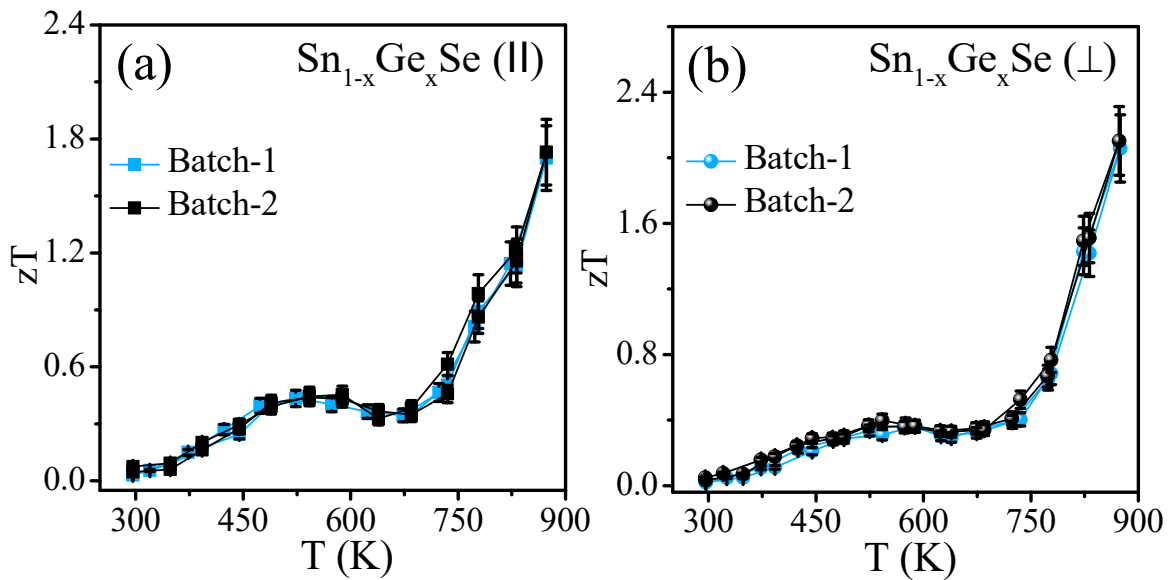
Figure 2.17 *zT* of SPS processed $Sn_{0.97}Ge_{0.03}Se$ sample is reversible (heating-cooling) and reproducible over temperature gradient and different batch of synthesis for both the (a) parallel and (b) perpendicular directions.

2.4 Conclusions

In summary, a cost-effective simple hydrothermal synthesis has been implemented to prepare 2D nanoplates of $Sn_{1-x}Ge_xSe$ (x = 0-3 mol%). Ge doping in SnSe increases the *p*-type carrier concentration, thereby enhances electrical transport. Synergistic effect of lattice

anharmonicity, nanoscale grains and precipitates decrease the κ_{lat} heavily in $Sn_{1-x}Ge_xSe$. Thus, an extremely high *zT* of ~1.8 and ~2.1 at 873 K are obtained for 3 mol % Ge doped SnSe when measured in parallel and perpendicular to the SPS pressing directions, respectively.

References

[1]   (a) Tan, G.; Zhao, L. D.; Kanatzidis, M. G., Rationally Designing High-Performance Bulk Thermoelectric Materials. *Chem. Rev.* **2016**, *116*, 12123-12149. (b) Ge, Z. H.; Zhao, L. D.; Wu, D.; Liu, X.; Zhang, B.-P.; Li, J.-F.; He, J., Low-cost, abundant binary sulfides as promising thermoelectric materials. *Mater. Today* **2016**, *19*, 227-239. (c) Zhao, L. D.; Dravid, V. P.; Kanatzidis, M. G., The panoscopic approach to high performance thermoelectrics. *Energy Environ. Sci.* **2014**, *7*, 251-268.

[2]   (a) Zhou, Y.; Zhao, L. D., Promising Thermoelectric Bulk Materials with 2D Structures. *Adv. Mater.* **2017**, *29*, 1702676. (b) Cao, X.; Tan, C.; Zhang, X.; Zhao, W.; Zhang, H., Solution-Processed Two-Dimensional Metal Dichalcogenide-Based Nanomaterials for Energy Storage and Conversion. *Adv. Mater.* **2016**, *28*, 6167-6196. (c) Samanta, M.; Pal, K.; Pal, P.; Waghmare, U. V.; Biswas, K., Localized Vibrations of Bi Bilayer Leading to Ultralow Lattice Thermal Conductivity and High Thermoelectric Performance in Weak Topological Insulator *n*-Type BiSe. *J. Am. Chem. Soc.* **2018**, *140*, 5866-5872. (d) Banik, A.; Biswas, K., Synthetic Nanosheets of Natural van der Waals Heterostructures. *Angew. Chem., Int. Ed.* **2017**, *56*, 14561-14566. (e) Chatterjee, A.; Biswas, K., Solution-Based Synthesis of Layered Intergrowth Compounds of the Homologous $Pb_mBi_{2n}Te_{3n+m}$ Series as Nanosheets. *Angew. Chem., Int. Ed.* **2015**, *54*, 5623-5627.

[3]   (a) Zhao, L. D.; Lo, S. H.; Zhang, Y.; Sun, H.; Tan, G.; Uher, C.; Wolverton, C.; Dravid, V. P.; Kanatzidis, M. G., Ultralow thermal conductivity and high thermoelectric figure of merit in SnSe crystals. *Nature* **2014**, *508*, 373-377. (b) Peng, K.; Lu, X.; Zhan, H.; Hui, S.; Tang, X.; Wang, G.; Dai, J.; Uher, C.; Wang, G.; Zhou, X., Broad temperature plateau for high ZTs in heavily doped *p*-type SnSe single crystals. *Energy Environ. Sci.* **2015**, *9*, 454-

460. (c) Zhao, L. D.; Tan, G.; Hao, S.; He, J.; Pei, Y.; Chi, H.; Wang, H.; Gong, S.; Xu, H.; Dravid, V. P.; Uher, C.; Snyder, G. J.; Wolverton, C.; Kanatzidis, M. G., Ultrahigh power factor and thermoelectric performance in hole-doped single-crystal SnSe. *Science* **2016**, *351*, 141-144. (d) Zhao, L. D.; Chang, C.; Tan, G.; Kanatzidis, M. G., SnSe: a remarkable new thermoelectric material. *Energy Environ. Sci.* **2016**, *9*, 3044-3060. (e) Duong, A. T.; Nguyen, V. Q.; Duvjir, G.; Duong, V. T.; Kwon, S.; Song, J. Y.; Lee, J. K.; Lee, J. E.; Park, S.; Min, T.; Lee, J.; Kim, J.; Cho, S., Achieving ZT=2.2 with Bi-doped *n*-type SnSe single crystals. *Nat. Commun.* **2016**, *7*, 13713. (f) Chang, C.; Wu, M.; He, D.; Pei, Y.; Wu, C.-F.; Wu, X.; Yu, H.; Zhu, F.; Wang, K.; Chen, Y.; Huang, L.; Li, J.-F.; He, J.; Zhao, L.-D., 3D charge and 2D phonon transports leading to high out-of-plane ZT in *n*-type SnSe crystals. *Science* **2018**, *360*, 778-783.

[4]   (a) Chen, Y. X.; Ge, Z. H.; Yin, M.; Feng, D.; Huang, X. Q.; Zhao, W.; He, J., Understanding of the Extremely Low Thermal Conductivity in High-Performance Polycrystalline SnSe through Potassium Doping. *Adv. Funct. Mater.* **2016**, *26*, 6836-6845. (b) Tang, G.; Wei, W.; Zhang, J.; Li, Y.; Wang, X.; Xu, G.; Chang, C.; Wang, Z.; Du, Y.; Zhao, L. D., Realizing High Figure of Merit in Phase-Separated Polycrystalline Sn$_{1-x}$Pb$_x$Se. *J. Am. Chem. Soc.* **2016**, *138*, 13647-13654. (c) Ge, Z. H.; Song, D.; Chong, X.; Zheng, F.; Jin, L.; Qian, X.; Zheng, L.; Dunin-Borkowski, R. E.; Qin, P.; Feng, J.; Zhao, L. D., Boosting the Thermoelectric Performance of (Na,K)-Codoped Polycrystalline SnSe by Synergistic Tailoring of the Band Structure and Atomic-Scale Defect Phonon Scattering. *J. Am. Chem. Soc.* **2017**, *139*, 9714-9720. (d) Shi, X.-L.; Zheng, K.; Liu, W.-D.; Wang, Y.; Yang, Y.-Z.; Chen, Z.-G.; Zou, J., Realizing High Thermoelectric Performance in *n*-Type

Highly Distorted Sb-Doped SnSe Microplates via Tuning High Electron Concentration and Inducing Intensive Crystal Defects. *Adv. Energy Mater.* **2018**, *8*, 1800775.

[5]   (a) Lee, Y. K.; Ahn, K.; Cha, J.; Zhou, C.; Kim, H. S.; Choi, G.; Chae, S. I.; Park, J. H.; Cho, S. P.; Park, S. H.; Sung, Y. E.; Lee, W. B.; Hyeon, T.; Chung, I., Enhancing *p*-Type Thermoelectric Performances of Polycrystalline SnSe via Tuning Phase Transition Temperature. *J. Am. Chem. Soc.* **2017**, *139*, 10887-10896. (b) Zhang, Q.; Chere, E. K.; Sun, J.; Cao, F.; Dahal, K.; Chen, S.; Chen, G.; Ren, Z. C., Studies on Thermoelectric Properties of *n*-type Polycrystalline $SnSe_{1-x}S_x$ by Iodine Doping. *Adv. Energy Mater.* **2015**, *5*, 1500360. (c) Wei, T. R.; Tan, G.; Zhang, X.; Wu, C. F.; Li, J. F.; Dravid, V. P.; Snyder, G. J.; Kanatzidis, M. G., Distinct Impact of Alkali-Ion Doping on Electrical Transport Properties of Thermoelectric *p*-Type Polycrystalline SnSe. *J. Am. Chem. Soc.* **2016**, *138*, 8875-8882. (d) Han, G.; Popuri, S. R.; Greer, H. F.; Llin, L. F.; Bos, J.-W. G.; Zhou, W.; Paul, D. J.; Ménard, H.; Knox, A. R.; Montecucco, A.; Siviter, J.; Man, E. A.; Li, W.-g.; Paul, M. C.; Gao, M.; Sweet, T.; Freer, R.; Azough, F.; Baig, H.; Mallick, T. K.; Gregory, D. H., Chlorine-Enabled Electron Doping in Solution-Synthesized SnSe Thermoelectric Nanomaterials. *Adv. Energy Mater.* **2017**, *7*, 1602328. (e) Wei, W.; Chang, C.; Yang, T.; Liu, J.; Tang, H.; Zhang, J.; Li, Y.; Xu, F.; Zhang, Z.; Li, J.-F.; Tang, G., Achieving High Thermoelectric Figure of Merit in Polycrystalline SnSe via Introducing Sn Vacancies. *J. Am. Chem. Soc.* **2018**, *140*, 499-505. (f) Luo, Y.; Zheng, Y.; Luo, Z.; Hao, S.; Du, C.; Liang, Q.; Li, Z.; Khor, K. A.; Hippalgaonkar, K.; Xu, J.; Yan, Q.; Wolverton, C.; Kanatzidis, M. G., *n*-Type $SnSe_2$ Oriented-Nanoplate-Based Pellets for High Thermoelectric Performance. *Adv. Energy Mater.* **2017**, 1702167. (g) Shi, X.; Zheng, K.; Hong, M.; Liu, W.; Moshwan, R.; Wang, Y.; Qu, X.; Chen, Z.-G.; Zou, J., Boosting the

thermoelectric performance of *p*-type heavily Cu-doped polycrystalline SnSe via inducing intensive crystal imperfections and defect phonon scattering. *Chem. Sci.* **2018**, *9*, 7376-7389.

[6]   (a) Roychowdhury, S.; Ghosh, T.; Arora, R.; Waghmare, U. V.; Biswas, K., Stabilizing n-Type Cubic GeSe by Entropy-Driven Alloying of AgBiSe$_2$: Ultralow Thermal Conductivity and Promising Thermoelectric Performance. *Angew. Chem. Int. Ed.* **2018**, *130*, 15387-15391. (b) Huang, Z.; Miller, S. A.; Ge, B.; Yan, M.; Anand, S.; Wu, T.; Nan, P.; Zhu, Y.; Zhuang, W.; Snyder, G. J.; Jiang, P.; Bao, X., High Thermoelectric Performance of New Rhombohedral Phase of GeSe stabilized through Alloying with AgSbSe$_2$. *Angew. Chem. Int. Ed.* **2017**, *56*, 14113-14118. (c) Roychowdhury, S.; Samanta, M.; Perumal, S.; Biswas, K., Germanium Chalcogenide Thermoelectrics: Electronic Structure Modulation and Low Lattice Thermal Conductivity. *Chem. Mater.* **2018**, *30*, 5799-5813.

[7]   (a) Gharsallah, M.; Serrano-Sánchez, F.; Nemes, N. M.; Mompeán, F. J.; Martínez, J. L.; Fernández-Díaz, M. T.; Elhalouani, F.; Alonso, J. A., Giant Seebeck effect in Ge-doped SnSe. *Sci. Rep.* **2016**, *6*, 26774. (b) Wubieneh, T. A.; Chen, C.-L.; Wei, P. C.; Chen, S.-Y.; Chen, Y.-Y., The effects of Ge doping on the thermoelectric performance of *p*-type polycrystalline SnSe. *RSC Adv.* **2016**, *6*, 114825-114829. (c) Fu, Y.; Xu, J.; Liu, G.-Q.; Tan, X.; Liu, Z.; Wang, X.; Shao, H.; Jiang, H.; Liang, B.; Jiang, J., Study on Thermoelectric Properties of Polycrystalline SnSe by Ge Doping. *J. Electron. Mater.* **2017**, *46*, 3182-3186.

[8]   (a) Li, Y.; Li, F.; Dong, J.; Ge, Z.; Kang, F.; He, J.; Du, H.; Li, B.; Li, J.-F., Enhanced mid-temperature thermoelectric performance of textured SnSe polycrystals made of solvothermally synthesized powders. *J. Mater. Chem. C* **2016**, *4*, 2047-2055. (b) Ge, Z.-H.;

Wei, K.; Lewis, H.; Martin, J.; Nolas, G. S., Bottom-up processing and low temperature transport properties of polycrystalline SnSe. *J. Solid State Chem.* **2015**, *225*, 354-358.

Chapter 3

n-Type Ultrathin Few-layer Nanosheets of Bi Doped SnSe: Synthesis and Thermoelectric Properties*

n-Type Ultrathin Few-layer Nanosheets of Bi Doped SnSe: Synthesis and Thermoelectric Properties

Summary: *SnSe, an environmental friendly layered chalcogenide fostered immense attention in the thermoelectric community with their high thermoelectric figure of merit in single crystals. Although the stride towards developing superior p-type SnSe as a thermoelectric material is progressing rapidly, synthesis of n-type SnSe is somewhat overlooked. Here, we report the solution phase synthesis and thermoelectric transport properties of two dimensional (2D) ultrathin (1.2-3 nm thick) few layer nanosheets (2-4 layers) of n-type SnSe. The n-type nature of the nanosheets initially originates from chlorination of the material during the synthesis. We could able to increase the carrier concentration of n-type SnSe significantly from 3.08×10^{17} cm^{-3} to 1.97×10^{18} cm^{-3} via further Bi doping which results in the increment of electrical conductivity and power factor. Furthermore, Bi-doped nanosheets exhibit ultralow lattice thermal conductivity (~0.3 W/mK) throughout the temperature range of 300-720 K which can be ascribed to the effective phonon scattering by interface of SnSe layers, nanoscale grain boundaries and point defects.*

3.1 Introduction

In most of the cases, reported SnSe materials are *p*-type while thermoelectric applications demand for both *p*-type and *n*-type materials. Recently, *n*-type single crystals of 6 mole% Bi-doped SnSe have been reported to show high *zT* of 2.2.[1] Till date, few nanostructures (eg. nanowires, nanoplates, nanoflowers and nanosheets) of SnSe have been synthesized by bottom-up wet chemical synthesis,[2, 3] but the materials are mostly *p*-type.[4, 5] Recently, electronic transport properties of *n*-type Cl-doped SnSe nanoparticles have been studied, which show moderate power factors.[4] Thus, *n*-type SnSe with 2D few-layered nanosheet morphology would be interesting for thermoelectric investigations as it may exhibits low thermal conductivity (κ_L) due to excess phonon scattering from nanoscale grains and interfaces.

In this chapter, I have demonstrated the low temperature solution phase synthesis and anisotropic thermoelectric properties of *n*-type few-layer (~2-4 layers) Bi-doped SnSe nanosheets (1.2-3 nm thick). Nanosheets of $Sn_{0.94}Bi_{0.06}Se$ exhibit lower band gap compared to the pristine SnSe nanosheets due to the formation of Bi acceptor level near the conduction band. Bi-doped few-layer SnSe nanosheets show enhanced *n*-type carrier concentration compared to SnSe nanosheets, which resulted in superior electrical conductivity and power factor for spark plasma sintering (SPS) processed $Sn_{0.94}Bi_{0.06}Se$ nanosheets compared to SnSe nanosheets. We have achieved higher Seebeck coefficient value in the perpendicular to the SPS pressing direction (i.e. along c-axis in SnSe) compared to parallel to SPS pressing direction (i.e. along a-axis in SnSe) due to high effective mass of the conduction band electron along the crystallographic c-axis. Furthermore, $Sn_{0.94}Bi_{0.06}Se$ nanosheets exhibit ultralow lattice thermal conductivity ($\sim 0.3 Wm^{-1}K^{-1}$) in the temperature range of 300-720 K due to effective phonon scattering by interface of SnSe layers and point defects. We have achieved a *zT* of 0.21 at 719 K

in $Sn_{0.94}Bi_{0.06}Se$ nanosheets, which is higher than that of the controlled *n*-type SnSe nanosheet sample.

3.2 Experimental Section

3.2.1 Reagents. Tin (IV) chloride pentahydrate ($SnCl_4.5H_2O$, 98%, Sigma Aldrich), Selenium dioxide (SeO_2, 99.9%, Sigma Aldrich), Oleylamine (OAm, tech. 90%, Sigma Aldrich), Bismuth neodecanoate ($Bi(OCOC(CH_3)_2(CH_2)_5CH_3)_3$, Sigma Aldrich) and 1,10-phenanthroline (Phen, $C_{12}H_8N_2$, 90%, Alfa Aesar) were used for synthesis.

3.2.2 Synthesis. In order to prepare pure phase *n*-type SnSe nanosheets, a typical Schlenk line method with vacuum and N_2 atmosphere has been used. First a mixture of $SnCl_4 \cdot 5H_2O$ (0.1 mmol), SeO_2 (0.1mmol), oleylamine (OAM, 10mL) and 1,10-phenanthroline (Phen, 0.1 mmol) were added into a three-necked flask at room temperature. The mixture was continuously stirred for 10 minutes under vacuum. The pale-yellow color of the resulting solution indicates the formation of $SnCl_4$-oleylamine complex (Figure 3.1). The solution mixture was degassed in N_2 atmosphere for 10 min at 120 °C and heated up to 200 °C. The color of the solution changes from pale yellow to orange and then a black colored suspension was formed immediately at 200 °C. Black colored suspension was further stirred for 5 min to complete the reaction. The reaction mixture was slowly cooled down to room temperature under inert atmosphere with constant stirring. Next the black precipitate was purified by washing several times with ethanol and hexane in an alternative fashion via centrifugation (at a rate of 4000 rpm). Finally the product was vacuum dried and collected as powder. In the preparation method, OAM acts as both capping reagent as well as reducing agent and Phen acts as a morphology controlling agent. To prepare $Sn_{0.94}Bi_{0.06}Se$, Bi-neodecanoate was added in stoichiometric amount along with the other

reagents and the rest of the procedure remains the same.

The yield of the reaction was ~95% and the products are scaled up to ~7 gm for the thermoelectric measurements. The nanosheets are dispersed in cyclohexane for further characterizations.

Removal of capping ligands. To measure thermoelectric properties, capping reagent has been removed by heat-treatment. The vacuum dried power samples were taken in an alumina boat and kept inside a tube furnace. Next the tube furnace was heated to 500 °C over 5 hrs and soaked for another 4 hrs under N_2 atmosphere and then slowly cooled down to room temperature. During the annealing process, red colored Se vapors were liberated and oleylamine got detached from the nanosheets.
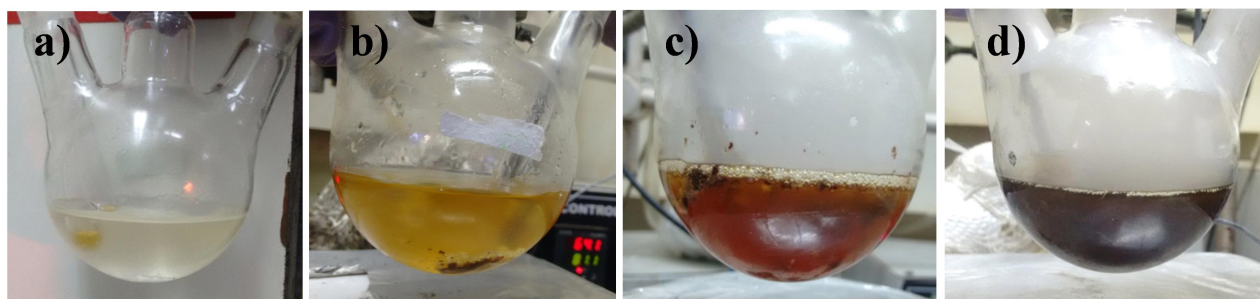
Figure 3.1 Color change at different stages of the reaction. (a) Pale-white solution of $SnCl_4$, SeO_2, Phen in OAm. (b) The color of the solution became yellow at 120 ^{0}C due to formation of $SnCl_4$-OAm adduct. (c) At 180 ^{0}C the solution became dark orange. (d) Formation of black colloidal solution of SnSe nanosheets.

3.2.3 Powder X-ray diffraction. Powder X-ray diffraction for all of the samples were recorded using a Cu K_α (λ = 1.5406 Å) radiation on a Bruker D8 diffractometer.

3.2.4 Band gap measurements. To measure optical band gap, a Perkin Elmer Lambda 900, UV/Vis/NIR spectrometer was used at the range of 200 nm to 3000 nm. Optical diffuse reflectance was measured for all the samples and using Kubelka-Munk equation, absorption (α/Λ) data were calculated. The above mention equation is as follows: $\alpha/\Lambda = (1 - R)^2/(2R)$, where R is the reflectance and α and Λ are the absorption and scattering coefficients, respectively. The

energy band gap was derived from the tangent of α/Λ vs. E (eV) plot.

3.2.5 X-ray photoelectron spectroscopy. XPS measurement has been performed with Mg−Kα (1253.6 eV) X-ray source with a relative composition detection better than 0.1% on an Omicron Nano-technology spectrometer.

3.2.6 Field emission scanning electron microscopy. FESEM images were derived using NOVA NANO SEM 600 (FEI, Germany) operated at 15 KV.

3.2.7 Transmission electron microscopy. TEM experiments were performed using JEOL JEM3010 TEM fitted with a Gatan CCD camera operating at 300 KV accelerating voltage. A suspension of the nanosheets was prepared in cyclohexane solution and it was then drop casted in a holey carbon coated Cu grid for TEM imaging.

3.2.8 Scanning transmission electron microscopy. STEM imaging was carried out using FEITECNAI G^2 20 STWIN TEM operating at 200 KV. The sample preparation was same as that of TEM. EDAX compositional analysis and color mapping were performed during STEM imaging. Background was subtracted (using multi-polynomial model) during the data processing for EDAX color mapping (with 500 eV minimum region of interest width). Errors in the determination in compositions of nanosheets in EDAX measurements is nearly 5%.

3.2.9 Inductively coupled plasma atomic emission spectroscopy (ICP-AES). The exact composition of the as synthesized nanosheets was calculated based on ICP-AES data. ICP-AES measurements were carried out using Perkin-Elmer Optima 7000DV instrument. ICP-AES measurement were carried out by dissolving the powder nanosheets in aquaregia (HNO_3:HCl = 1:3) followed by diluting with millipore water. Sn standard (1000 mg/L, Sigma-Aldrich), Se standard (1000 mg/L, Sigma-Aldrich) and Bi standard (1000 mg/L, Sigma-Aldrich) were used to determine the compositions in ICP. In the present measurement, error bar lies below 1.5 %.

3.2.10 Fourier transform infrared spectroscopy. FTIR spectra was recorded using a Bruker IFS 66v/S spectrometer.

3.2.11 Spark plasma sintering. Sintering was done using a SPS211-LX (Dr. Sinter Lab) instrument. The heat treated powdered nanosheets were sintered to prepare a rectangular column (8 mm × 8 mm ×8 mm) and coin (2 mm x 10 mm) using graphite dies at 40 MPa pressure and 450 ^{0}C temperature. From the rectangular column, a rectangular bar (2 mm × 2 mm × 8 mm) was made using a typical cutter-polisher. The density of the SPS processed samples were found to be about ~95 % of theoretical density.

3.2.12 Electrical transport. Electrical conductivity (σ) and Seebeck coefficients (S) were measured simultaneously from the rectangular bar under helium atmosphere from room temperature to 720 K using a ULVAC-RIKO ZEM-3 instrument system. σ and S were measured in both the parallel and perpendicular to the pressing directions.

3.2.13 Hall measurement. Room temperature carrier concentrations were determined from Hall coefficient measurements with the equipment developed by Excel Instrument, India. Four-contact Hall-bar geometry was used for the measurement. The applied magnetic field was 0.57 Tesla. Room temperature carrier concentration, *n*, was measured using the formula $n=1/eR_H$, where *e* is the electronic charge, R_H is hall coefficient.

3.2.14 Thermal transport. The thermal diffusivity (*D*) of the coin-shaped samples have been measured by laser flash diffusivity technique using NETZSCH LFA 457 instrument in 300−720 K range. Total thermal conductivity (κ_{total}) was calculated using the formula $\kappa_{total} = DC_p\rho$, where *D* is the thermal diffusivity, C_p is specific heat, and ρ is density of the sample. Further, the electronic thermal conductivities, κ_{ele} were estimated using Wiedemann-Franz Law, $\kappa_{ele} = L\sigma T$, where *L* is the Lorenz number which is estimated by fitting reduced chemical potential derived

from temperature-dependent Seebeck coefficient using single parabolic band conduction and dominant acoustic phonon scattering of carriers. The heat capacity value was taken from reference 6 and 7.

3.3 Results and Discussion

SnSe adopts a layered orthorhombic crystal structure (*P*nma) at room temperature, in which the intralayer Sn and Se atoms are covalently bonded in the *a-b* plane and the layers are held together by interlayer van der Waals interactions along the c-axis (Figure 3.2).
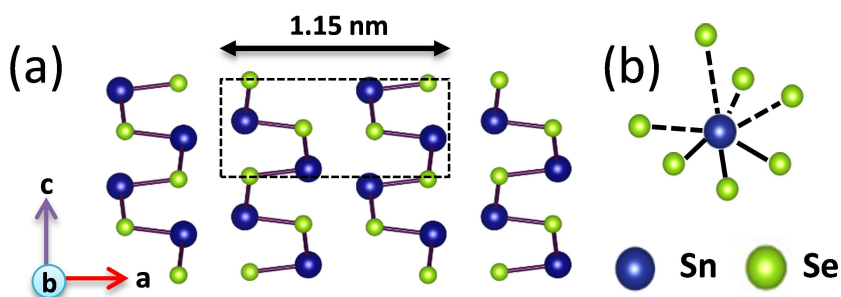
Figure 3.2 (a) Crystal structure of SnSe along the crystallographic b-direction. (b) Highly distorted SnSe$_7$ polyhedra containing four long (dotted lines) and three short (solid lines) Sn-Se bonds.

Powder X-ray diffraction (PXRD) patterns of as-synthesized samples have been indexed to pure orthorhombic SnSe (Figure 3.3 (a)) with lattice parameters of a = 11.50 Å, b = 4.15 Å and c = 4.45 Å. The indirect optical band gap of the SnSe nanosheets were measured to be ~0.88 eV. Further, Bi being more electronegative than Sn, is known to create an acceptor level just below the conduction band of Sn, which *in-turn* reduces the band gap of the Sn$_{0.94}$Bi$_{0.06}$Se nanosheets to ~0.75 eV (Figure 3.3 (b)).

In order to confirm Bi doping, X-ray photoelectron spectroscopy (XPS) was performed on both SnSe and Bi-doped SnSe nanosheets. Figure 3.4 confirms the presence of Sn, Se and Bi in as-synthesized Sn$_{0.94}$Bi$_{0.06}$Se nanosheets. The Sn3d spin-orbit doublet peaks appeared at 488.4
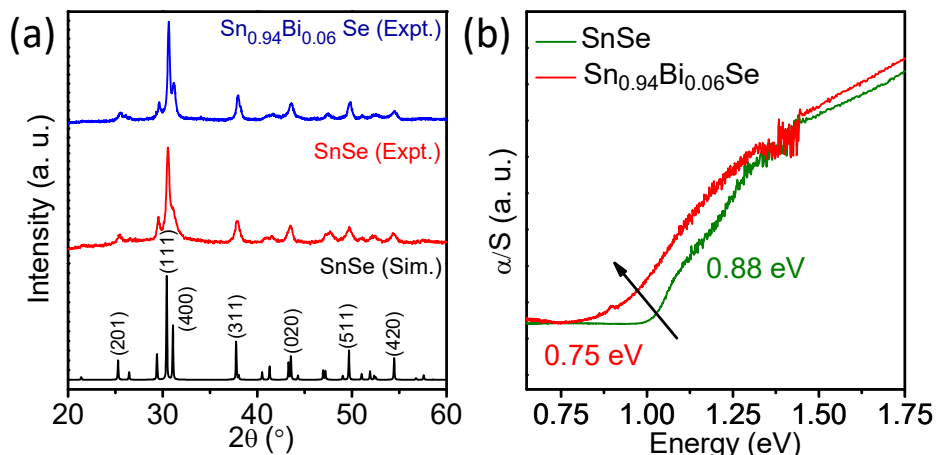
Figure 3.3 (a) PXRD patterns of as-synthesized SnSe and $Sn_{0.94}Bi_{0.06}Se$ nanosheets. (b) Optical absorption spectra of SnSe and $Sn_{0.94}Bi_{0.06}Se$ nanosheets.

eV and 496.7 eV with splitting of 8.3 eV, which can be assigned to $Sn3d_{5/2}$ and $Sn3d_{3/2}$, respectively.[8] We could able to deconvolute the broad peak of selenium as $Se3d_{5/2}$ and $Se3d_{3/2}$ at 53.1 eV and 55.45 eV respectively.[9]
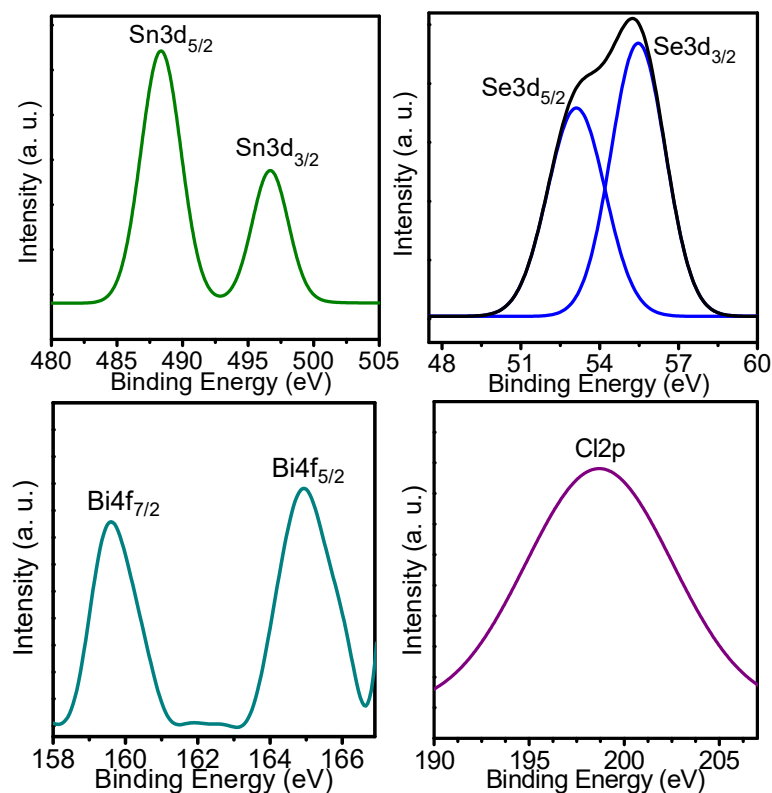
**Figure 3.4** High-resolution XPS of Sn3d, Se3d, Bi4f and Cl2p in $Sn_{0.94}Bi_{0.06}Se$ nanosheets.

Presence of Bi4f$_{7/2}$ and Bi4f$_{5/2}$ peaks at 159.6 eV and 164.95 eV can be attributed to Bi (III) states in Bi-doped SnSe sample.[8] *In situ* chlorination of as-synthesized SnSe and Sn$_{0.94}$Bi$_{0.06}$Se nanosheets was further confirmed from the XPS peak at 198.7 eV.[9]

Table 3.1 Compositional analysis from EDAX and ICP.

Nominal Composition	EDAX Composition	ICP-AES Composition
SnSe	SnSe$_{1.05}$	SnSe$_{1.33}$
Sn$_{0.94}$Bi$_{0.06}$Se	Sn$_{0.91}$Bi$_{0.058}$Se$_{1.47}$	Sn$_{0.94}$Bi$_{0.055}$Se$_{1.42}$

The actual elemental compositions of SnSe nanosheet samples were obtained further from inductively coupled plasma atomic emission spectroscopy (ICP-AES) and energy dispersive analysis of X-Rays (EDAX). Compositions determined by these two independent techniques are in good agreement with the nominal compositions (Table 3.1), which confirms successful control over the composition in the present synthetic technique.

Field emission scanning electron microscopy (FESEM) images display the 2D nanosheet morphology of SnSe and Sn$_{0.94}$Bi$_{0.06}$Se samples (Figures 3.5 (a) and 3.6 (a)). SnSe and Bi-doped SnSe samples show folded nanosheet like morphology with the thickness of few nanometers (1.2-3nm). The ultra-thin nature of the nanosheets was confirmed by AFM, as depicted in Figures 3.5 (b) and 3.6 (b). The height profile acquired from a typical AFM micrograph indicates the formation of 1.18 nm thick nanosheets (Figure 3.5 (b)), which is nearly the thickness of two-layers SnSe (i.e. a axis of the unit cell). The lateral dimension of the as-synthesized nanosheets ranges from 0.3 to 0.5 µm. 2D nanosheet nature of the samples was further verified from transmission electron microscope (TEM) images in Figures 3.5 (c) and 3.6 (c). High-resolution TEM (HRTEM) images of SnSe and Sn$_{0.94}$Bi$_{0.06}$Se nanosheets clearly show a lattice spacing of 3.06 Å, which corresponds to the (011) plane of SnSe (Figures 3.5 (d) and 3.6 (d)).
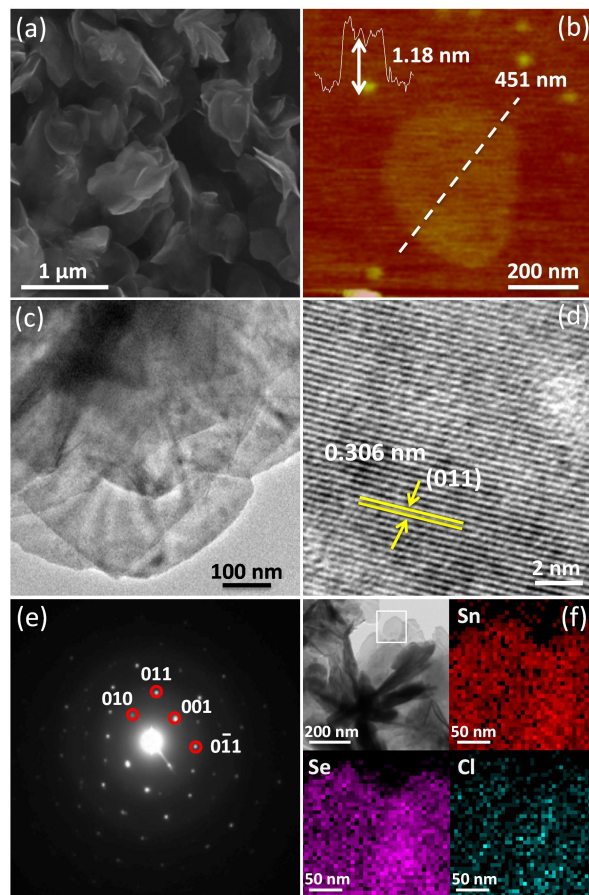
Figure 3.5 (a) FESEM image of SnSe nanosheets. (b) AFM image of single nanosheet of SnSe. (c) TEM image of SnSe nanosheets.(d) HRTEM image reveals the crystalline nature of the as-synthesized SnSe nanosheets. (e) SAED pattern of a single SnSe nanosheet. (f) STEM image of nanosheets and EDAX color mapping for Sn, Se and Cl.

The single crystalline nature of the nanosheets is confirmed from selected-area electron diffraction (SAED) pattern recorded from single nanosheet region (Figures 3.5 (e) and 3.6 (e)), which are indexed based on the orthorhombic SnSe structure. EDAX elemental color mapping has been done during scanning transmission electron microscopy (STEM) imaging which shows homogeneous distribution of all the respective elements in SnSe and $Sn_{0.94}Bi_{0.06}Se$ nanosheets (Figures 3.5 (f) and 3.6 (f)), which also confirms the successful Bi doping in SnSe.

In order to investigate thermoelectric properties of SnSe and Bi-doped SnSe few-layer nanosheets, capping reagent has been removed by heat-treatment of as-synthesized powder at 500 °C under N_2 flow. The conventional hydrazine treatment route for removal of capping agent
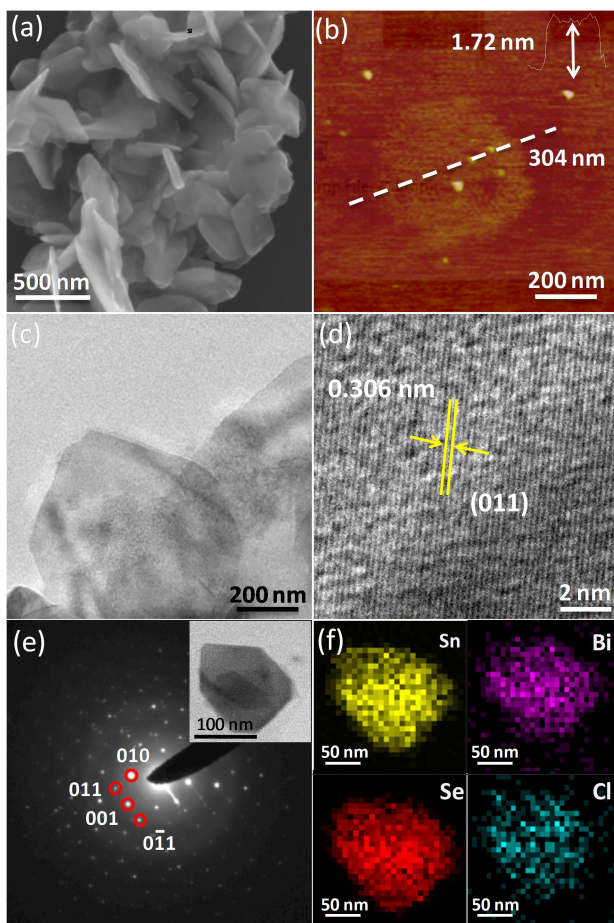
Figure 3.6 (a) FESEM image of $Sn_{0.94}Bi_{0.06}Se$ nanosheets. (b) AFM image of single nanosheet of $Sn_{0.94}Bi_{0.06}Se$. (c) TEM image of $Sn_{0.94}Bi_{0.06}Se$ nanosheets. (d) HRTEM image of $Sn_{0.94}Bi_{0.06}Se$ nanosheets. (e) SAED pattern of a single $Sn_{0.94}Bi_{0.06}Se$ nanosheet. Inset of (e) shows the STEM image of single nanosheet of $Sn_{0.94}Bi_{0.06}Se$. (f) EDAX color mapping of Sn, Se, Bi and Cl from the $Sn_{0.94}Bi_{0.06}Se$ nanoshhet shown in STEM image.

was avoided because SnSe reacts with hydrazine to form a SnSe-hydrazine hydrate adduct.[10]

During this heat treatment, no change in structure and composition was found, as indicated by PXRD patterns (Figure 3.7). The FTIR spectra confirms the removal of organic capping agent in the heating process (Figure 3.8).

To measure the thermoelectric properties, the surface cleaned nanosheets were pressed into pellets using SPS process at a pressure of 40 MPa and 450 °C under vacuum. The sample became more compact and the adjacent nanosheets are arranged on top of each other with negligible change in the nanoscale-grain size as seen from the FESEM images of the SPS-processed samples (Figure 3.9).
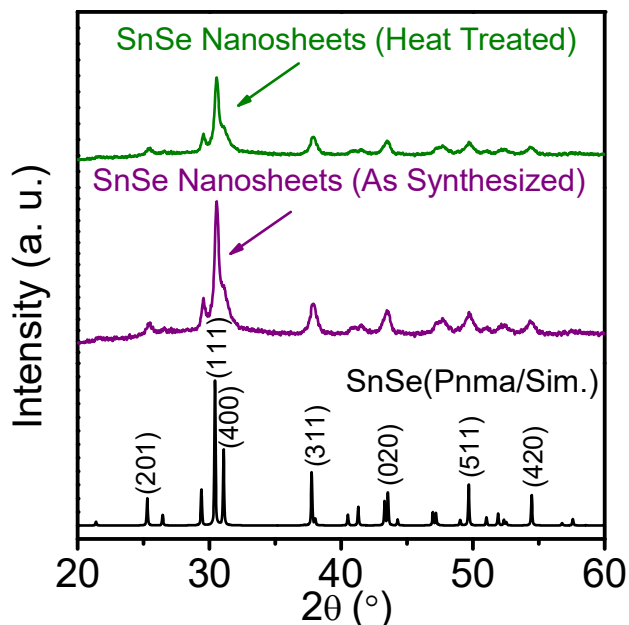
Figure 3.7 PXRD pattern of the synthesized SnSe nanosheets before and after the tube-furnace treatment at 500 ^{0}C.

As SnSe shows anisotropic transport properties originating from its layered structure (as depicted from PXRD in Figure 3.10), thermoelectric transport properties were measured both in parallel (∥) and perpendicular (⊥) to the pressing direction of SPS.
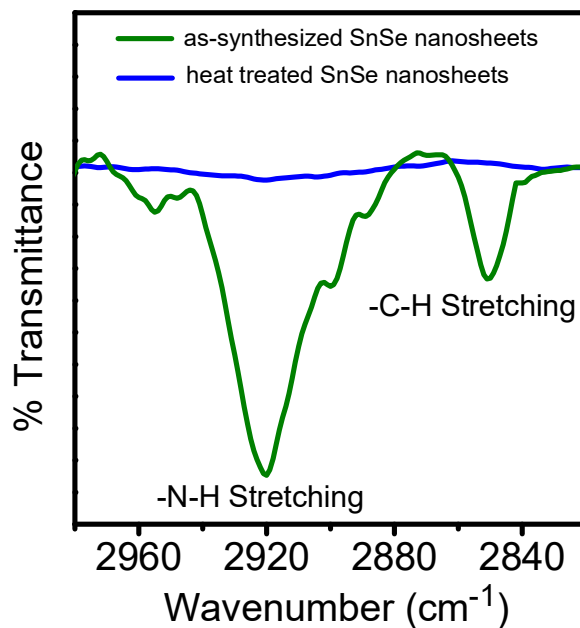
Figure 3.8 FT-IR spectra of SnSe nanosheets before and after the heat treatment
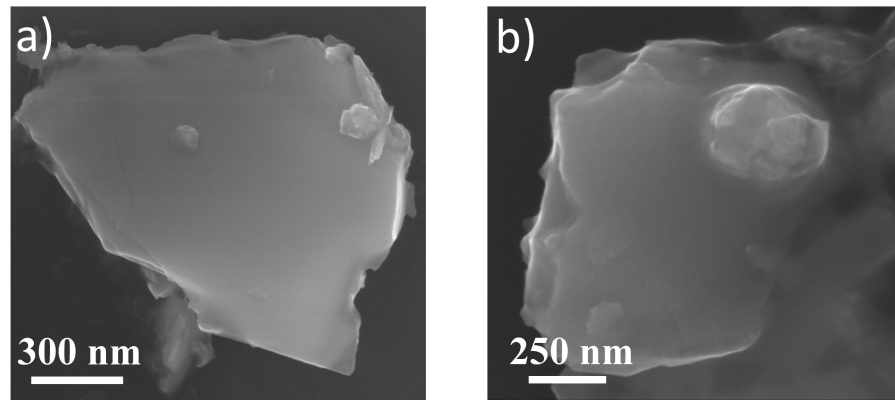
Figure 3.9 FESEM images of powder sample of SPS processed $Sn_{0.94}Bi_{0.06}Se$.

Figure 3.11 presents the temperature dependent thermoelectric properties (both in ∥ & ⊥ to SPS pressing directions) of SnSe and $Sn_{0.94}Bi_{0.06}Se$ nanosheets in the temperature range of 300-720 K. Electrical conductivity (σ) and Seebeck coefficient (S) were measured simultaneously under He atmosphere by a ULVAC-RIKO ZEM-3 instrument. Figure 3.11 (a) represents temperature dependence of σ for both SnSe and $Sn_{0.94}Bi_{0.06}Se$ samples. Being a semiconductor, electrical conductivity increases linearly with temperature for both the samples. The electrical conductivity measured along perpendicular to the SPS pressing direction is more
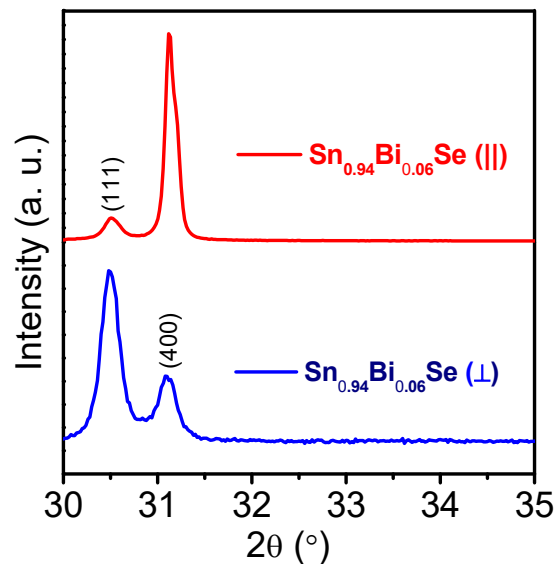
Figure 3.10 PXRD pattern of the as synthesized $Sn_{0.94}Bi_{0.06}Se$ nanosheets showing the anisotropy in (111) and (400) peaks for the parallel and perpendicular to the SPS pressing direction.

than those from parallel to the pressing direction, which can be attributed to favorable electronic transport in perpendicular to pressing direction (i.e. the c-axis, along the layers in SnSe, Figure 3.2 (a)), as also observed elsewhere.[11-13] Room temperature σ for SnSe nanosheets measured perpendicular to pressing direction is to be 0.28 Scm^{-1}, which increases to 9 Scm^{-1} at 719 K. Bi-doped nanosheets show superior electrical conductivity as compared to that of pristine SnSe. At room temperature, the σ values for the $Sn_{0.94}Bi_{0.06}Se$ nanosheets (for the $\perp$ to pressing direction) was 1.20 Scm^{-1}, which increases to 12.5 Scm^{-1} with increase in temperature.
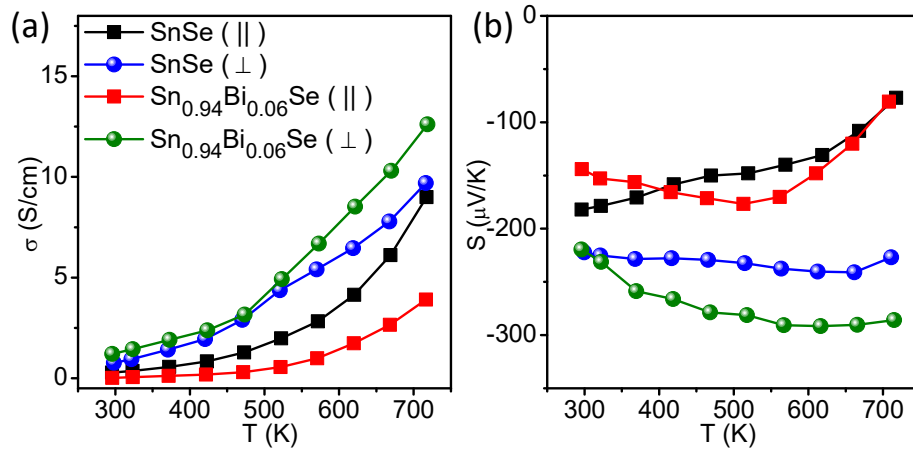
Figure 3.11 Temperature dependent (a) Electrical conductivity, (σ) (b)Seebeck coefficient, *(S)* of SnSe and $Sn_{0.94}Bi_{0.06}Se$ nanosheets measured along the SPS direction (indicated by squares) and perpendicular to the SPS direction (indicated by spheres).

The Hall coefficient of both the SnSe and $Sn_{0.94}Bi_{0.06}Se$ nanosheets is negative at room temperature, which confirms the *n*-type conduction. The *n*-type nature of SnSe can be attributed to the *in-situ* chlorination during synthesis as confirmed from ICP and EDAX analysis (Table 3.1). The room temperature *n*-type carrier concentration (*n*) for $Sn_{0.94}Bi_{0.06}Se$ nanosheets was estimated based on Hall measurement to be 1.97×10^{18} cm^{-3}, which is significantly higher compared to that of the pure SnSe nanosheet (3.08×10^{17} cm^{-3}). Substitution of Bi^{3+} at Sn^{2+} site contributes excess electron to conduction band, which results in enhanced *n*-type carrier concentration and electrical conductivity.
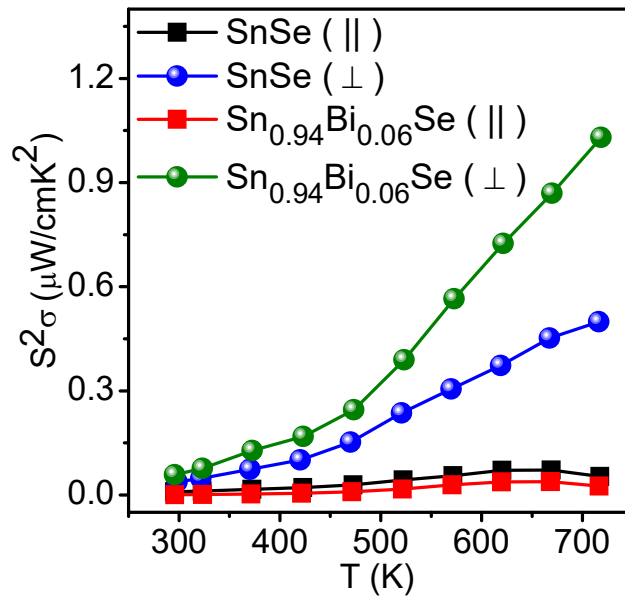
Figure 3.12 Temperature dependent Power factor, (σS^2).

Negative Seebeck coefficient (*S*) indicates the presence of *n*-type carriers in both the samples (Figure 3.11 (b)). Typically, $Sn_{0.94}Bi_{0.06}Se$ nanosheets ($\perp$ to pressing direction) has *S* value of -219 µV/K at 300 K, which increases to -285 µV/K at 719 K. Interestingly, we observe the *S* value is higher in the perpendicular to the pressing direction (along the *c*-axis in SnSe structure) than that of the parallel to the pressing direction, which is earlier observed in *n*-type Cl/Br-doped bulk SnSe.[12,13] Previous electronic structure calculation demonstrated the presence of a heavy conduction band (Γ-Z direction i.e. the c-axis in SnSe) along with the principal conduction band in SnSe.[14] Thus, high effective mass (*m**) of electron along the *c*-axis of SnSe ($\perp$ to the pressing direction) resulted high *S* value compared to that of the parallel to the pressing direction. $Sn_{0.94}Bi_{0.06}Se$ nanosheets sample exhibit higher power factor of 100 µW/mK^2 at 719 K which significantly higher than that of the SnSe (Figure 3.12).

The total thermal conductivity, κ_{total} (Figure 3.13 (a)) was estimated in the temperature range of $300 - 720$ K using the formula, $\kappa_{total} = DC_p\rho$, where *D* is the thermal diffusivity, C_p is
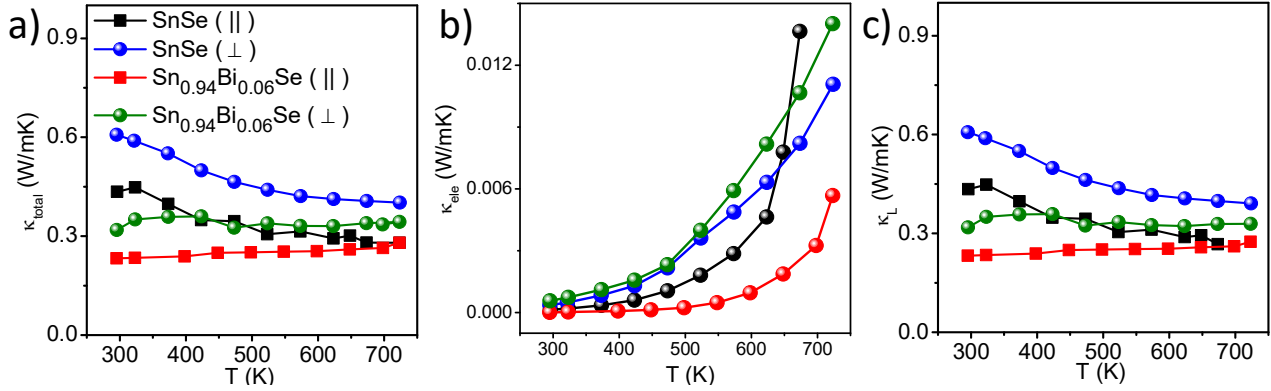
Figure 3.13 (a) Temperature dependent Total thermal conductivity, (κ_{total}) (b) electrical thermal conductivity (κ_{ele}) (c) Lattice thermal conductivity, (κ_L) of SnSe and Sn$_{0.94}$Bi$_{0.06}$Se nanosheets.

specific heat, and ρ is density of the sample. Temperature dependent (300-720 K) D has been measured by laser flash diffusivity technique in NETZSCH LFA 457 instrument. The κ_L was acquired by subtracting the electronic thermal conductivity, κ_{ele}, from the κ_{total}. The electronic thermal conductivities, κ_{ele} were evaluated (Figure 3.13 (b)) using Wiedemann-Franz Law, $\kappa_{ele} = L\sigma T$, where L is the Lorenz number which is calculated by fitting reduced chemical potential derived from temperature-dependent Seebeck coefficient using single parabolic band conduction and dominant acoustic phonon scattering of carriers. Sn$_{0.94}$Bi$_{0.06}$Se nanosheets show lower κ_L in the parallel to SPS pressing direction (i.e. *a*-axis in SnSe) compared to that of the perpendicular to the SPS pressing direction (i.e. *c*-axis of SnSe), which is attributed to phonon scattering by the interfaces between the layers (Figure 3.13 (c)). Typically, Sn$_{0.94}$Bi$_{0.06}$Se nanosheets exhibit ultralow κ_L of ~0.3 Wm^{-1}K^{-1} over 300–720 K measured perpendicular to SPS pressing direction which is in close proximity to the theoretical minimum, κ_{min} of SnSe (0.26 Wm^{-1}K^{-1})[11] *n*-type Sn$_{0.94}$Bi$_{0.06}$Se few-layer nanosheets ($\perp$ to the SPS pressing direction) demonstrate *zT* of 0.21 at 719 K, which is higher than that of *n*-type SnSe nanosheet sample (Figure 3.14).

3.4 Conclusions

In summary, *n*-type few-layer (2-4 layers) Bi-doped SnSe 2D nanosheets (1.2-3 nm thick) have been synthesized via facile low temperature solution based route. The *n*-type nature of $Sn_{0.94}Bi_{0.06}Se$ can be attributed to the *in-situ* chlorination and donor dopant nature of Bi. The presence of nanoscale grain boundaries and layered anisotropic structure enables the heat carrying phonons to get scattered significantly, thereby decreasing κ_L to as low as ~ 0.3 $Wm^{-1}K^{-1}$
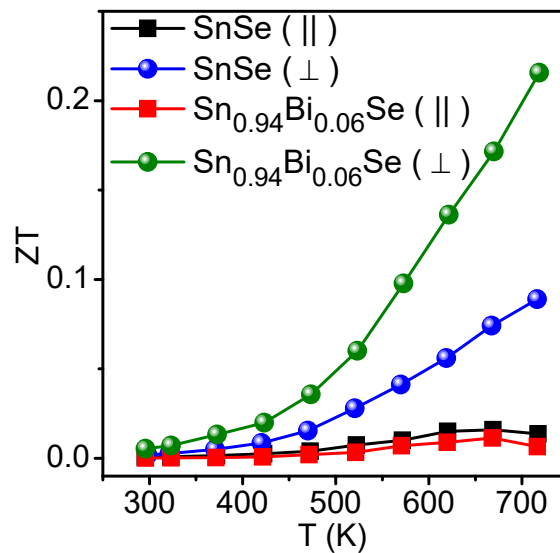
Figure 3.14 Temperature dependent Thermoelectric figure of merit, (*zT*).

over 300–720 K range. A combination of low thermal conductivity coupled with high power factor originated due to the enhancement of carrier concentration to 1.97×10^{18} cm^{-3}, gives rise to a *zT* of 0.21 at 719 K for 6% Bi-doped SnSe nanosheets, which is higher than that of *n*-type SnSe nanosheets.

References

[1]   Duong, A. T.; Nguyen, V. Q.; Duvjir, G.; Duong, V. T.; Kwon, S.; Song, J. Y.; Lee, J. K.; Lee, J. E.; Park, S.; Min, T.;*et al*. Achieving ZT = 2.2 with Bi-doped *n*-Type SnSe Single Crystals. *Nat. Commun.* **2016**, *7*, 13713.

[2]   Hu, C.-H.; Chiang, M.-H.; Hsieh, M.-S.; Lin, W.-T.; Fu, Y.-S.; Guo, T.-F. Phase Formation, Morphology Evolution and Tunable Bandgap of $Sn_{1-x}Sb_xSe$ Nanocrystals. *CrystEngComm* **2013**, *16*, 1786-1792.

[3]   Li, L.; Chen, Z.; Hu, Y.; Wang, X.; Zhang, T.; Chen, W.; Wang, Q. Single-Layer Single-Crystalline SnSe Nanosheets. *J. Am. Chem. Soc.* **2013**, *135*, 1213-1216.

[4]   Han, G.; Popuri, S. R.; Greer, H. F.; Bos, J. W. G.; Zhou, W.; Knox, A. R.; Montecucco, A.; Siviter, J.; Man, E. A.; Macauley, M.; *et al*. Facile Surfactant-Free Synthesis of *p*-Type SnSe Nanoplates with Exceptional Thermoelectric Power Factors. *Angew. Chem., Int. Ed.* **2016**, *55*, 6433-6437.

[5]   Han, G.; Popuri, S. R.; Greer, H. F.; Llin, L. F.; Bos, J.-W. G.; Zhou, W.; Paul, D. J.; Ménard, H.; Knox, A. R.; Montecucco, *et al*. Chlorine-Enabled Electron Doping in Solution-Synthesized SnSe Thermoelectric Nanomaterials. *Adv. Energy Mater.* **2017**, *7*, 1602328.

[6]   Zhao, L.-D.; Lo, S.-H.; Zhang, Y.; Sun, H.; Tan, G.; Uher, C.; Wolverton, C.; Dravid, V. P.; Kanatzidis, M. G. Ultralow Thermal Conductivity and High Thermoelectric Figure of Merit in SnSe Crystals. *Nature* **2014**, *508*, 373-377.

[7]   Zhao, L.-D.; Tan, G.; Hao, S.; He, J.; Pei, Y.; Chi, H.; Wang, H.; Gong, S.; Xu, H.; Dravid, V. P.; *et al*. Ultrahigh Power Factor and Thermoelectric Performance in Hole-Doped Single-Crystal SnSe. *Science* **2016**, *351*, 141-144.

[8]   Banik, A.; Biswas, K. Synthetic Nanosheets of Natural van der Waals Heterostructures. *Angew. Chem., Int. Ed.* **2017**, *56*, 14561-14566.

[9]   Saha, S.; Banik, A.; Biswas, K. Few-Layer Nanosheets of *n*-Type SnSe$_2$. *Chem. Eur. J.* **2016**, *22*, 15634-15638.

[10]   Mitzi, D. B. Synthesis, Structure, and Thermal Properties of Soluble Hydrazinium Germanium (IV) and Tin (IV) Selenide Salts. *Inorg. Chem.* **2005**, *44*, 3755-3761.

[11]   Zhang, Q.; Chere, E. K.; Sun, J.; Cao, F.; Dahal, K.; Chen, S.; Chen, G.; Ren, Z. C. Studies on Thermoelectric Properties of *n*-Type Polycrystalline SnSe$_{1-x}$S$_x$ by Iodine Doping. *Adv. Energy Mater.* **2015**, *5*, 1500360.

[12]   Xue, W.; Jingtao, X.; Guoqiang, L.; Yajie, F.; Zhu, L.; Xiaojian, T.; Hezhu, S.; Haochuan, J.; Tianya, T.; Jun, J. Optimization of Thermoelectric Properties in *n*-Type SnSe Doped with BiCl$_3$. *Appl. Phys. Lett.* **2016**, *108*, 083902.

[13]   Chang, C.; Tan, Q.; Pei, Y.; Xiao, Y.; Zhang, X.; Chen, Y.-X.; Zheng, L.; Gong, S.; Li, J.-F.; He, J.;*et al*. Raising Thermoelectric Performance of *n*-Type SnSe via Br Doping and Pb Alloying. *RSC Adv.* **2016**, *6*, 98216-98220.

[14]   Kutorasinski, K.; Wiendlocha, B.; Kaprzyk, S.; Tobola, J. Electronic Structure and Thermoelectric Properties of *n*- and *p*-Type SnSe From First-Principles Calculations. *Phys. Rev. B* **2015,** *91*, 205201.

Chapter 4

Evolution of Crystal and Electronic Structure of SnSe by AgBiSe$_2$ Alloying*

Evolution of Crystal and Electronic Structure of SnSe by AgBiSe$_2$ Alloying

Summary: *Recently, tin selenide (SnSe) has attracted extensive attention for the reported excellent thermoelectric performance. SnSe, a narrow band-gap semiconcuctor, crystallizes into a layered orthorhombic structure at ambient conditions. Interestingly, the high symmetry cubic phase of SnSe is predicted to be stabilized by applying 15 GPa external pressure which is calculated to be a topological crystalline insulator (TCI). In a recent study by Wencan Jin et. al., TCI has been observed in rock-salt SnSe {111} thin films. But, till date there are no reports of the experimental stabilization of bulk cubic SnSe. Herein, for the first time, we have stabilized the cubic phase of SnSe at ambient conditions by alloying with 30 mol% of AgBiSe$_2$. The increase in chemical pressure originating from the substitution of AgBiSe$_2$ in SnSe matrix decreases the band gap of orthorhombic SnSe and for cubic SnSe the band band-gap approaches nearly to 0 eV. This study provides an insight into electronic structure and thermoelectric properties of novel bulk phase of cubic SnSe.*

4.1 Introduction

Topological insulators (TIs) have drawn an immense interest in Solid State Chemistry and Condensed Matter Physics recently, owing to their unique conductive properties.[1] TIs are a new quantum state of matter with a bulk band gap typically generated by a strong spin orbit coupling and topologically protected linearly dispersed metallic surface states.[1] TIs have different electronic structures compared to conventional semiconductors and insulators with special characteristic topologically protected metallic surface states.[2] TIs possess an odd number of band inversions between valence and conduction band owing to strong spin orbit coupling.[3] Metallic surface states of TIs are protected by time-reversal symmetry, thus surface states in TIs are robust against almost any type of chemical surface modification.[3]

Many TIs are known to be good thermoelectric (TE) materials because of the requirement of similar features in the electronic band structure.[4] The primary criteria for good TE and TI materials are relatively similar as both require heavy elements and narrow band gap semiconducting electronic structure.[4]

TCIs are a new class of quantum materials[5] that are fundamentally different from conventional TIs in terms of their surface state protection mechanism. TI surface states are protected by time-reversal symmetry, while TCI surface states are protected by crystal mirror symmetry.[5] Thus, breaking of crystal mirror symmetry can alter the electronic structure of TCI. Recently, crystal symmetry in TCI was broken by various external physical perturbations, such as by applying electric fields, ferroelectric structural distortion, mechanical strain, and thickness engineering.[5,6]

Recently, solid solution composition, $Pb_{0.6}Sn_{0.4}Te$[7] derived from the well-known thermoelectric materials, PbTe (Eg. 0.29 eV)[4] and SnTe (Eg. 0.18 eV, inverted gap),[8] has been

discovered to be a TCI by angle-resolved photoemission spectroscopy (ARPES).[9] High-resolution scanning tunneling microscopy/spectroscopy measurements revealed the crystal symmetry-breaking and distortion of the surface of TCI, which resulted in opening of band gap and massive Dirac fermion formation.[5e] Furthermore, applying an electric field perpendicular to the thin films of SnTe and $Pb_{1-x}Sn_xSe(Te)$ grown along (001) direction breaks the mirror symmetry, resulting in the opening of a band gap from the edge states.[5d] Very recently, the TCI phase in a metastable SnSe {111} thin film with rock-salt structure has been observed and was found to be Se terminated and hydrogen passivated using first-principles calculations.[10a] Later, Wencan Jin et. al., experimentally verified the existence of the TCI phase in Sn terminated rock-salt SnSe {111} thin film epitaxially grown on Bi_2Se_3.[10b]
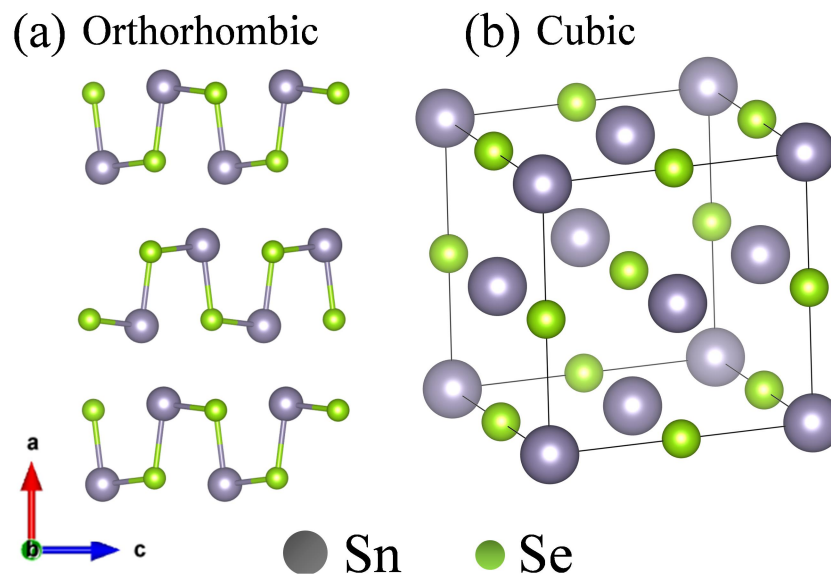
Figure 4.1 Crystal structure of different phases of SnSe: (a) Orthorhombic (Pnma) and (b) Face-centered cubic (Fm-3m).

SnSe crystallizes in two different structures: orthorhombic (Pnma) and cubic phases (Fm-3m) (Figure 4.1) depending on the temperature and pressure conditions. At ambient conditions, SnSe possess orthorhombic cystal structure, which shows an unprecedented zT in the single-

crystal form owing to ultralow thermal conductivity.[11] But TCI phase is only predicted for rock-salt SnSe.[10] Since the high symmetry cubic phase can only be stabilized at very high pressure of 15 GPa,[10c] till date there are no experimental reports of TCI on bulk cubic SnSe. Thus, the experimental realization of cubic SnSe still remains elusive.

In this chapter, for the very first time, we have successfully stabilized the cubic phase of SnSe with 30 mol% AgBiSe₂ alloying at ambient conditions. We find that the phase transition from orthorhombic to cubic SnSe is induced by alloying with AgBiSe₂ due to the interplay of chemical pressure. Orthorhombic SnSe is a direct band gap semiconductor (band gap = 0.99 eV) consisting six degenerate valence bands near Fermi level,[11] but, the band gap approaches to zero for cubic rock-salt $(SnSe)_{1-x}(AgBiSe_2)_x$ (x = 0.30-0.70). This study gives a brief overview about the structural details and thermoelectric properties of cubic $(SnSe)_{1-x}(AgBiSe_2)_x$.

4.2 Experimental Section

4.2.1 Reagents. Tin (Alfa Aesar 99.99+ %), silver (Ag, Aldrich 99.999%), bismuth (Alfa Aesar 99.9999%), and selenium (Se, Alfa Aesar 99.9999%) were used for synthesis without further purification.

4.2.2 Synthesis. Ingots (~ 4 g) of $(SnSe)_{1-x}(AgBiSe_2)_x$ (x = 0 – 0.6) were synthesized by mixing stoichiometric ratios of elemental Sn, Ag, Bi and Se in quartz tubes. The tubes were sealed under vacuum (10^{-5} Torr) and slowly heated to 723 K over 12 hrs, and then heated up to 1223 K in 5 hrs followed by annealing for 10 hrs, and then slowly cooled down to room temperature over a period of 18 hrs.

4.2.3 Powder X-ray diffraction. Room temperature powder X-ray diffraction for all of the samples were recorded using a Cu K_α (λ = 1.5406 Å) radiation on a Bruker D8 Diffractometer.

Rietveld refinement of the PXRD pattern was performed using FULLPROF software.

4.2.4 Band gap measurement. To estimate optical band gap of the as-synthesized specimens of $(SnSe)_{1-x}(AgBiSe_2)_x$ (x = 0, 0.05, 0.10, 0.20, 0.30, 0.40, 0.50, 0.60, 0.70, 0.80. 0.90, 1.00), diffuse reflectance measurements were carried out with finely grounded powder at room temperature using a Perkin-Elmer Lambda 900 UV/Vis/near-IR spectrometer in reflectance mode (λ = 2500-250 nm) and FT-IR Bruker IFS 66V/S spectrometer (λ = 4000-400 cm^{-1}), respectively. Absorption (α/S) data were calculated from the reflectance data using Kubelka-Munk equation: $\alpha/S = (1-R)^2/(2R)$, where R is the reflectance, α and S are respectively the absorption and scattering coefficients. The energy band gaps were then determined from α/S vs. E (eV) plot.

4.2.5 Electrical transport. Electrical conductivity and Seebeck coefficients were measured simultaneously under helium atmosphere from room temperature to 723 K on a ULVAC-RIKO ZEM-3 instrument system. The sample for measurement had a rectangular shape with the dimensions of ~ 2 × 2 × 8 mm^3. The longer direction coincides with the direction in which the thermal conductivity was measured. Heating and cooling cycles gave reversible electrical properties for given samples.

4.2.6 Hall measurement. For determining the carrier concentrations, Hall measurements were carried out on the same rectangular specimens used for electrical transport measurement in four-contact geometry up to a magnetic field of 0.57 T at room-temperature using custom-built equipment developed by Excel Instruments.

4.2.7 Thermal transport. Thermal diffusivity, D, was directly measured in the range 300−723 K by using laser flash diffusivity method in a Netzsch LFA-457. Coins with 8 mm diameter and 2 mm thickness were used in all of the measurements. Temperature dependent heat capacity, C_p,

was derived using standard sample (pyroceram) in LFA-457. Total thermal conductivity, κ, was calculated using the formula, $\kappa = D.C_p.\rho$, where ρ is the density of the sample, measured using the sample dimension and mass. The density of the pellets was ~98% of the theoretical density.

4.2.8 Computational details. The DFT calculations have been carried out with the collaboration with Prof. Waghmare's group from JNCASR. We use density functional theoretical (DFT) methods as implemented in QUANTUM ESPRESSO (QE) code. We used a generalized gradient approximation (GGA) to the exchange-correlation energy functional as parameterized by Perdew, Burke, and Ernzerhof (PBE). To describe the interactions between valence electrons and ions we used Projected Augmented–Wave (PAW) potentials. Electronic wave functions and charge density were represented in plane wave basis sets truncated with cut-off energies of 45 Ry and 360 Ry respectively. The discontinuity in occupation numbers of electronic states was smeared using a Fermi-Dirac distribution function with broadening of $k_B T$ = 0.003 Ry. We determined electronic structure of SnSe and $(SnSe)_{0.66}(AgBiSe_2)_{0.33}$ using their fully optimized structures. At ambient conditions, SnSe stabilizes in the orthorhombic phase containing eight atoms in the unit cell, and we consider this phase in our theoretical analysis. Integrations over Brillouin Zone (BZ) were sampled on a uniform 8x8x8 mesh of k-points. Electronic spectrum was determined at Bloch vectors along high symmetry lines (Γ - X - S - Y -Γ - Z - U - R - T - Z - Y - T -U - X - S) in the Brillouin zone. With increase in concentration of AgBiSe₂, a rock-salt phase is stabilized. $(SnSe)_{0.66}(AgBiSe_2)_{0.33}$ exists in the cubic structure consisting of 16 atoms in the unit cell. To simulate this composition, a $\sqrt{2}x\sqrt{2}x1$ supercell was considered, and Brillouin Zone (BZ) integrations were sampled on a uniform 10x12x12 mesh of k points. Electronic spectrum was determined at Bloch vectors along high symmetry lines (Γ - X - M - Γ - Z - R - A - Z) in the Brillouin zone of FCC lattice. We compared electronic structures with and without

spin-orbit coupling (SOC) using fully relativistic and scalar relativistic potentials respectively. Our optimized lattice parameters for pristine SnSe in the orthorhombic structure (Pnma) are a = 11.77 Å, b = 4.22 Å, c = 4.53 Å, which agree with the typical GGA errors with experimental lattice parameters (a = 11.97 Å, b = 4.19 Å, c = 4.46 Å). The experimental lattice parameters of the cubic $(SnSe)_{0.66}(AgBiSe_2)_{0.33}$ are a = 8.36Å, b = 8.36Å, c = 5.91Å and the theoretical lattice parameters are a = 8.43Å, b = 8.43Å, c = 5.96Å (for the $\sqrt{2}x\sqrt{2}x1$ supercell), which was used for understanding the effect of disordering.

4.3 Results and Discussion

The room-temperature powder X-ray diffraction (PXRD) pattern of pristine SnSe obtained using laboratory X-ray source could be indexed based on the orthorhombic phase at room temperature (Figure 4.2). Orthorhombic SnSe (space group Pnma), when alloyed with $AgBiSe_2$, gradually transforms to the face-centered cubic structure at ambient conditions.
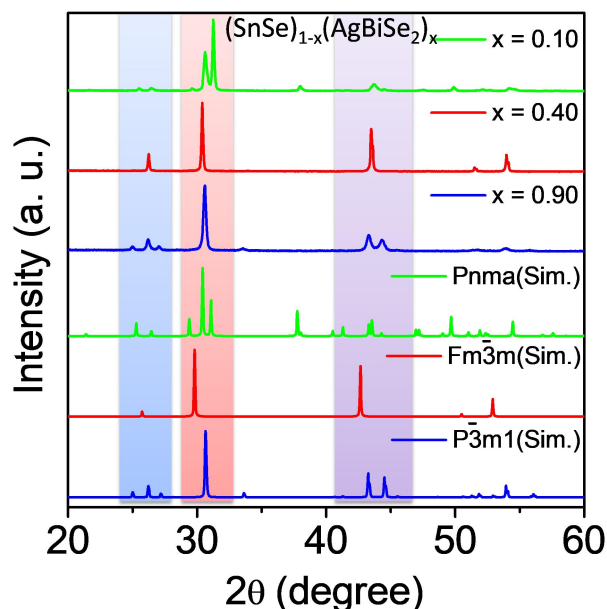
Figure 4.2 Room-temperature PXRD patterns (Laboratory source, Cu Kα (λ = 1.5406 Å) of $(SnSe)_{1-x}(AgBiSe_2)_x$ (x=0.10, 0.40, 0.90) manifesting the structural phase evolution from orthorhombic to cubic.

With the addition of 30 mol% AgBiSe$_2$ in SnSe, a pure rock-salt (space group Fm-3m) phase starts to appear. A pure-phase cubic compound is sustained up to x > 0.70 in (SnSe)$_{1-x}$(AgBiSe$_2$)$_x$ composition. With further addition of AgBiSe$_2$ (more than x = 0.80), we observe the formation of phase-pure hexagonal AgBiSe$_2$ (space group P-3m1).
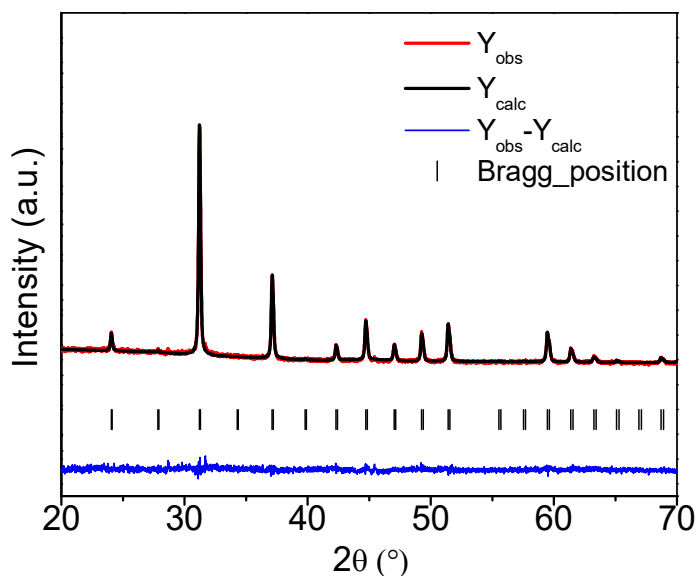
Figure 4.3 Rietveld refinement of PXRD pattern of (SnSe)$_{0.60}$(AgBiSe$_2$)$_{0.40.}$

The Rietveld refinement (Figure 4.3) of the PXRD patterns of (SnSe)$_{0.60}$(AgBiSe$_2$)$_{0.40}$ indicates that when AgBiSe$_2$ is added into the SnSe system, the Ag and Bi atoms preferentially occupies the Sn sites and create substitutional disorder (Table 4.1). The increasing substitutional disorder with the increase of AgBiSe$_2$ concentration in the system leads to the enhancement of configurational entropy and the consequent stabilization of the high symmetry cubic phase at room temperature.

This is similar to the phenomenon generally found in high entropy alloys where the addition of extra elements stabilizes high symmetry phases owing to the enhancement of entropy of the alloy system.[12] The entropy engineering is an effective approach to optimize the thermoelectric performance of a material because it elevates the symmetry of then crystal

structure, which in turn helps to achieve high Seebeck coefficient and reduces thermal conductivity by increasing the point defect concentrations, which can scatter heat carrying phonons effectively.

Table 4.1 Structural parameters of Rietveld refinement for $(SnSe)_{0.60}(AgBiSe_2)_{0.40}$ sample.
Space group: Fm-3m; a=b = c = 5.8413 Å, α = β = ɣ = 90°

Constitute Elements	x/a	y/b	z/c	Occupancy	χ^2
Sn	0	0	0	0.3681	
Ag	0	0	0	0.3187	
Bi	0	0	0	0.3133	2.53
Se	0.5	0.5	0.5	1	

The phase diagram of the SnSe-AgBiSe$_2$ system, as inferred from room- temperature PXRD and DSC analysis is shown in Figure 4.4. The phase boundaries are, however, relative to the position of the orthorhombic, and cubic phases because of the limited amount of data set studied in this work.
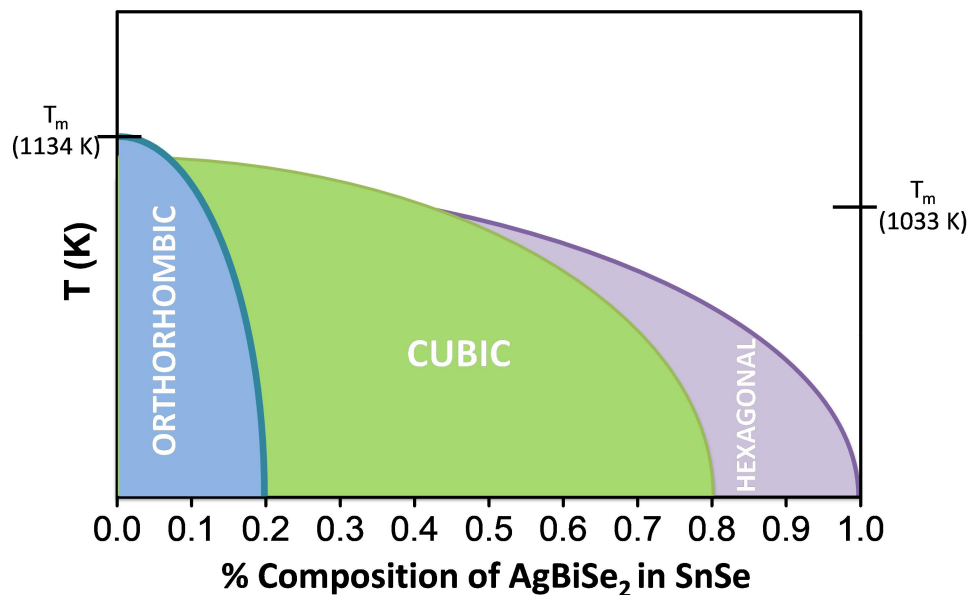
Figure 4.4 A possible phase diagram of the SnSe-AgBiSe$_2$ system based on PXRD and DSC data.

However, this phase diagram helps to identify that the increase of AgBiSe$_2$ concentration in SnSe causes a structural phase evolution from orthorhombic to a rock-salt structure as the AgBiSe$_2$ concentration increases further. We intend to do the temperature dependent XRD to generate more reliable phase diagram in future.
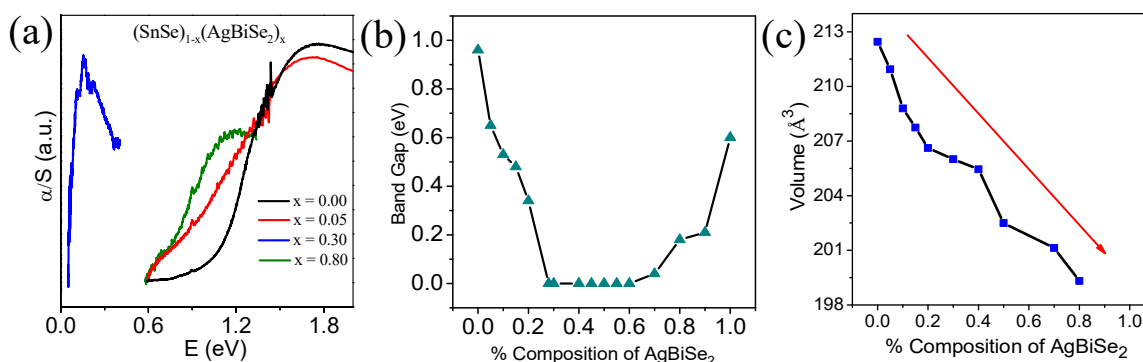
Figure 4.5 (a) and (b) Band gap evolution and (c) Unit cell volume of (SnSe)$_{1-x}$(AgBiSe$_2$)$_x$ vs. AgBiSe$_2$ concentration concentration.

The band gap of pristine orthorhombic SnSe is measured to be about 0.99 eV (Figure 4.5 a). However, when SnSe is alloyed with AgBiSe$_2$, band gap rapidly decreases to about 0.37 eV at x = 0.20 (Figure 4.5 b) in the orthorhombic phase owing to increase in chemical pressure originating from a sharp decrease in unit cell volume from 213 Å^3 (orthorhombic) to 206 Å^3 (Figure 4.5 c). When the concentration of AgBiSe$_2$ increases above x = 0.2, the band gap approaches nearly to 0 eV. The contraction of the unit cell during orthorhombic (213 Å^3) to cubic phase (205 Å^3) transition increases the chemical pressure, which consequently cloes the band gap. To study the evolution of band gap with respect to the alloying concentration, we have preliminarily calculated the electronic band structure at two concentrations: pristine SnSe (orthorhombic), and (SnSe)$_{0.66}$(AgBiSe$_2$)$_{0.33}$ (rock-salt) by density functional theoretical (DFT) calculation (Figure 4.6) with and without spin–orbit coupling (SOC). The theoretical band gap of SnSe in the orthorhombic structure is 0.71 eV irrespective of the inclusion of SOC, which is

slightly lower than that of the experimental band gap of 0.99 eV, that is common in the DFT calculation of bang gaps.
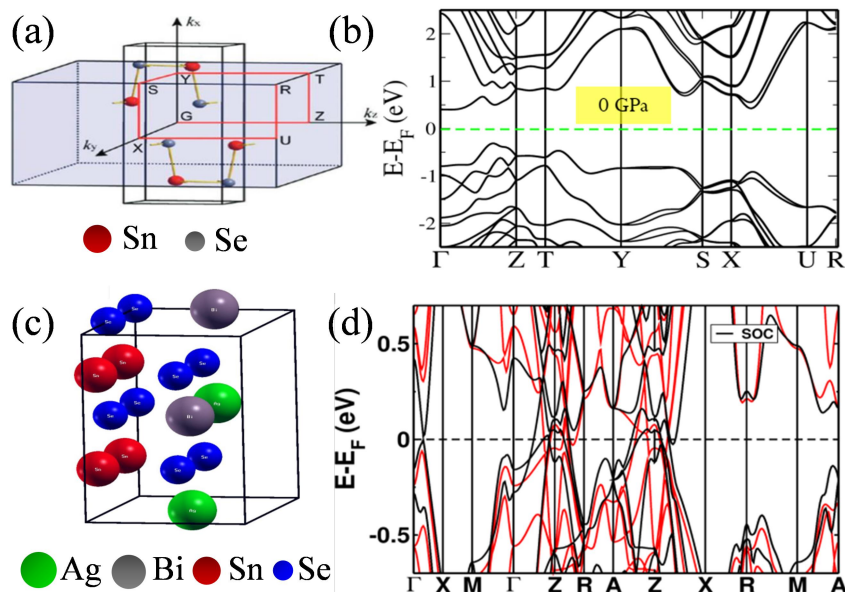
Figure 4.6 (a) 8 atom unit cell and (b) electronic band structure of orthorhombic SnSe, (c) 16 atom unit cell and (d) electronic band structure of $(SnSe)_{0.66}(AgBiSe_2)_{0.33}$ with (black lines) and without (red lines) the inclusion of spin–orbit coupling (SOC).

We find that the band gap of SnSe decreases with AgBiSe₂ alloying, consistent with the trend observed in experimental measurements (Figure 4.5 b). Electronic structures of the 16 atoms cubic FCC unit cell ($\sqrt{2}$x$\sqrt{2}$x1) of $(SnSe)_{0.66}(AgBiSe_2)_{0.33}$ (Figure 4.6 c) calculated with spin orbit coupling (SOC) reveals no overlap between valence and conduction band (Figure 4.6 d).

Thermoelectric properties are measured for cubic $(SnSe)_{1-x}(AgBiSe_2)_x$ (x = 0–0.50) and compared with to that of the pristine orthorhombic SnSe (measured along parallel to the pressing direction). For all the $(SnSe)_{1-x}(AgBiSe_2)_x$ (x = 0–0.50) samples, electrical conductivity increases with increasing temperature which indicates the semiconducting transport (Figure 4.7 a). The σ of pristine orthorhombic SnSe is 0.717 Scm^{-1} at 300 K, which increases to about 170 Scm^{-1} upon 40 mol% AgBiSe₂ alloying at room temperature.
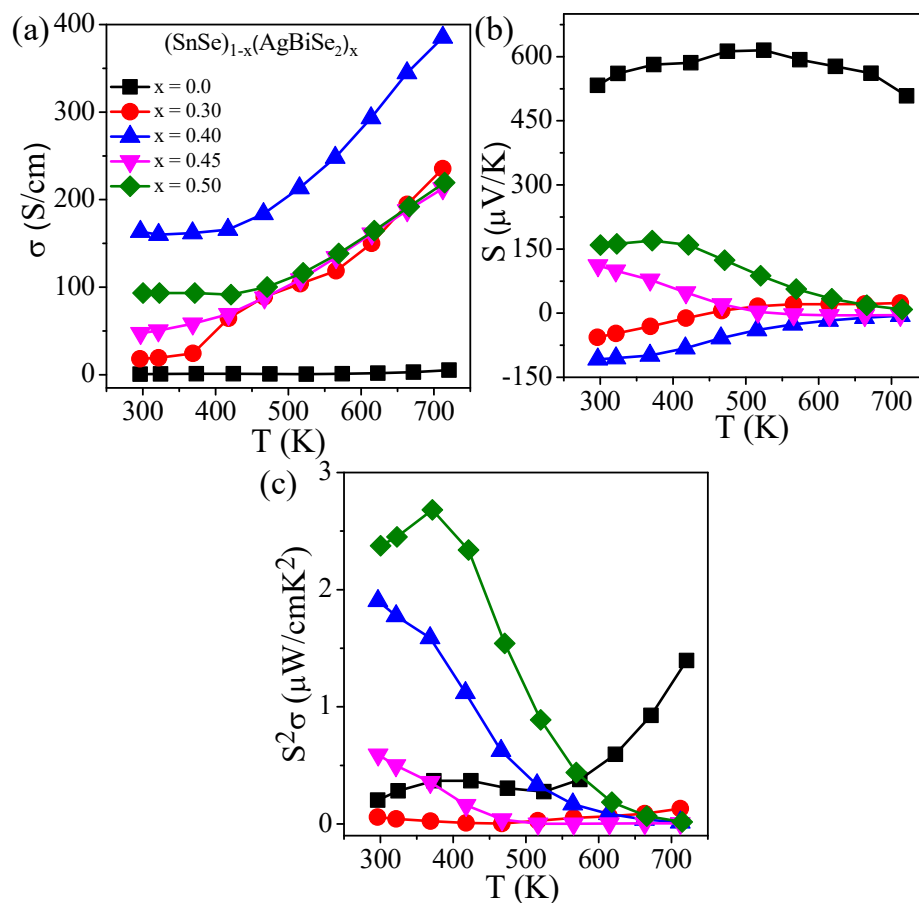
Figure 4.7 Temperature dependent (a) electrical conductivity (σ), (b) Seebeck coefficient (S) and (c) power factor ($S^2\sigma$) of $(SnSe)_{1-x}(AgBiSe_2)_x$ (x = 0–0.50) samples.

Several attempts have been made in the past few years to increase the carrier concentration in SnSe using p-type dopants such as Ag, Pb, K, Na [13] or n-type dopants like Sb, S, I [14] etc. Solid solution of SnSe with AgBiSe₂ increases σ significantly due to the enhancement in the carrier concentration from 3×10^{17} cm^{-3} (p-type) for pristine SnSe to 6.17×10^{19} cm^{-3} in n-type $(SnSe)_{0.60}(AgBiSe_2)_{0.40}$. Typically, the room temperature σ of $(SnSe)_{0.60}(AgBiSe_2)_{0.40}$ is found to be about 170 Scm^{-1}, which increases to about 385 Scm^{-1} at 723 K.

The measured value of the Seebeck coefficient (S) of pristine orthorhombic SnSe is 527 μVK^{-1} at 300 K (Figure 4.7 b), which decreases to -109.05 μVK^{-1} for $(SnSe)_{0.60}(AgBiSe_2)_{0.40}$. Holes are the majority carriers in orthorhombic SnSe making it a p-type semiconductor, which is

also confirmed by the positive value of Hall coefficient. However, the cubic $(SnSe)_{1-x}(AgBiSe_2)_x$ (x= 0.30 to 0.50) shows anomalous trend in S values. This arises mainly due to the onset of bipolar conduction. For all the $(SnSe)_{1-x}(AgBiSe_2)_x$ (x= 0.30 to 0.50) samples, S approaches toward zero at 723K (Figure 4.7 b) which can be a direct implication of the fact that band-gap closes for the cubic $(SnSe)_{1-x}(AgBiSe_2)_x$ alloys. The n-type carrier concentration is also in good agreement with the negative sign of Hall coefficients for $(SnSe)_{0.60}(AgBiSe_2)_{0.40}$ sample. Bi^{3+} substitution in place of Sn^{2+} acts as a donor dopant and increases the n-type carrier concentration. Cubic $(SnSe)_{0.50}(AgBiSe_2)_{0.50}$ exhibits higher power factor of 2.7 $\mu Wcm^{-1}K^{-2}$ near room temperature (300 K) which approaches to zero at 723 K. Thus there is no significant enhancement in power factor for cubic SnSe as compared to pristine orthorhombic SnSe.

Orthorhombic pristine SnSe exhibits lattice thermal conductivity (κ_{lat}) of 0.98 $Wm^{-1}K^{-1}$ at 300 K, which decreases to 0.38 $Wm^{-1}K^{-1}$ at 723 K (Figure 4.8). When SnSe is alloyed with AgBiSe₂, κ_{lat} in the cubic $(SnSe)_{1-x}(AgBiSe2)_x$ (x = 0.30, 0.40) increases significantly to ~ 0.9 $Wm^{-1}K^{-1}$ at 300 K (Figure 4.8) and it further continues to increase at higher temperature. The low
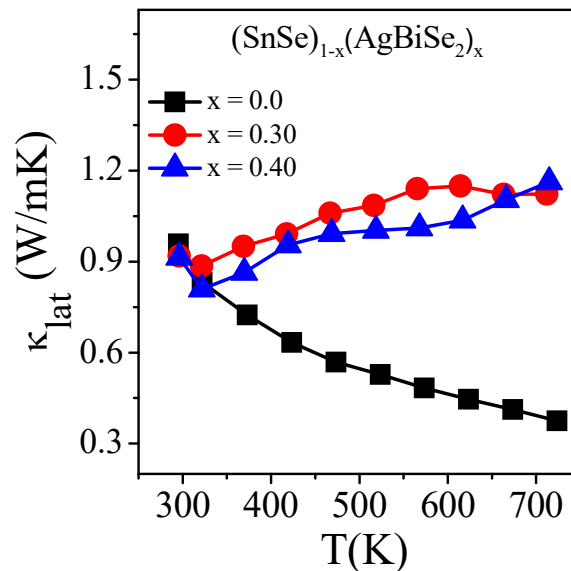
Figure 4.8 Temperature dependent lattice thermal conductivity (κ_{lat}) of $(SnSe)_{1-x}(AgBiSe_2)_x$ (x = 0–0.40) samples.

low lattice thermal conductivity in SnSe originates mainly due the damping phonon vibrations at the layers of SnSe and for the presence of optically active Sn $5s^2$ lone-pair which scatters the phonons significantly.[11] But in the as-synthesized cubic $(SnSe)_{1-x}(AgBiSe_2)_x$ (x = 0.30, 0.40), the total thermal conductivity increases drastically which is mainly due to the destruction of the layered orthorhombic crystal structure.

4.4 Conclusions

In conclusion, the high-pressure cubic rock-salt phase of SnSe has been stabilized at ambient conditions by interplay of chemical pressure and introduction of high entropy with $AgBiSe_2$ alloying. The anomalous closing of the band gap of SnSe with increasing $AgBiSe_2$ concentration is due to the influence of increase in chemical pressure. Interestingly, cubic $(SnSe)_{0.60}(AgBiSe_2)_{0.40}$ possess *n*-type conduction with reasonable high carrier concentration. This report establishes cubic $(SnSe)_{0.60}(AgBiSe_2)_{0.40}$ as a new *n*-type thermoelectric material and their performance can be improved further by carrier engineering such as aliovalent halide doping. Besides, further experimental proof supported by extensive DFT calculations are required to prove the existence of TCI phase in bulk rock-salt SnSe, which we intend to do in future.

References

[1]   (a) Müchler, L.; Zhang, H.; Chadov, S.; Yan, B.; Casper, F.; Kübler, J.; Zhang, S. C.; Felser, C., Topological Insulators from a Chemist's Perspective. *Angew. Chem. Int. Ed.* **2012,** *51*, 7221. (b) Hsieh, D.; Qian, D.; Wray, L.; Xia, Y.; Hor, Y. S.; Cava, R. J.; Hasan, M. Z., A topological Dirac insulator in a quantum spin Hall phase. *Nature* **2008,** *452*, 970. (c) Xiao-Liang, Q.; Shou-Cheng, Z., The quantum spin Hall effect and topological insulators. *Phys. Today* **2010,** *63*, 33. (d) Moore, J. E., The birth of topological insulators. *Nature* **2010,** *464*, 194. (e) Yan, B.; Zhang, S.-C., Topological materials. *Rep. Prog. Phys.* **2012,** *75*, 096501.

[2]   (a) Wang, Z. H.; Yang, L.; Li, X. J.; Zhao, X. T.; Wang, H. L.; Zhang, Z. D.; Gao, X. P. A., Granularity Controlled Non-saturating Linear Magnetoresistance in Topological Insulator Bi₂Te₃ Films. *Nano Lett.* **2014,** *14*, 6510. (b) Chatterjee, A.; Biswas, K., Solution-Based Synthesis of Layered Intergrowth Compounds of the Homologous Pb$_m$Bi$_{2n}$Te$_{3n+m}$ Series as Nanosheets. *Angew. Chem., Int. Ed.* **2015,** *54*, 5623.

[3]   (a) Kong, D.; Cui, Y., Opportunities in chemistry and materials science for topological insulators and their nanostructures. *Nat. Chem.* **2011,** *3*, 845. (b) Wang, X.; Du, Y.; Dou, S.; Zhang, C., Room Temperature Giant and Linear Magnetoresistance in Topological Insulator Bi₂Te₃ Nanosheets. *Phys. Rev. Lett.* **2012,** *108*, 266806.

[4]   (a) Müchler, L.; Casper, F.; Yan, B.; Chadov, S.; Felser, C., Topological insulators and thermoelectric materials. *Phys. Status Solidi RRL* **2012,** *7*, 91. (b) Sootsman, J. R.; Chung, D. Y.; Kanatzidis, M. G., New and Old Concepts in Thermoelectric Materials. *Angew. Chem. Int. Ed.* **2009,** *48*, 8616. (c) Zhao, L. D.; Dravid, V. P.; Kanatzidis, M. G., The panoscopic approach to high performance thermoelectrics. *Energy Environ. Sci.* **2014,** *7*, 251. (d) Biswas, K.; He, J.; Blum, I. D.; Wu, C.-I.; Hogan, T. P.; Seidman, D. N.; Dravid, V. P.;

Kanatzidis, M. G., High-performance bulk thermoelectrics with all-scale hierarchical architectures. *Nature* **2012,** *489*, 414. (e) Biswas, K.; He, J.; Zhang, Q.; Wang, G.; Uher, C.; Dravid, V. P.; Kanatzidis, M. G., Strained endotaxial nanostructures with high thermoelectric figure of merit. *Nat. Chem.* **2011,** *3*, 160. (f) Guin, S. N.; Chatterjee, A.; Negi, D. S.; Datta, R.; Biswas, K., High thermoelectric performance in tellurium free *p*-type AgSbSe$_2$. *Energy Environ. Sci.* **2013,** *6*, 2603. (g) Banik, A.; Roychowdhury, S.; Biswas, K., The journey of tin chalcogenides towards high-performance thermoelectrics and topological materials. *Chem. Commun.* **2018,** *54*, 6573.

[5]   (a) Sato, T.; Tanaka, Y.; Nakayama, K.; Souma, S.; Takahashi, T.; Sasaki, S.; Ren, Z.; Taskin, A. A.; Segawa, K.; Ando, Y., Fermiology of the Strongly Spin-Orbit Coupled Superconductor Sn$_{1-x}$In$_x$Te: Implications for Topological Superconductivity. *Phys. Rev. Lett.* **2013,** *110*, 206804. (b) Yoichi, A.; Liang, F., Topological Crystalline Insulators and Topological Superconductors: From Concepts to Materials. *Rev. Condens. Matter Phys.* **2015,** *6*, 361. (c) Liu, J.; Hsieh, T. H.; Wei, P.; Duan, W.; Moodera, J.; Fu, L., Spin-filtered edge states with an electrically tunable gap in a two-dimensional topological crystalline insulator. *Nat. Mater.* **2014,** *13*, 178. (d) Zeljkovic, I.; Okada, Y.; Serbyn, M.; Sankar, R.; Walkup, D.; Zhou, W.; Liu, J.; Chang, G.; Wang, Y. J.; Hasan, M. Z.; Chou, F.; Lin, H.; Bansil, A.; Fu, L.; Madhavan, V., Dirac mass generation from crystal symmetry breaking on the surfaces of topological crystalline insulators. *Nat. Mater.* **2015,** *14*, 318. (e) Liang, T.; Gibson, Q.; Xiong, J.; Hirschberger, M.; Koduvayur, S. P.; Cava, R. J.; Ong, N. P., Evidence for massive bulk Dirac fermions in Pb$_{1-x}$Sn$_x$Se from Nernst and thermopower experiments. *Nat. Commun.* **2013,** *4*, 2696. (f) Okada, Y.; Serbyn, M.; Lin, H.; Walkup, D.; Zhou, W.; Dhital, C.; Neupane, M.; Xu, S.; Wang, Y. J.; Sankar, R.; Chou, F.; Bansil, A.; Hasan, M. Z.;

Wilson, S. D.; Fu, L.; Madhavan, V., Observation of Dirac Node Formation and Mass Acquisition in a Topological Crystalline Insulator. *Science* **2013,** *341*, 1496.

[6]   (a) Hsieh, T. H.; Lin, H.; Liu, J.; Duan, W.; Bansil, A.; Fu, L., Topological crystalline insulators in the SnTe material class. *Nat. Commun.* **2012,** *3*, 982. (b) Tanaka, Y.; Sato, T.; Nakayama, K.; Souma, S.; Takahashi, T.; Ren, Z.; Novak, M.; Segawa, K.; Ando, Y., Tunability of the k-space location of the Dirac cones in the topological crystalline insulator $Pb_{1-x}Sn_xTe$. *Phys. Rev. B* **2013,** *87*, 155105.

[7]   Kattner, U.; Leo Lukas, H.; Petzow, G.; Gather, B.; Irle, E.; Blachnik, R., Excess enthalpy measurements and thermodynamic evaluation of the Sn-Pb-Te system. *Phys. Rev. Lett.* **1988**, *79*, 32.

[8]   (a) Tan, G.; Shi, F.; Doak, J. W.; Sun, H.; Zhao, L.-D.; Wang, P.; Uher, C.; Wolverton, C.; Dravid, V. P.; Kanatzidis, M. G., Extraordinary role of Hg in enhancing the thermoelectric performance of *p*-type SnTe. *Energy Environ. Sci.* **2015,** *8*, 267. (b) Banik, A.; Shenoy, U. S.; Anand, S.; Waghmare, U. V.; Biswas, K., Mg Alloying in SnTe Facilitates Valence Band Convergence and Optimizes Thermoelectric Properties. *Chem. Mater.* **2015,** *27*, 581. (c) Banik, A.; Biswas, K., Lead-free thermoelectrics: promising thermoelectric performance in *p*-type $SnTe_{1-x}Se_x$ system. *J. Mater. Chem. A* **2014,** *2*, 9620.

[9]   Xu, S. Y.; Liu, C.; Alidoust, N.; Neupane, M.; Qian, D.; Belopolski, I.; Denlinger, J. D.; Wang, Y. J.; Lin, H.; Wray, L. A.; Landolt, G.; Slomski, B.; Dil, J. H.; Marcinkova, A.; Morosan, E.; Gibson, Q.; Sankar, R.; Chou, F. C.; Cava, R. J.; Bansil, A.; Hasan, M. Z., Observation of a topological crystalline insulator phase and topological phase transition in $Pb_{1-x}Sn_xTe$. *Nat. Commun.* **2012,** *3*, 1192.

[10] (a) Wang, Z.; Wang, J.; Zang, Y.; Zhang, Q.; Shi, J. A.; Jiang, T.; Gong, Y.; Song, C. L.; Ji,

S. H.; Wang, L. L.; Gu, L.; He, K.; Duan, W.; Ma, X.; Chen, X.; Xue, Q. K., Molecular Beam Epitaxy-Grown SnSe in the Rock-Salt Structure: An Artificial Topological Crystalline Insulator Material. *Adv. Mater.* **2015,** *27*, 4150. (b) Jin, W.; Vishwanath, S.; Liu, J.; Kong, L.; Lou, R.; Dai, Z.; Sadowski, J. T.; Liu, X.; Lien, H. H.; Chaney, A.; Han, Y.; Cao, M.; Ma, J.; Qian, T.; Wang, S.; Dobrowolska, M.; Furdyna, J.; Muller, D. A.; Pohl, K.; Ding, H.; Dadap, J. I.; Xing, H. G.; Osgood, R. M., Electronic Structure of the Metastable Epitaxial Rock-Salt SnSe {111} Topological Crystalline Insulator. *Phys. Rev. X* **2017,** *7*, 041020. (c) Rehman, S. U.; Butt, F. K.; Tariq, Z.; Hayat, F.; Gilani, R.; Aleem, F., Pressure induced structural and optical properties of cubic phase SnSe: An investigation for the infrared/mid-infrared optoelectronic devices. *J. Alloy Compd.* **2017,** *695*, 194.

[11] Zhao, L. D.; Lo, S. H.; Zhang, Y.; Sun, H.; Tan, G.; Uher, C.; Wolverton, C.; Dravid, V. P.; Kanatzidis, M. G., Ultralow thermal conductivity and high thermoelectric figure of merit in SnSe crystals. *Nature* **2014,** *508*, 373.

[12] (a) Samanta, M.; Biswas, K., Low Thermal Conductivity and High Thermoelectric Performance in $(GeTe)_{1-2x}(GeSe)_x(GeS)_x$: Competition between Solid Solution and Phase Separation. *J. Am. Chem. Soc.* **2017,** *139*, 9382 (b) Rost, C. M.; Sachet, E.; Borman, T.; Moballegh, A.; Dickey, E. C.; Hou, D.; Jones, J. L.; Curtarolo, S.; Maria, J.-P., Entropy-stabilized oxides. *Nat. Commun.* **2015,** *6*, 8485. (c) Liu, R.; Chen, H.; Zhao, K.; Qin, Y.; Jiang, B.; Zhang, T.; Sha, G.; Shi, X.; Uher, C.; Zhang, W.; Chen, L., Entropy as a Gene-Like Performance Indicator Promoting Thermoelectric Materials. *Adv. Mater.* **2017,** *29*, 1702712.

[13] (a) Chen, Y. X.; Ge, Z. H.; Yin, M.; Feng, D.; Huang, X. Q.; Zhao, W.; He, J., Understanding of the Extremely Low Thermal Conductivity in High-Performance

Polycrystalline SnSe through Potassium Doping. *Adv. Funct. Mater.* **2016,** *26*, 6836. (b) Tang, G.; Wei, W.; Zhang, J.; Li, Y.; Wang, X.; Xu, G.; Chang, C.; Wang, Z.; Du, Y.; Zhao, L. D., Realizing High Figure of Merit in Phase-Separated Polycrystalline Sn$_{1-x}$Pb$_x$Se. *J. Am. Chem. Soc.* **2016**, *138*, 13647. (c) Ge, Z. H.; Song, D.; Chong, X.; Zheng, F.; Jin, L.; Qian, X.; Zheng, L.; Dunin-Borkowski, R. E.; Qin, P.; Feng, J.; Zhao, L. D., Boosting the Thermoelectric Performance of (Na,K)-Codoped Polycrystalline SnSe by Synergistic Tailoring of the Band Structure and Atomic-Scale Defect Phonon Scattering. *J. Am. Chem. Soc.* **2017**, *139*, 9714. (d) Wei, T. R.; Tan, G.; Zhang, X.; Wu, C. F.; Li, J. F.; Dravid, V. P.; Snyder, G. J.; Kanatzidis, M. G., Distinct Impact of Alkali-Ion Doping on Electrical Transport Properties of Thermoelectric *p*-type Polycrystalline SnSe. *J. Am. Chem. Soc*. **2016**, *138*, 8875.

[14] (a) Shi, X. L.; Zheng, K.; Liu, W.-D.; Wang, Y.; Yang, Y.-Z.; Chen, Z. G.; Zou, J., Realizing High Thermoelectric Performance in *n*-Type Highly Distorted Sb-Doped SnSe Microplates via Tuning High Electron Concentration and Inducing Intensive Crystal Defects. *Adv. Energy Mater.* **2018**, *8*, 1800775. (b) Zhang, Q.; Chere, E. K.; Sun, J.; Cao, F.; Dahal, K.; Chen, S.; Chen, G.; Ren, Z. C., Studies on Thermoelectric Properties of *n*-type Polycrystalline SnSe$_{1-x}$S$_x$ by Iodine Doping. *Adv. Energy Mater.* **2015**, *5*, 1500360.

List of publications

1. **Chandra, S.**; Banik, A.; Biswas, K., n-Type Ultrathin Few-Layer Nanosheets of Bi-Doped SnSe: Synthesis and Thermoelectric Properties. *ACS Energy Lett.* **2018**, *3*, 1153-1158.

2. **Chandra, S.**; Biswas, K., Realization of High Thermoelectric Figure of Merit in Solution Synthesized p-type 2D SnSe Nanoplates via Ge Alloying. (Manuscript is currently under revision)

Biography

Sushmita Chandra was born on February 16, 1995 in Kolkata, West Bengal (India). She did her B.Sc. Hons. Chemistry (2016) from Lady Brabourne College, University of Calcutta. She joined as an Int. PhD student (Chemical Sciences) at New Chemistry Unit of Jawaharlal Nehru Centre for Advanced Scientific Research (JNCASR), Bangalore, India in August 2016. Currently, she is working with Prof. Kanishka Biswas as MS Student from January 2017. Her research work is focused on tin selenide (SnSe) based layered thermoelectric materials.